

ESD TDR 65-318

ESTI FILE COPY

SD-TDR-65-318

ESD RECORD COPY

RETURN TO
SCIENTIFIC & TECHNICAL INFORMATION DIVISION
(ESTI), BUILDING 1211

ESD ACCESSION LIST

ESTI Call No. AL 48213

Copy No. 1 of 1 cys.

2

Solid State Research

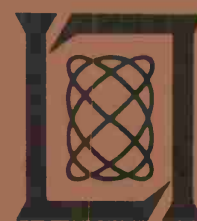
1965

Prepared under Electronic Systems Division Contract AF 19(628)-5167 by

Lincoln Laboratory

MASSACHUSETTS INSTITUTE OF TECHNOLOGY

Lexington, Massachusetts



AD624611

The work reported in this document was performed at Lincoln Laboratory, a center for research operated by Massachusetts Institute of Technology, with the support of the U.S. Air Force under Contract AF 19(628)-5167.

Non-Lincoln Recipients

PLEASE DO NOT RETURN

Permission is given to destroy this document
when it is no longer needed.

2

Solid State Research

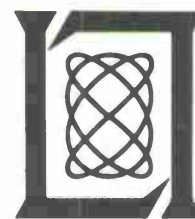
1965

Issued 4 November 1965

Lincoln Laboratory

MASSACHUSETTS INSTITUTE OF TECHNOLOGY

Lexington, Massachusetts



ABSTRACT

This report covers in detail the solid state research work at Lincoln Laboratory for the period 1 May 1965 through 31 July 1965. The topics covered are Solid State Device Research, Laser Research, Materials Research, and Physics of Solids.

Accepted for the Air Force
Stanley J. Wisniewski
Lt Colonel, USAF
Chief, Lincoln Laboratory Office

INTRODUCTION

I. SOLID STATE DEVICE RESEARCH

Photoluminescence spectra of bulk InSb pumped with the output from a GaAs laser have been used to identify the band-to-band radiative transition as well as transitions from the conduction band to zinc acceptor levels and to cadmium acceptor levels. Diode lasers, as well as optically pumped n-type bulk lasers, have involved band-to-band emission. Optically pumped p-type bulk lasers have been fabricated from cadmium-doped samples and have involved transitions to the cadmium acceptor levels. The most efficient material for optically pumped bulk-laser action has been pure n-type ($n = 10^{14} \text{ cm}^{-3}$). Pumping a surface at right angles to the cavity axis produced beam angles which imply active regions of about 40μ in diameter. Thus, although the GaAs radiation is expected to penetrate only about 1μ into the InSb, the diffusion length of the electrons and holes is such that the recombination region spreads over a much greater volume. Greater efficiencies and lower thresholds have been obtained by decreasing the sample thickness. If the surface recombination can be kept low, with thicknesses shorter than a diffusion length, much larger equilibrium densities can be obtained for a given incident pump flux density, and some of the lossy regions are eliminated from the material. For a $50\text{-}\mu$ sample, the threshold for laser action (converting the absorbed power into an equivalent injection current) at 10°K corresponded to about 100 amp cm^{-2} , a factor of 10 less than that obtained with InSb diode lasers without a magnetic field. Because the surfaces of the sample were etched to keep surface recombination low, they are quite rough and the beam angles have exceeded the dewar window aperture; however, the external quantum efficiency of the spontaneous emission, assuming that the sample radiates isotropically (no deviation was measurable over the one-steradian optical access), is about 50 percent. It is apparent that the large diffusion lengths, although they may limit the threshold power density may be used to obtain laser action from large volumes and with a longitudinal type structure — with the pumping beam incident upon one large area face of a semiconductor and the laser emission emerging from the opposite, parallel face.

Present InAs diode lasers which emit near 3.1μ (band-to-acceptor line) have external quantum efficiencies of about 12 percent and threshold current densities of about 300 amp cm^{-2} at 11°K , and they can be operated continuously with currents of several amperes. With magnetic fields of several kilogauss applied perpendicular to the diode current, the threshold has been further reduced and the efficiency increased to as much as 25 percent. This enhancement of emission is shown to be associated with a decrease of injected carrier diffusion in the magnetic field which produces a more compact active region. The threshold increases nearly exponentially with temperature up to 150°K , the highest temperature for InAs laser action at present.

The output wavelength of the coherent and spontaneous emission from PbSe diode lasers operating at 77°K has been tuned from 7.3 to 11.2 μ by applying hydrostatic pressure up to 7 kilobars. The pressure variation of the photon energy of the emitted radiation is -8.50×10^{-6} eV/bar, in substantial agreement with the pressure coefficient of -9×10^{-6} eV/bar of the optical absorption edge. As in the case of magnetic and temperature tuning, pressure tuning of the laser emission involves small changes in the wavelength of the excited cavity modes and switching of these modes, so that the dominant mode varies as above. The individual modes shift at the rate of 2.5×10^{-6} eV/bar at 400 bars and 1.6×10^{-6} eV/bar at 6.5 kilobars. This shift, which is due to the change in optical length of the Fabry-Perot cavity, corresponds to a relative variation $(1/n)(dn/dP)$ of about 1.3×10^{-5} bar $^{-1}$. With diode current held constant, we have observed no significant change in intensity of the coherent or spontaneous emission with pressure. Extension of this work to 13 kilobars, the freezing pressure of helium at 77°K, should be a straightforward task requiring the development of a suitable window transparent to about 21 μ . Higher pressures will require new techniques, but we feel that extension to 20 kilobars, the pressure at which the energy gap of PbSe is expected to close at 77°K, is possible.

Magnetoemission experiments reported previously for PbSe and PbTe diode lasers have been further refined and also have been extended to PbS diode lasers. For these PbS diodes, the shift in the spontaneous emission peak with magnetic field is consistent with a value for the reduced effective mass of $0.05 m_0$, and g values $|g_v| = 7.0$ and $|g_c| = 11.5$, all values being for the [100] direction. From the shift of the individual modes with magnetic field, the magnetodispersion $(\partial n / \partial H)_{[100]}^E$ for PbSe and PbTe are, respectively, -1.3×10^{-6} gauss $^{-1}$ and -1.2×10^{-6} gauss $^{-1}$.

Experimental results of the Gunn effect in n-GaAs support the transferred electron model of Ridley and Watkins as the model for this effect. The bulk negative resistance that results if the transfer occurs rapidly enough as the electric field is increased leads to the formation of domains of different electrical conductivity which move through the sample. The shape of the current vs time waveform for the longer samples ($l \sim 100$ to 1000μ) — sharp spikes in current separated by flat valleys in current — and the observed independence of threshold electric field (2300 to 4000 volts/cm) on sample length are consistent with a negative resistance model. The value of electric field which characterizes the regions of high conductivity, about 1500 volts/cm, is independent of sample length as expected. In addition, the voltage across the high electric field domain scales with sample length, also as expected, and the value of electric field which characterizes the regions of low conductivity is estimated to be $\geq 60,000$ volts/cm. The effects of temperature on the threshold electric field and threshold electron drift velocity are consistent with the transferred electron model. For short samples ($l \sim 25$ to 100μ), a sinusoidal current vs time waveform is seen, and for samples in the $100\text{-}\mu$ length range, the sinusoidal mode is seen near threshold and the spike mode is seen well above threshold. Although the sinusoidal mode is not predicted by the simplest form of the model, the effects of magnetic field and termination impedance on this mode are

consistent with the interpretation of this mode as a longitudinal disturbance caused by a negative resistance. The Gunn effect has also been observed in n-CdTe, and resistance vs hydrostatic pressure experiments show that the transferred electron model is a reasonable explanation for this material as well. Finally, the absence of an instability in n-InSb and n-InAs is shown to be consistent with the detailed band structure of these materials and the transferred electron model.

II. LASER RESEARCH

Laser beam perturbation of the refractive index of absorbing media has been further studied. In the recent work, ammonia gas is used in place of the liquid material previously studied. By utilizing a neodymium laser for the perturbing beam and a pulsed argon laser as the interferometer source, the fringe shift, or change in optical path-length, has been correlated with the energy deposition across the area of the neodymium beam. The measured changes in index of refraction are approximately 1.7 times greater than would be predicted from a simple theory. Q-switched operation of the neodymium source leads to similar results, indicating that the fringe shifts are determined only by the total energy deposited and are not power dependent.

Electron densities in an argon ion laser have been measured by observation of the Stark broadening of particular neutral argon lines. Densities of 10^{13} to 10^{14} cm^{-3} have been measured over the range of currents used. These densities have in turn been correlated with the stimulated and spontaneous emission and the voltage across the tube.

The high pressure mercury laser system has been further tested without successful oscillation. The negative results are attributed to insufficient gain as calculated from the measured spontaneous emission.

The photocurrent spectrum and photoelectric counts produced by a gaseous laser have been measured. In using a semiclassical theory of the van der Pol oscillator, we find good agreement between the experimental and theoretical values of the three lowest order factorial moments of the photocount distribution.

Multiple stimulated Brillouin scattering has been measured in quartz by using a ruby laser. As many as six successive Brillouin shifts have been observed as a result of iterative scattering and reamplification in the ruby rod. Only Stokes waves are generated in the experiment, which can be explained by considerations of the Brillouin conversion efficiency and ruby gain.

III. MATERIALS RESEARCH

Single crystals of zinc aluminate doped with approximately 0.1 percent Co^{+2} have been grown from a flux of lead oxyfluoride. The crystals, which are blue and transparent,

will be used for measurements of the nuclear hyperfine field of tetrahedrally coordinated Co^{+2} .

Conductivity measurements have been made between 120° and 670°K on single crystals of LaVO_3 and YVO_3 obtained by slow cooling of the melts in iridium crucibles, and magnetic susceptibility measurements are being made on powders prepared from the crystals. The data indicate that the t_{2g} state of V^{+3} in these rare-earth perovskites exists as discrete levels, without the formation of bands. Preliminary results indicate the existence of an antiferromagnetic transition in LaVO_3 at $T_N \approx 135^\circ\text{K}$.

According to a tentative stability diagram which has been obtained for perovskite phases in the La-Mn-O system, these phases exist over wide ranges of composition. The diagram shows that the amount of Mn^{+4} in a particular sample depends sensitively on the conditions of preparation as well as on the ratio of lanthanum to manganese.

The results of high temperature x-ray diffraction measurements on powdered LaCoO_3 show that the semiconductor \rightleftharpoons metal transition which occurs at 1210°K is accompanied by a change in space group from $R\bar{3}$ below this temperature to $R\bar{3}m$ above it. Between 600° and 1210°K, the degree of order increases with increasing temperature.

The accuracy with which crystallographic parameters can be calculated from x-ray diffraction data has been markedly improved by applying the simplex method for minimizing the differences between experimental and computed values of observable quantities. Computer programs that use this method have been written for calculating cell edge values from 2θ data and for calculating atom positions from line intensity data.

Crystallographic parameters for 10 spinels of the type ACr_2X_4 (where A = Mn, Fe, Co, Cu, Zn, or Cd; and X = O, S, or Se) have been calculated by the simplex method from x-ray diffraction data on powdered samples. Comparison with neutron diffraction results indicates that standard x-ray powder measurements can yield crystallographic parameters comparable in accuracy to those obtained by neutron diffraction experiments.

In order to obtain calibration data for determining selenium partial pressures over HgSe(c) and other binary selenides, the optical density of selenium vapor in equilibrium with pure liquid selenium has been measured between 1900 Å and 2.0μ for total selenium pressures between 7×10^{-5} and 1.0 atm. The partial pressures of Se_2 obtained from the data agree closely with those calculated from the dissociation constants for Se_4 , Se_6 , and Se_8 reported by Illarionov and Lapina.

The resistivity and Hall coefficient of oriented Ti_2O_3 single crystals have been measured between 4.2° and 390°K at magnetic fields between 8 and 170 kG. Neither property changes appreciably with sample orientation. This lack of anisotropy is inconsistent with a proposed band model which ascribes band formation near the Fermi level exclusively to direct cation-cation interactions.

The similarity between high pressure InSb(II) and $\beta\text{-Sn}$ is being explored by studying the InSb(II) -In system in order to compare its properties with those of the Sn-In system. Initial measurements on $\text{InSb(II)}_{1-x}(2\text{In})_x$ samples with x between 0.1 and 0.5 suggest the existence of a phase analogous to the tin-rich γ -phase in the Sn-In system.

Experiments on $\text{CaF}_2:\text{Dy}^{+2}$ lasers that contain different concentrations of Y have shown that Y^{+2} quenches the fluorescence of Dy^{+2} and therefore raises the threshold for laser action. The results of fluorescent lifetime measurements show that quenching is due to resonant energy transfer between the $^5\text{I}_7$ level of Dy^{+2} and excited t_{2g} levels of Y^{+2} .

IV. PHYSICS OF SOLIDS

Reflectivity measurements in single crystals of ReO_3 in the vicinity of 2.3 eV indicate a steep plasma edge which is reminiscent of silver and which may therefore arise from a similar mechanism, namely, competing intraband and interband processes.

Oscillatory magnetoabsorption and Faraday rotation studies at 1.5°K and up to magnetic fields of 103 kG are being carried out in single crystals of a number of semiconductors. The indirect edge is being examined in germanium, and oscillatory effects due to direct transitions are being studied in GaSb and GaSe.

In the continuing optical study of sulfur-doped silicon, a fourth impurity center has been found, in addition to those previously reported. This center, which is presumed to be due to pairs of neutral sulfur atoms, exhibits a spectrum under stress with unexpected extra splittings.

A more direct determination of the spin-orbit band splitting ϵ_{so} has been made in graphite by use of the magnetoreflexion data. The result $\epsilon_{\text{so}} = 0.005 \pm 0.002$ eV is greater by at least one order of magnitude from previous estimated values but comparable to that measured in diamond by Rauch, $\epsilon_{\text{so}} = 0.006$ eV.

A study of the behavior of the excitation spectra of group III impurities in germanium under uniaxial stress has been completed. The various experimental lines have been identified from line intensities and polarization effects. Deformation potentials for the valence band have been determined.

Measurements of the microwave surface impedance in p-type PbSe, in the Azbel-Kaner geometry, as a function of magnetic field at 70 kMcps have indicated complicated hybrid resonances as well as magnetoplasma effects. In order to simplify the data and hence the theoretical interpretation, a new cavity is being constructed which should provide a better control between the relative orientations of the RF electric field and the DC magnetic field.

Helicon wave propagation is being studied in single crystals of PbTe at 9 kMcps and 4.2°K, and with magnetic fields up to 10 kG. The measured anisotropies of the complex propagation vector should provide information on the effective mass and collision time anisotropies.

The microwave phonon generation work at 70 kMcps is continuing. By using a combination of a better sample, as well as an improved cavity, the number of echoes which can be observed has been doubled so that now eight to ten echoes are observed; thus the T^4 temperature dependence of the attenuation in x-cut quartz has been confirmed with an improved accuracy.

The propagation of microwave phonons (9 kMcps) is also being studied in pure semiconductors at low temperatures where electron-phonon scattering is the predominant hypersonic attenuation mechanism. Extremely sensitive measurements can be made of the magnetic field dependence of both the attenuation and velocity. The performance of the microwave detection system has been verified by using GaAs single-crystal samples and also x-cut quartz.

The spin wave dispersion experiments on permalloy (63 percent nickel-37 percent iron) films have been extended to low temperatures. These studies, which have now been carried out at 4.2°, 77°, and 298°K on the same sample, indicate that the long-range interaction distance is approximately one order of magnitude larger than the nearest-neighbor distance and that the coefficient of the quartic term is roughly (within 20 percent) temperature independent.

Magnetic studies are being extended to chromium spinels with nonmagnetic A-sites. One interesting material being measured is the cubic spinel CdCr_2Se_4 which has been found to be ferromagnetic and also nonconducting. Thus, this compound offers a rather unique theoretical opportunity for comparison with the Heisenberg model of ferromagnetism.

Studies are being made of the variation of thermoelectric power with hydrostatic pressure in extrinsic n-type HgSe, HgTe, and $\text{HgSe}_x\text{Te}_{1-x}$ alloys. These measurements are being used to supply evidence for the relative ordering of the Γ_6 and Γ_8 energy states.

The numerical calculation, for $T = 0^\circ\text{K}$, of the magnetic field dependence of the energy and linewidth of the transition between the $n = 0$ and $n = 1$ Landau levels of a piezoelectric polaron has been completed; the effect is found to be very small. However, a similar evaluation for the optical polaron indicates a considerably larger nonlinear magnetic field dependence which may be experimentally observable.

The nonrelativistic augmented plane wave (APW) technique has been used to calculate the electronic band structure of the rare-earth metals gadolinium, thulium, and lanthanum, and also palladium metal. The rare-earth calculations account for the bandwidth of the 4f band in gadolinium as measured in photoemission experiments and also the exchange splittings of the s-d conduction bands. Further predictions have been made concerning the expected optical properties in the visible and ultraviolet. In palladium, a Fermi surface consisting of two hole surfaces and a compensating electron surface has been calculated; good agreement is found with the results of de Haas-van Alphen data.

It has generally been assumed that the Hartree-Fock ground state of closed shell atoms and atomic ions always has the ^1S symmetry of the exact ground state, although the assumption has recently been questioned. It is shown here that this assumption is not generally correct. This implies that Hartree-Fock theory for such systems should now be reinvestigated and raises fundamental questions about the meaningfulness of "correlation" corrections as usually defined, and hence about criteria for the importance of such corrections.

TABLE OF CONTENTS

Abstract	iii
Introduction	v
Organization	xiii
Reports by Authors Engaged in Solid State Research	xiv
 I. SOLID STATE DEVICE RESEARCH	 1
A. InSb Photoluminescence with Improved Quantum Efficiencies	1
B. Properties of InAs Lasers	5
C. Pressure Tuned PbSe Diode Laser	7
D. Magnetoemission Studies of PbS, PbTe, and PbSe Diode Lasers	8
1. Introduction	8
2. Landau Levels in the Lead Salts	8
3. Experiment	9
4. Spontaneous Emission	11
5. Laser Emission	13
E. Gunn Effect in Compound Semiconductors	14
 II. LASER RESEARCH	 17
A. Perturbation of Refractive Index of Absorbing Media by a Laser Beam	17
B. Stark Linewidth Measurement of Ion Density in an Argon Ion Laser	20
C. High Pressure Mercury Laser	21
D. Photocurrent Spectrum and Photoelectric Counts Produced by a Gaseous Laser	22
E. Multiple Stimulated Brillouin Scattering in Solids	23
 III. MATERIALS RESEARCH	 27
A. Single-Crystal Growth of Cobalt-Doped ZnAl_2O_4	27
B. Single-Crystal Growth and Properties of LaVO_3 and YVO_3	27
C. Perovskite Phase Stability in La-Mn-O System	29
D. Semiconductor \rightleftharpoons Metal Transition in LaCoO_3	30
1. Symmetry	30
2. Structural Mechanism	31
3. Interpretation	31
E. Application of Simplex Method to Crystallographic Calculations	33
F. Crystallographic Study of Chromium Spinels	35
G. Partial Pressures from Optical Density Measurements of Vapor Phase	36
H. Resistivity and Hall Coefficient of Ti_2O_3	37
I. Superconductivity and Resistivity in High Pressure InSb-In System	40
J. Quenching of Dy^{+2} Fluorescence by Y^{+2} in $\text{CaF}_2:\text{Dy}^{+2}$ Lasers	41

IV. PHYSICS OF SOLIDS	45
A. Magneto-Optics	45
1. Reflectivity of ReO_3	45
2. Oscillatory Faraday Rotation and Magnetoabsorption of the Indirect Transition in Germanium	46
3. Oscillatory Faraday Rotation of the Direct Transition in GaSb	49
4. Magnetoabsorption of Circularly Polarized Light in GaSb	51
5. Magnetoabsorption of the Direct Transition in GaSe	53
6. Optical Studies of Sulfur-Doped Silicon	55
7. Determination of Spin-Orbit Band Splitting in Graphite	55
8. Excitation Spectra of Group III Impurities in Germanium Under Uniaxial Stress	57
B. Solid State Magnetoplasmas	57
1. Magnetoplasma Cyclotron Resonance in p-Type PbSe	57
2. Magnetoplasma Wave Propagation in PbTe	58
C. Hypersonic Waves in Solids	59
1. Microwave Phonon Generation at 70 kMcps	59
2. Attenuation of 9-kMcps Hypersonic Waves in Semiconductors	59
D. Magnetism	60
1. Long-Range Exchange Interaction from Spin Wave Resonance	60
2. Magnetic Properties of Chromium Spinel with Nonmagnetic A-Sites	60
E. Band Structure of Mercury Chalcogenides	63
1. Thermoelectric Power vs Pressure for HgSe, HgTe, and $\text{HgSe}_x\text{Te}_{1-x}$ Alloys	63
F. Theory	64
1. Cyclotron Resonance of Piezoelectric Polarons	64
2. Optical Properties of Rare-Earth Metals	64
3. Electronic Band Structure, Fermi Surface, and Magnetic Properties of Palladium Metal	65
4. On the Symmetry of Hartree-Fock Ground States	66

ORGANIZATION

SOLID STATE DIVISION

H. C. Gatos, *Head*
 A. L. McWhorter, *Associate Head*
 P. E. Tannenwald, *Assistant Head*
 M. J. Hudson, *Assistant*
 E. P. Warekois
 D. T. Stevenson*
 T. C. Harman†

SOLID STATE THEORY

H. J. Zeiger, *Leader*
 M. M. Litvak, *Assistant Leader*

Argyres, P. N.	Larsen, D. M.
Dimmock, J. O.	Mason, V. J.
Dresselhaus, G. F.	Mason, W. C.
Houghton, B. H.*	Rawson, N. B.*
Kaplan, T. A.	Sorbello, R. S.‡
Kelley, P. L.	Stanley, H. E.*
Kirkpatrick, E. S.‡	Trent, P. H.
Kleiner, W. H.	Van Zandt, L. L.

OPTICS AND INFRARED

R. H. Kingston, *Leader*
 R. J. Keyes, *Assistant Leader*

Bates, D. H.	Longaker, P. R.
Bostick, H. A.	McGowan, J.
Carbone, R. J.	Reese, R. L.‡
Dennis, J. H.	Zimmerman, M. D.
Freed, C.	

ELECTRONIC MATERIALS

J. B. Goodenough, *Leader*
 J. M. Honig, *Associate Leader*
 A. J. Strauss, *Assistant Leader*

Andrews, H. I.§	Hilsenrath, S.
Amott, R. J.	Kafalas, J. A.
Bachner, F. J.§	LaFleur, W. J.
Banus, M. D.	Lavine, M. C.*
Brebrick, R. F.	Newman, W. A.
Button, M. J.	O'Connor, J. R.
Cornwell, J. C.	Owens, E. B.
Delaney, E. J.	Paladino, A. E.
Ehlers, H. H.	Plonko, M. C.
Esterling, D. M.‡	Pollard, E. R.§
Fahey, R. E.	Raccach, P. M.
Farrell, L. B.	Reed, T. B.
Ferretti, A.	Ridgley, D. H.
Finn, M. C.	Roddy, J. T.
Fischler, S.	Rogers, D. B.
Geisman, J. H.‡	Siuta, V. P.§
Germann, R. W.	Whipple, E. R.

SOLID STATE PHYSICS

J. G. Mavroides, *Leader*
 G. B. Wright, *Assistant Leader*

Bernon, S.	Johnson, E. J.
Bostwick, D. I.‡	Kernan, W. C.
Burke, J. W.	Kolesar, D. F.
Buss, D. D.‡	Krag, W. E.
Carman, R. L.*	Mastromattei, E. L.
Curran, E. A.	Menyuk, N.
Dickey, D. H.	Parker, C. D.
DiStefano, T. H.‡	Perry, F. H.
Dresselhaus, M. S.	Schlossberg, H. R.§
Dwight, K., Jr.	Scouler, W. J.
Edwards, D. F.	Stickler, J. J.
Feinleib, J.	Strahm, N. D.§
Feldman, B.	Thaxter, J. B.
Fulton, M. J.	Walters, E.
Groves, S. H.	Weber, R.
Halpern, J.	Weinberg, D. L.

APPLIED PHYSICS

R. H. Rediker, *Leader*

Berninger, W. H.‡	Knepper, R. W.‡
Butler, J. F.	McPhie, J. M.
Calawa, A. R.	Melngailis, I.
Carter, F. B.	Nill, K. W.§
Caswell, F. H.	Palermo, J. S.
Clough, T. F.	Phelan, R. J., Jr.
Donaldson, P. L.	Quist, T. M.
Foyt, A. G., Jr.	Sullivan, F. M.
Grant, C. R.	Walpole, J. M.§
Hinkley, E. D.	Ward, J. H. R., III
Hurwitz, C. E.	Youtz, P.

* Part Time

† Leave of Absence

‡ Summer Staff

§ Research Assistant

REPORTS BY AUTHORS ENGAGED IN SOLID STATE RESEARCH

15 May 1965 through 15 August 1965

PUBLISHED REPORTS

Journal Articles*

JA No.			
2399	Galvano-Thermomagnetic Phenomena and the Figure of Merit in Bismuth. I. Transport Properties of Intrinsic Material	T.C. Harman J.M. Honig B.M. Tarmy	Adv. Energy Conversion <u>5</u> , 1 (1965), DDC 618461
2454	Resistivities and Transformation Rates of High-Pressure InSb- β Sn Alloys	M.D. Banus L.B. Farrell A.J. Strauss	J. Appl. Phys. <u>36</u> , 2186 (1965)
2480	Partial Pressures of Hg(g) and Te ₂ (g) in the Hg-Te System from Optical Densities	R.F. Brebrick A.J. Strauss	J. Phys. Chem. Solids <u>26</u> , 989 (1965)
2535	Higher Order Corrections to the Molecular-Field Theory of the Magnetic State	G.F. Dresselhaus	Phys. Rev. <u>139</u> , A855 (1965)
MS-1116	Transition-Metal Oxides with Metallic Conductivity	J.B. Goodenough	Bull. Soc. Chim. France, No. 4, 1200 (1965), DDC 618458

* * * * *

UNPUBLISHED REPORTS

Journal Articles

JA No.			
2525	Interband Magneto-Optical Effects	B. Lax J.G. Mavroides	Accepted for Vol. 2, <u>Physics of III-V Compounds</u> , R.K. Willardson and A.C. Beer, Editors (Academic Press, New York)
2550	Spin Orbit Interaction in Graphite	G.F. Dresselhaus M.S. Dresselhaus	Accepted by Phys. Rev.
2556	Long-Range Exchange Interactions from Spin Wave Resonance	R. Weber P.E. Tannenwald	Accepted by Phys. Rev.

* Reprints available.

Unpublished Journal Articles (Continued)

JA No.

2588	Quenching of Dy^{+2} Fluorescence by Y^{+2} in $CaF_2:Dy^{+2}$ Lasers	J. R. O'Connor	Accepted by Appl. Phys. Letters
2589	Effect of Y^{+3} on the Reduction of Sm^{+3} in CaF_2	J. R. O'Connor	Accepted by Appl. Phys. Letters
2590	Simple Apparatus for Applying Uniaxial Pressure at Cryogenic Temperatures	J. H. R. Ward	Accepted by Rev. Sci. Instr.
2597	The Bohr-Sommerfeld Quantization Rule and the Weyl Correspondence	P. N. Argyres	Accepted by Physics
2599	High-Field Magnetoabsorption of the Indirect Transition Exciton in Germanium at 1.7°K	J. Halpern B. Lax	Accepted by J. Phys. Chem. Solids
2600	Partial Pressure of Se_2 and Optical Density of Selenium Vapor in the Visible Ultra-Violet	R. F. Brebrick	Accepted by J. Chem. Phys.
2604	PbS Diode Laser	J. F. Butler A. R. Calawa	Accepted by J. Electrochem. Soc.
2605	Electrical Properties of Metal Oxides Characterized by "Hopping" Charge Carriers	J. M. Honig	Accepted by J. Chem. Educ.
2629	Physics of Quantum Electronics – A Conference Report	P. E. Tannenwald P. L. Kelley B. Lax	Accepted by Phys. Today
	<u>Galvano-Thermomagnetic Phenomena with Applications to Energy Conversion</u>	T. C. Harman J. M. Honig	Accepted by McGraw-Hill, New York

Meeting Speeches*

MS No.

1134A-B	Chemical Uses of Induction Plasmas	T. B. Reed	United Aircraft Research Laboratories, East Hartford, Connecticut, 27 May 1965; Stanford Research Center, Stanford, California, 13 May 1965.
1243F-H	Recent Advances in Semiconductor Lasers	R. H. Rediker	Seminar, University of Southern California, Los Angeles, 15 July 1965; Seminar, Aerospace Corporation, El Segundo, California, 16 July 1965; Seminar, Eastman-Kodak, Rochester, New York, 30 July 1965.

* Titles of Meeting Speeches are listed for information only. No copies are available for distribution.

Unpublished Meeting Speeches (Continued)

MS No.

1245A-B	Recent Developments in Crystal Growth	T. B. Reed	Arizona State University, 6 May 1965; University of Arizona, 7 May 1965
1253	Intricately-Shaped Semimetal Samples by Spark Erosion	S. Fischler M. J. Button	Electrochemical Society Semiconductor Sessions, San Francisco, 13 May 1965
1293	Spin Orbit Interaction in Graphite	G. F. Dresselhaus M. S. Dresselhaus J. G. Mavroides	Seventh Biennial Conference on Carbon, Cleveland, Ohio, 21-25 June 1965
1294	Energy Band Parameter Determination in Graphite	M. S. Dresselhaus J. G. Mavroides	
1339	Amplitude Noise in Gas Lasers Below and Above the Threshold of Oscillation	C. Freed H. A. Haus*	Physics of Quantum Electronics Conference, San Juan, Puerto Rico, 28-30 June 1965
1343	Sum and Difference Frequency Generation in Gases and Liquids	P. N. Butcher* W. H. Kleiner P. L. Kelley H. J. Zeiger	
1396	Magneto-Emission Studies of PbS, PbTe, and PbSe Diode Lasers	J. F. Butler A. R. Calawa	
1397	Laser Emission by Optical Pumping of Semiconductors	R. J. Phelan, Jr.	
1398	Multiple Stimulated Brillouin Scattering in Solids	P. E. Tannenwald	
1399	Plasmon Scattering of Light and Stimulated Emission of Plasmons in Solids	A. L. McWhorter	
1341	Focusing Far Infrared Reflection Filters	D. H. Dickey	20th Annual Molecular Spectroscopy Symposium, Columbus, Ohio, 14-18 June 1965
1346	Oscillatory Faraday Rotation of the Direct Transition in GaSb at 1.5°K	J. Halpern	American Physical Society, New York, 23-25 June 1965
1357A	Thermodynamics of Semiconducting Tellurides	R. F. Brebrick	IRIS Specialty Group, Syracuse University, 15 June 1965

* Author not at Lincoln Laboratory.

Unpublished Meeting Speeches (Continued)

MS No.

1382	Pressure Tuned Lead Salt Laser	J. M. Besson* J. F. Butler A. R. Calawa W. Paul* R. H. Rediker	1965 Solid-State Device Research Conference, Princeton University, 21-23 June 1965
1383	Electrical and Electro-Optical Properties of GaAs-InSb "Schottky" Barrier Heterojunctions	E. D. Hinkley R. H. Rediker	
1384	Transients and Hot Carrier Effects in InSb Bulk Injection Lasers	I. Melngailis	
1385	Properties of Optically Pumped Semiconductor Lasers	R. J. Phelan, Jr.	
1388	High Electric Field and Pressure Effects in n-CdTe, n-InAs and n-InSb	A. G. Foyt W. Paul* A. L. McWhorter	1965 Solid-State Device Research Conference, Princeton University, 21-23 June 1965; 1965 Conference on Electron Device Research, University of Illinois, 23-25 June 1965
1387, 1387A	Helicon Instabilities in Drifted Plasmas	A. Bers* A. L. McWhorter	
1389	Effect of Pressure on Electrical Properties of Some $Al_{III}B_{VI}$ Compounds	M. D. Banus	Symposium, New York University, 13 May 1965
1394	Magneto-Optical Effects in Solids	G. F. Dresselhaus	Lecture Series, Optical Properties of Solids, Enrico Fermi School, Varena, Italy, 28 June - 9 July 1965
1422	Theory of the Method of Kinetic Equations for Quantum Systems	P. N. Argyres	Lecture Series, Summer Institute for Theoretical Physics, University of Colorado, 14-25 June 1965
1425	Directed Heating with Atoms, Electrons, and Photons	T. B. Reed	American Cyanamid Company, Stamford, Connecticut, 17 June 1965
1428	Magnetospectroscopy in Solids	J. G. Mavroides	Lecture Series, University of California, Los Angeles, 19-30 July 1965
1429	Magnetospectroscopy in Solids	J. O. Dimmock	
1449	Gunn Effect in Compound Semiconductors	A. L. McWhorter	Gordon Research Conference on Chemistry and Metallurgy of Semiconductors, Andover, New Hampshire, 16 July 1965
1450	Recent Advances in Semi- conductor Lasers	A. L. McWhorter	

* Author not at Lincoln Laboratory.

I. SOLID STATE DEVICE RESEARCH

A. InSb PHOTOLUMINESCENCE WITH IMPROVED QUANTUM EFFICIENCIES

Although we have operated InSb diode lasers without a magnetic field, the quantum efficiencies have been low (about 0.5 percent). InSb diode lasers reported thus far have involved band-to-band emission, whereas the efficient diode lasers of GaAs and InAs have involved an acceptor level. In an attempt to find an efficient transition in InSb, studies of the spontaneous emission were performed. As a result, improved quantum efficiencies were obtained by using optical pumping of homogeneous materials.

Studies of the photoluminescence spectra of InSb at about 10°K have yielded results as shown in Fig. I-1. The InSb samples for these spectra were about 250 μ thick, and the luminescence corresponds to that emitted from the same surface which was pumped by a GaAs diode laser. The figure shows spectra for three n-type and two p-type samples. The solid-line spectra, which correspond to the n-type samples, are due to band-to-band emission. The two samples with $n = 10^{14} \text{ cm}^{-3}$ and $n = 10^{16} \text{ cm}^{-3}$ have produced laser emission both with p-n junctions and by optical pumping. The two lines corresponding to the zinc- and cadmium-doped samples, shown here for the bulk material, were not observed in our diffused diode emission spectra. With optical pumping, the zinc line even appears in our undoped n-type sample ($n = 10^{14}$) but becomes masked by the tail of the band-to-band emission line which grows at a much greater rate as the pump power is increased. Because we are able to observe these lines with optical pumping, we may conclude that the zinc-diffused diodes involved injection into the n-type material. Optical pumping has allowed us to obtain laser emission involving the cadmium level of Fig. I-1; however, the power levels have thus far been in the few milliwatt range.

In looking for the most efficient material, we placed these various samples on a rotating heat sink so that each sample could be pumped in turn. Plots of the photoluminescence intensity vs pump power intensity were obtained and are shown in Fig. I-2. From the linewidth results of Fig. I-1 and the relative external efficiencies shown here, it would appear that the n-type material with $n = 10^{14} \text{ cm}^{-3}$ should yield the lowest thresholds for laser emission. We also note that there is some super-linear behavior in the output of the sample made from this pure InSb. With large competing processes for recombination, the luminescence output should be proportional to the product of the electrons and holes. With the low extrinsic concentration, our available pump power density may be sufficiently large so that this effect can be observed.

Besides the particular transitions involved, there is another factor that limits the threshold power density and, possibly, the laser efficiency. Pumping a surface at right angles to the cavity axis of an InSb sample has produced beam angles which imply active regions of about 40 μ in diameter. Thus, although the GaAs radiation is expected to penetrate only about 1 μ into the InSb, the diffusion length of the electrons and holes is such that the recombination region spreads over a much greater volume. The effect of long diffusion lengths can be observed in the spontaneous emission spectra. The experimental arrangement for observing this effect is shown in Fig. I-3. Again we have the GaAs diode laser emission impinging on an InSb sample mounted on

Section I

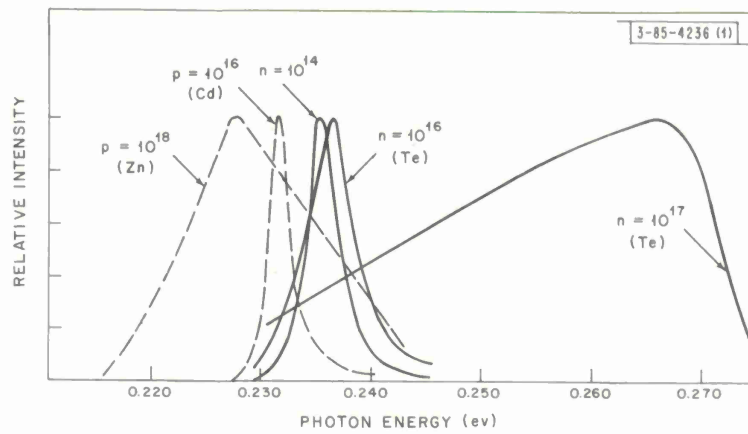


Fig. 1-1. Photoluminescence spectra of three n-type and two p-type InSb samples.

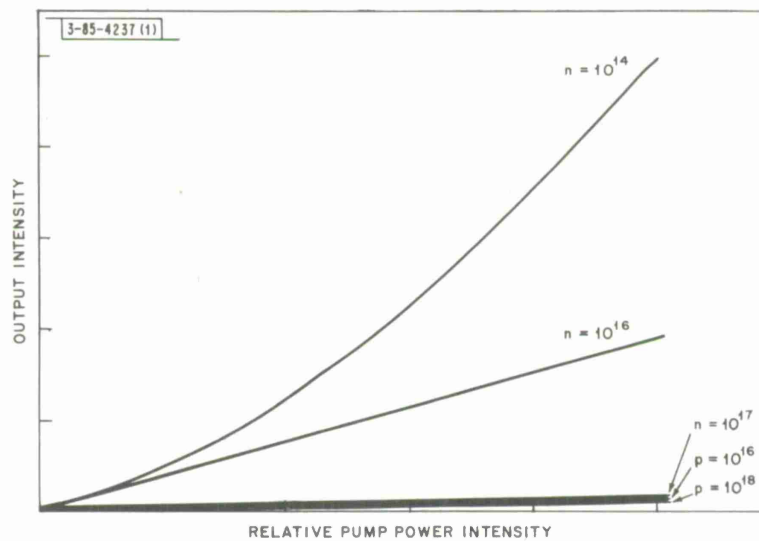


Fig. 1-2. Relative output intensity vs pump power intensity for samples of Fig. 1-1.

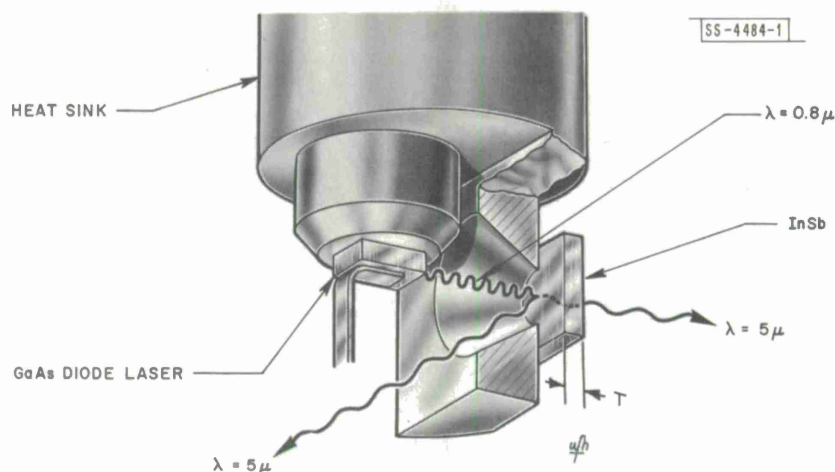


Fig. I-3. Optical pumping arrangement for observing spectral shifts as a function of sample thickness T . Also, an arrangement for obtaining improved quantum efficiencies and lower laser thresholds.

a heat sink. The InSb sample was mounted on the far side of the heat sink so that, when the thickness of the sample was reduced, there would be less of a chance that a shift in the emission spectra to higher energies would be due to a lower temperature for thinner samples. The heat sink also masks out a definite area to be pumped. Spectra were taken of radiation from the front side (the side upon which the GaAs radiation is incident) and from the far side. The results obtained from observing the front side are shown in Fig. I-4. The spectra shown here are normalized to the same height in order to show the shift in the emission peak clearly. As the thickness of the sample was reduced, the emission peak shifted to higher energies. For the spectrum corresponding to the smallest thickness (shown by the dashed line), the sample probably was at a slightly higher temperature because of room temperature radiation through the observation window. For the thin sample, the thermal conductivity and heat capacity were low enough to observe thermal time decays with the available pump powers. Better heat sinking for this thickness has shifted the peak out to about 0.237 eV. It is evident that as the diffusion of the electron-hole pairs is limited to regions close to the surface, there is less loss on the high energy side of the spectrum by reabsorption. Because of the numerous assumptions required, attempts have not been made to obtain exact values of the absorption coefficient or diffusion lengths from the data thus far obtained. On the other hand, we have mentioned that the beam angle implies diffusion lengths of at least $40\ \mu$, and measured absorption coefficients from 1 to $1000\ \text{cm}^{-1}$ in the emission range are consistent with these data.

Noting that the long diffusion lengths may be increasing the active volume, one may attempt to obtain greater efficiencies and lower thresholds by decreasing the sample thickness. If the surface recombination can be kept low, with thicknesses shorter than a diffusion length, much larger equilibrium densities can be obtained for a given incident pump flux density. In addition, we are eliminating some of the lossy regions from the material. Stimulated emission was obtained from the $50\text{-}\mu$ -thick sample; the emission spectra are shown in Fig. I-5. For these spectra, we were pumping one side of the sample and looking at the radiation emitted from the other side. As noted, with an increase in pump power, a very narrow, resolution-limited line emerges

Section I

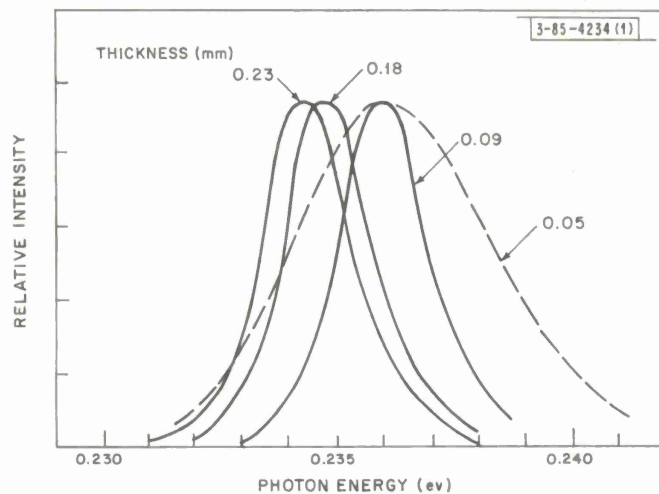


Fig. 1-4. Photoluminescence spectra for various sample thicknesses ($n = 10^{14} \text{ cm}^{-3}$). Spectra correspond to the InSb radiation emitted to the left in Fig. 1-3.

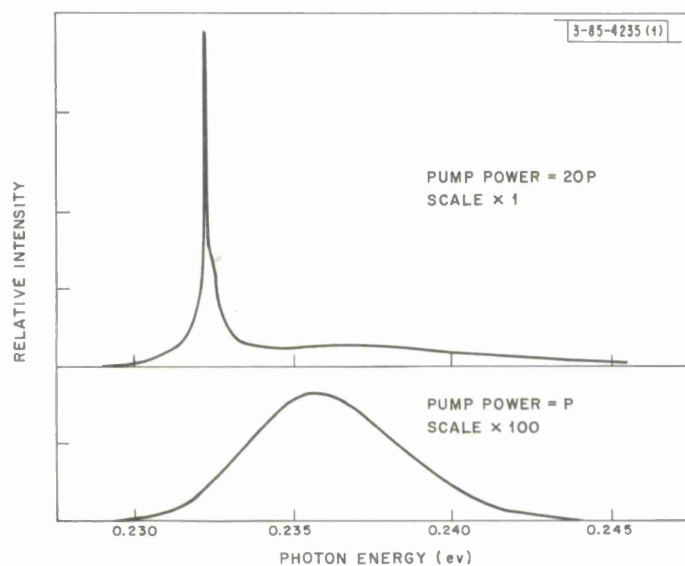


Fig. 1-5. Spectra from a 50-μ-thick n-type sample ($n = 10^{14} \text{ cm}^{-3}$) below and above threshold. Spectra correspond to the InSb radiation emitted to the right in Fig. 1-3.

and is attributed to stimulated emission. If we convert the absorbed power into an equivalent injection current, the threshold corresponds to about 100 amp cm^{-2} , which is about a factor of 10 less than that obtained with InSb diode lasers without a magnetic field.

Because the surfaces of the sample were etched to keep the surface recombination low, they are quite rough and the beam angles have exceeded the dewar window aperture; however, an estimate of the quantum efficiency of the spontaneous emission is quite high. With six watts of GaAs radiation incident on the InSb samples, accounting for reflection (which for InSb is about 50 percent for this wavelength region), we have an equivalent injection of 2 amp. Because the surface is rough we may expect the spontaneous emission of the sample to radiate almost spherically (no deviation was measurable over 34 degrees – the optical access), and one may extrapolate the external InSb radiation to an equivalent output of 1 amp. Although some deviation from a spherical radiator should be expected, we have neglected any correction for internal reflection due to the existence of a critical angle for total internal reflection. The total internal reflection argument, with optically flat, plane-parallel faces, can be used to gain as much as a factor of 100 in the internal efficiency. Obviously, here we have multiple reflections between the two relatively rough crystal faces which allow for a high percentage of the radiation to be emitted. In addition, with the thin, highly efficient sample, the output intensity is now a linear function of the input instead of a super-linear behavior as noted in Fig. I-2. The magnetic field also has little effect on the emission intensity, as it did with the thick samples. This supports our belief that we are approaching 100-percent quantum efficiency. If we can improve the surface flatness and retain a low surface recombination velocity, we may be able to limit the emitted beam angle.

In conclusion, we have attempted to improve the efficiency of InSb lasers by optical pumping. Lines not observed with diodes are readily seen with optical pumping, and a continuous transition from the spontaneous to laser emission involving an acceptor level has been obtained. It is also apparent that the large diffusion lengths, although they may limit the threshold power density, may be used to obtain laser action from large volumes and with a longitudinal type structure.

R. J. Phelan, Jr.

B. PROPERTIES OF InAs LASERS

Two different recombination mechanisms can be distinguished in the infrared radiation spectra of InAs. The photoluminescence of n-type InAs corresponds to a direct band-to-band (or weak exciton) transition. The photoluminescence of zinc-doped p-type InAs and the injection luminescence of most zinc-diffused diodes correspond to transitions between conduction band states (not excluding shallow donors for p-type crystals with a heavy donor compensation) and acceptor states about 17 meV above the valence band. The diode emission, therefore, results from injection of electrons into the p-type side of the junction, although band-to-band radiation has also been obtained in some diodes under certain conditions of current density and magnetic field.

Present InAs diode lasers which emit near 3.1μ (band-to-acceptor line) have external quantum efficiencies of about 12 percent and threshold current densities of about 300 amp cm^{-2} at 11°K, and they can be operated continuously with currents of several amperes. With magnetic fields of several kilogauss applied perpendicular to the diode current, the threshold has been

Section I

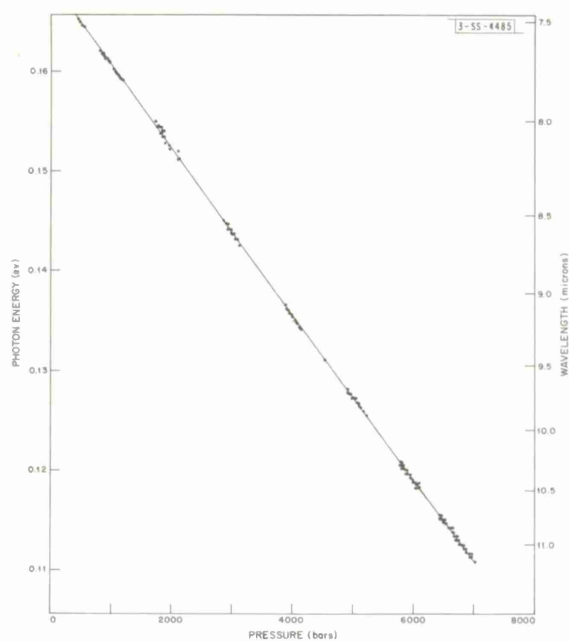


Fig. I-6. Variation with pressure of the dominant emission modes from a PbSe diode laser at 77°K. Current density = 4800 amp cm⁻².

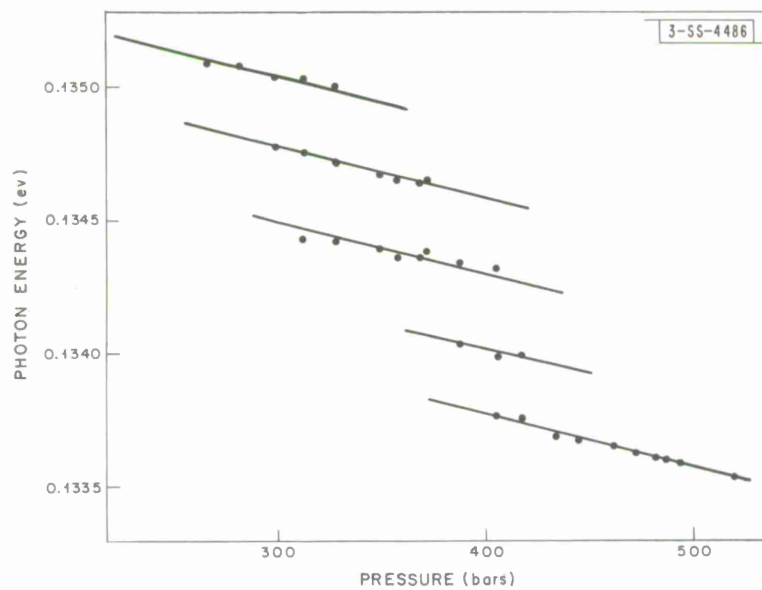


Fig. I-7. Variation of emission modes over a small pressure range at 77°K. Current density = 9000 amp cm⁻².

further reduced and the efficiency increased to as much as 25 percent. This enhancement of emission is shown to be associated with a decrease of injected carrier diffusion in the magnetic field which produces a more compact active region. The threshold increases nearly exponentially with temperature up to 150°K, the highest temperature for laser action at present. The angular spread of the coherent radiation beam in the plane perpendicular to the junction plane is about 30°, which corresponds to a coherently emitting region of 6 μ at the junction. Angles as small as 7° were measured in the plane of the junction.

Coherent emission at 3.0 μ , which corresponds to a band-to-band transition, is obtained from n-type ($N_D = 2 \times 10^{16} \text{ cm}^{-3}$) InAs crystals at 11°K by exciting them with 0.84- μ emission of a GaAs p-n junction laser. The angular spread of the coherent radiation beam in the plane perpendicular to the optically excited plane is 9°, which corresponds to a coherently emitting region of 20 μ — over three times larger than the 6- μ value for the diode laser.

I. Melngailis
R. H. Rediker

C. PRESSURE TUNED PbSe DIODE LASER

In this section, we report on the shift to longer wavelength with increasing pressure of the coherent and spontaneous emission from PbSe diode lasers. This work was carried out in collaboration with Dr. J. M. Besson and Professor W. Paul of Harvard University. Stress effects on the light output of diode lasers have previously been studied by using hydrostatic pressure in GaAs¹⁻⁴ and uniaxial compression in GaAs^{5,6} and PbSe.⁷

The PbSe diodes were fabricated by previously described diffusion techniques.⁸ The substrate material was p-type with a carrier concentration of $4.7 \times 10^{17} \text{ cm}^{-3}$ and Hall mobility of $3.3 \times 10^4 \text{ cm}^2 \text{ volts}^{-1} \text{ sec}^{-1}$ at 77°K. Threshold currents were below 5000 amp cm^{-2} at 77°K. The pressure apparatus was similar in design to that used in high pressure experiments with GaAs lasers,¹ the principal new feature being an IRTRAN II window in the pressure vessel. It was found that IRTRAN II could be used at 77°K to pressures over 8 kilobars, providing that the support area of the window was large enough and the pressure was changed slowly. The pressure vessel was immersed in liquid nitrogen. Diode current was supplied in pulses with a repetition rate of 7 kcps, pulse widths between 0.1 and 1 μsec , and amplitudes between 1 and 12 amp. Either a single-pass prism or single-pass grating spectrometer was used. The radiation was detected with a copper-doped germanium detector at 4.2°K, and the signal was amplified with a lock-in amplifier system.

The positions of the dominant cavity modes at each pressure are plotted vs pressure in Fig. I-6. The variation is nearly linear with a slope of $-8.50 \times 10^{-6} \text{ ev/bar}$, which we believe corresponds to the pressure coefficient of the peak of the spontaneous emission. This value is in substantial agreement with the pressure coefficient of $-9 \times 10^{-6} \text{ ev/bar}$ of the optical absorption edge.⁹ The pressure dependence is not strictly linear and higher order terms must be added to account for a slight upward curvature at high pressures. Experiments at higher pressures are needed to obtain a quantitative estimate of this effect. Shifting of individual modes and switching from one mode to another are shown more clearly in Fig. I-7. The modes shift at the rate of $2.5 \times 10^{-6} \text{ ev/bar}$ at 400 bars and $1.6 \times 10^{-6} \text{ ev/bar}$ at 6.5 kilobars. This shift, which is

Section I

due to the change in optical length of the Fabry-Perot cavity, corresponds to a relative variation $(1/n) (dn/dP)$ of about $1.3 \times 10^{-5} \text{ bar}^{-1}$. We have also examined the change with pressure of the spontaneous emission peak from 7.3μ at one atmosphere to 11μ at 7 kilobars. The pressure coefficient was $-8.45 \times 10^{-6} \text{ eV/bar}$. Since the intensity was low, the line broad, and the position of the peak strongly dependent on diode current, this value is less precise than that found by observation of the dominant laser mode. We hope to obtain information about the radiative process from further studies of the spontaneous emission line shape and its variation with pressure and temperature. With current held constant, we observed no significant change in intensity of the coherent or spontaneous emission with pressure.

Extension of this work to 13 kilobars, the freezing pressure of helium at 77°K , should be a straightforward task requiring the development of a suitable window transparent to about 21μ . Higher pressures will require new techniques, but we feel that extension to 20 kilobars, the pressure at which the energy gap of PbSe is expected to close at 77°K , is possible. At room temperature, our PbSe diodes have shown evidence of carrier injection to 25 kilobars. At long wavelengths, free carrier absorption in the active region and diffraction will become more important loss mechanisms. Weak interaction with phonon modes of the crystal should not begin before 40μ .

J. F. Butler
A. R. Calawa
R. H. Rediker

D. MAGNETOEMISSION STUDIES OF PbS, PbTe, AND PbSe DIODE LASERS

1. Introduction

Magnetic field effects on the light output from forward biased p-n junctions have been studied in a number of III-V semiconductors.¹⁰ Such experiments provide information about the states involved in the radiative process. In this section, we describe the action of a [100] oriented magnetic field on the spontaneous and laser emission from diodes of the lead salt semiconductors (PbS, PbTe, and PbSe). From measurements of polarization, splitting and rate of shift to higher energies, spontaneous emission peaks are correlated with transitions between sublevels of spin-split, $l = 0$ Landau levels. These results give information about low energy transitions which could not be measured in magnetoabsorption experiments¹¹⁻¹³ because of high carrier concentrations and consequent band filling. Above threshold, shifting of individual modes due to a dependence of the refractive index on magnetic field is observed.

2. Landau Levels in the Lead Salts

The lead salt semiconductors possess fourfold direct minimum energy gaps at point L on the Brillouin zone face.¹⁴ Band-edge parameters (effective mass and g-factor) of valence and conduction bands are of comparable magnitude, and constant energy surfaces at both band edges are prolate ellipsoids with major axes in $\langle 111 \rangle$ directions. The band structure of the lead salts is determined in part by strong spin-orbit interaction. Both valence and conduction bands have only the twofold spin or time-reversal degeneracy.

A magnetic field lifts the twofold degeneracy and produces spin-split Landau levels. The energies of the sublevels of an l^{th} order Landau level in, for example, the conduction band are given by¹⁵⁻¹⁷

$$E_\ell = E_c + (\ell_c + \frac{1}{2}) \hbar \omega_c \pm \frac{1}{2} g_c \beta B \quad (1)$$

where E_c is the zero-field conduction band energy, $\hbar \omega_c$ is the cyclotron energy, g_c is the conduction band g -factor, β is the Bohr magneton, and B is the magnetic flux density. Figure I-8 shows schematically the type of Landau level spectrum expected in a lead salt semiconductor.

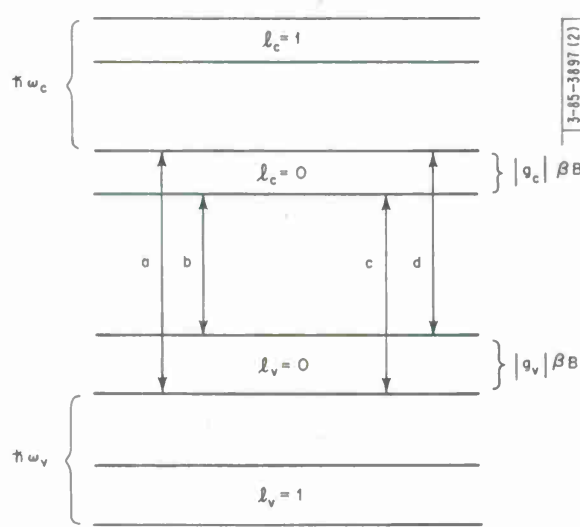


Fig. I-8. Landau level spectrum for a semiconductor with twofold degenerate valence and conduction bands. First two levels and possible transitions between $\ell = 0$ sublevels are shown.

The $\ell = 0$ and $\ell = 1$ levels are shown for valence and conduction bands. Dipole transitions across the gap are restricted by the well-known selection rule¹⁵⁻¹⁷ that ℓ must be conserved, and the transitions allowed by this rule are shown for $\ell = 0$. A similar set of transitions connects the higher Landau levels. Because of the large spin-orbit interaction, the sublevels of a given spin-split Landau level would be expected to contain both spin-up and spin-down components. Hence transitions involving spin reversal are allowed, and the four optical transitions shown in the figure could be expected for each value of ℓ . If certain simple selection rules are applicable,¹⁴⁻¹⁷ radiation associated with a spin reversal should be linearly polarized perpendicular to the magnetic field when propagating perpendicular to the field (σ -emission), and radiation associated with spin conservation should be linearly polarized in the direction of the magnetic field (π -emission). These rules are analogous to those governing the polarization of light in the atomic Zeeman effect.

Magnetoabsorption experiments¹¹⁻¹³ have shown that valence and conduction band g -factors in all three lead salts have opposite sign and approximately equal magnitude. This result implies that transitions c and d in Fig. I-8 are spin-reversing and of nearly equal energy while transitions a and b are spin-conserving. The polarization rules discussed above were found to be valid for magnetoabsorption in PbS and PbSe.¹¹

3. Experiment

The fabrication of lead salt diode lasers has been described elsewhere.¹⁸⁻²⁰ The units used in the present work were of good quality, having threshold current densities between 200 and

Section I

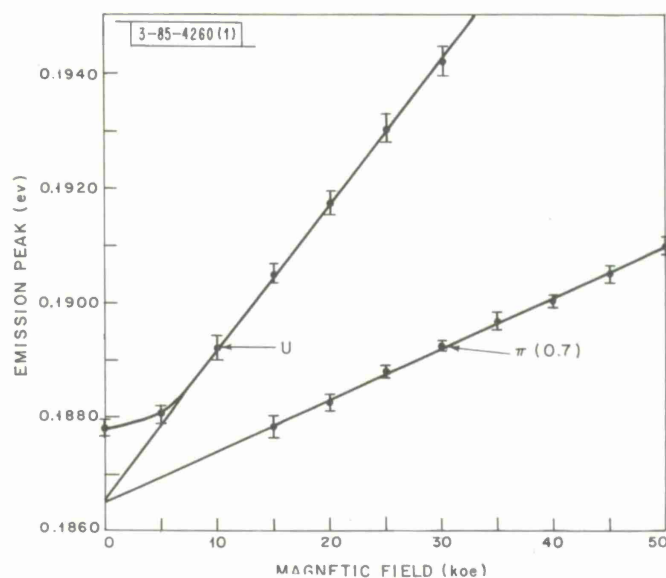


Fig. I-9. PbTe injection luminescence. Variation of spontaneous emission peak with [100] oriented magnetic field. $T = 10^\circ\text{K}$, $J = 480 \text{ amp cm}^{-2}$.

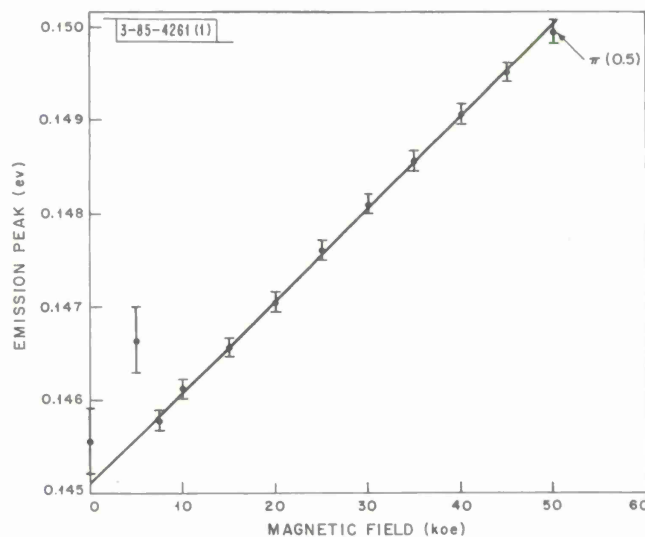


Fig. I-10. PbSe injection luminescence. Variation of spontaneous emission peak with [100] oriented magnetic field. $T = 10^\circ\text{K}$, $J = 320 \text{ amp cm}^{-2}$.

500 amp cm^{-2} at 10°K and in the absence of a magnetic field. Although continuous operation was possible, diode currents were chopped at 7 kcps in order to make use of a lock-in amplifier system. The diodes were mounted in the core of a solenoidal superconducting magnet of 50-koe capability and were oriented with magnetic field in the [100] crystallographic direction, parallel to the diode current and perpendicular to the emitted radiation. The conduction-cooled diodes were at a temperature of approximately 10°K . Spectra were measured with a single-pass grating spectrometer. A copper-doped germanium detector was used for PbTe and PbSe emission, and a photovoltaic InSb detector was used for PbS. Polarization measurements were made with a six-plate AgCl pile-of-plates polarizer which was rotated through 180° in 10° increments. The light path outside of the dewars was maintained in a dry nitrogen atmosphere.

4. Spontaneous Emission

In the first set of measurements, current was held at a constant value below threshold while the magnetic field was varied. Spectra were obtained and the spectral positions of the peaks were recorded as functions of magnetic field intensity. Polarization was measured at selected points. Since the spontaneous radiation intensity increased and threshold currents decreased with increasing magnetic field, it was, in some cases, not possible to obtain a spectrum at zero magnetic field.

Results for a PbTe diode are shown in Fig. I-9. The estimated limits of error in the determination of the position of each spectral peak are indicated. Two emission maxima shifting linearly to higher energies with increasing magnetic field were observed. The upper peak decreased in intensity with field and could not be observed beyond 30 koe. Polarization was measured at the indicated points. The notation π (0.7) signifies that the radiation was polarized parallel to the magnetic field and that the degree of polarization was 70 percent; radiation at point U was unpolarized. The upper line in Fig. I-9 can be identified with the nearly degenerate pair of spin-reversing transitions between $\ell = 0$ Landau levels (c and d of Fig. I-8). For $|g_v| = |g_c|$, the slope of this line gives the reduced effective mass directly as $|m_r| = 0.22 m_0$, in agreement with the magnetoabsorption work.^{11,12} The fact that the emission is unpolarized indicates that the simple polarization rules discussed in the previous section are not valid for this case and agrees with the magnetoabsorption results. The lower line in Fig. I-9 then corresponds to the lowest energy, spin-conserving transition (b of Fig. I-8). Here the polarization has the expected π -orientation. This transition apparently was not resolved in the magnetoabsorption work at 77°K . From the energy difference between the two lines in Fig. I-9 as a function of magnetic field, the magnitude of the conduction and valence band g -factor is calculated to be 29.

Figure I-10 shows results for a PbSe diode. This diode exhibits a single emission peak beyond 5 koe which can be identified from its polarization and from the slope of the line in Fig. I-10 with the lowest energy, spin-conserving transition between $\ell = 0$ Landau levels (b of Fig. I-8). The single line in Fig. I-10 is insufficient to determine both m_r and $|g_v|$ or $|g_c|$ uniquely. By using the value $m_r = 0.028 m_0$ from the magnetoabsorption work¹¹ and the slope of the line in Fig. I-10, we find $|g_v| = |g_c| = 19$, in agreement with the magnetoabsorption value.

The shift of the spontaneous emission peak with magnetic field for a PbS diode is shown in Fig. I-11. The polarization data indicate that the upper line is associated with a spin-conserving

Section I

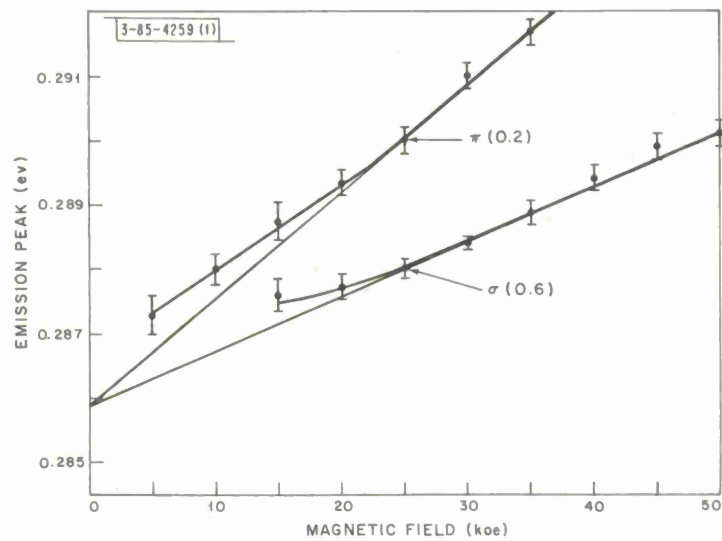


Fig. I-11. PbS injection luminescence. Variation of spontaneous peak with [100] oriented magnetic field. $T = 10^\circ\text{K}$, $J = 430 \text{ amp cm}^{-2}$, $n = 3 \times 10^{18} \text{ cm}^{-3}$.

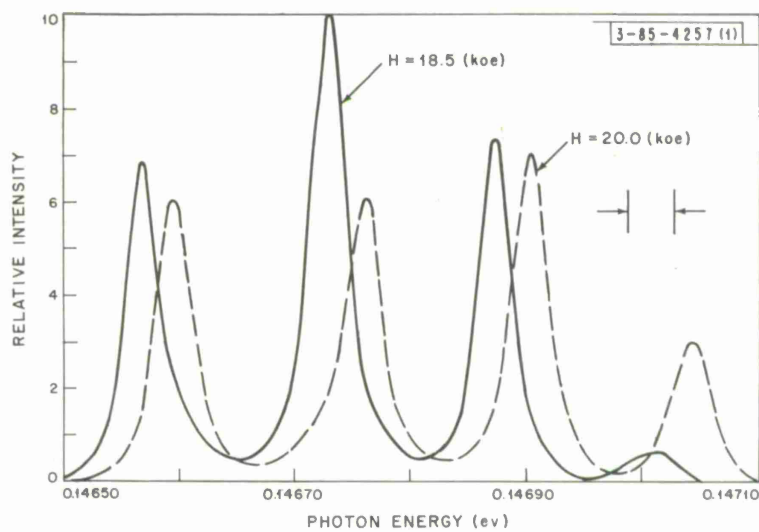


Fig. I-12. Multimode laser emission from a PbSe diode laser for two values of [100] oriented magnetic field. $T = 10^\circ\text{K}$, $J = 400 \text{ amp cm}^{-2}$.

and the lower line with a spin-reversing transition. The slopes of the linear regions indicate that the transitions are between $l = 0$ Landau levels. Thus, the upper line can be identified with the transition a and the lower line with c and/or d of Fig. I-8. The assumption that $|g_v| = |g_c|$ leads to a reduced effective mass, in poor agreement with published values. For $|g_v| \neq |g_c|$, Fig. I-11 does not give enough information in order to calculate the three quantities $|g_v|$, $|g_c|$, and m_r uniquely. However, the data are consistent with the values $m_r = 0.05 m_0$, $|g_v| = 7.0$, and $|g_c| = 11.5$, which can be compared with the magnetoabsorption values^{11,13} $m_r = 0.050 \pm 0.002$ obtained at 4.2°K, and $|g_v| = 8.5 \pm 1.5$ and $|g_c| = 10.0 \pm 1.5$ obtained at 77°K. The emission peaks do not follow the linear variation of the Landau levels at low fields. This appears to be a band filling effect and will be studied in more detail during the next quarter.

5. Laser Emission

Laser action associated with spin-conserving and spin-reversing transitions has been observed in diodes of all three lead salts in a magnetic field. Laser emission moves to higher energies with increasing magnetic field intensity by the growth and decay of mode intensities and by shifting of mode positions. This is shown in Fig. I-12 where emission spectra of a PbSe diode biased above threshold are presented for two values of magnetic field. Mode positions are plotted against magnetic field intensity in Fig. I-13. The change in refractive index with magnetic field is related to the mode shift by

$$\left(\frac{\partial n}{\partial H}\right)_E = - \frac{ch}{2LE\Delta E} \frac{dE}{dH} \quad (2)$$

where L is the distance between the reflecting end faces of the Fabry-Perot cavity, E is the photon energy of the emitted radiation, ΔE is the energy spacing between cavity modes, and

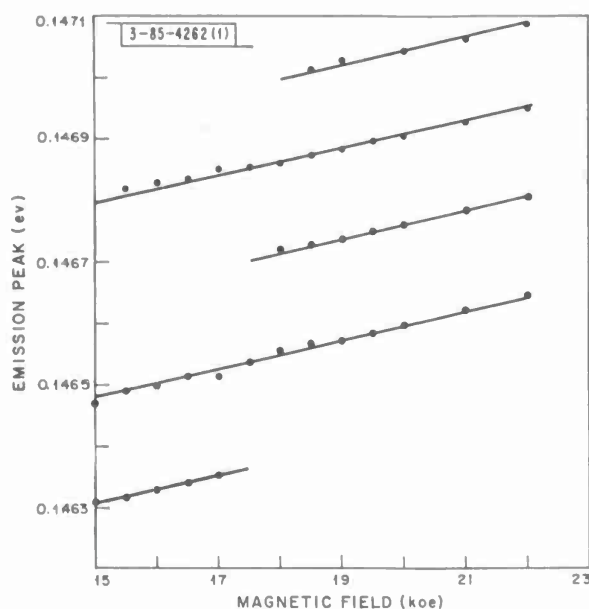


Fig. I-13. Multimode laser emission from a PbSe diode laser. Dependence of mode position on magnetic field. $T = 10^\circ\text{K}$, $J = 400 \text{ amp cm}^{-2}$.

Section I

dE/dH is the rate of change in mode position with magnetic field. By using the data of Fig. I-13 and 500μ for L , $(\partial n/\partial H_{[100]})_E = -1.3 \times 10^{-6} \text{ oe}^{-1}$ is obtained for PbSe. For PbTe, similar data obtained near 40 koe give $(\partial n/\partial H_{[100]})_E = -1.2 \times 10^{-6} \text{ oe}^{-1}$.

J. F. Butler
A. R. Calawa

E. GUNN EFFECT IN COMPOUND SEMICONDUCTORS

The following summarizes a Technical Report²¹ which is in the process of publication.

A theoretical and experimental study of the Gunn effect is presented. It appears that this effect, originally observed by Gunn as a time variation in the current through ohmic samples of n-GaAs when the sample voltage exceeded a critical value, can be accounted for by the transferred electron model of Ridley and Watkins. This model is based on a transfer of electrons, as the electron temperature is increased by the applied electric field, from a low-mass, high-mobility conduction band that is lowest in energy to a higher-mass, low-mobility band. If the transfer occurs rapidly enough as the electric field is increased, a bulk differential negative resistance will be realized, which then leads to the formation of domains of different electrical conductivity which move through the sample, giving rise to a time-varying current.

Most of the experimental results for n-GaAs verify this interpretation. The shape of the current vs time waveform for the longer samples ($l \sim 100$ to 1000μ) — sharp spikes in current separated by flat valleys in current — and the observed independence of threshold electric field (2300 to 4000 volts/cm) on sample length are shown to be consistent with a negative resistance model. The value of electric field which characterized the regions of high conductivity, about 1500 volts/cm, is found to be independent of sample length as expected. In addition, the voltage across the high electric field domain is found to scale with sample length, also as expected, and the value of electric field which characterizes the regions of low conductivity is estimated to be $\geq 60,000$ volts/cm. The effects of temperature on the threshold electric field and threshold electron drift velocity are consistent with the transferred electron model. For short samples ($l \sim 25$ to 100μ), a sinusoidal current vs time waveform is seen, and for samples in the 100μ length range, the sinusoidal mode is seen near threshold and the spike mode is seen well above threshold. Although the sinusoidal mode is not predicted by the simplest form of the model, the effects of magnetic field and termination impedance on this mode are consistent with the interpretation of this mode as a longitudinal disturbance caused by a negative resistance.

The Gunn effect has also been observed in n-CdTe, and resistance vs hydrostatic pressure experiments show that the transferred electron model is a reasonable explanation for this material as well.

Finally, the absence of an instability in n-InSb and n-InAs is shown to be consistent with the transferred electron model. The higher conduction band minima in these materials are probably sufficiently separated from the lowest minimum that other effects such as carrier multiplication will occur before transfer, and no negative resistance is to be expected.

A. G. Foyt, Jr.
A. L. McWhorter

REFERENCES

1. J. Feinleib, S. Groves, W. Paul and R. Zallen, Phys. Rev. 131, 2070 (1963).
2. T.A. Fulton, D.B. Fitchen and G.E. Fenner, Appl. Phys. Letters 4, 9 (1964).
3. G.E. Fenner, Phys. Rev. 137A, 1000 (1965).
4. M.J. Stevenson, J.D. Axe and J.R. Lankard, IBM J. Res. Develop. 7, 155 (1963).
5. D. Meyerhofer and R. Braunstein, Appl. Phys. Letters 3, 171 (1963).
6. R.C. Miller, F.M. Ryan and P.R. Emtage, Proceedings of the Symposium on Radiative Recombination in Semiconductors, Paris, 1964 (Dunod, Paris, 1965), pp. 209-215.
7. A.R. Calawa, J. F. Butler and R.H. Rediker, Bull. Am. Phys. Soc. 10, 84 (1965).
8. J.F. Butler, J. Electrochem. Soc. 111, 1150 (1964).
9. V. Prakash and W. Paul, to be published.
10. For a review of this work, see F.L. Galeener, I. Melngailis, G.B. Wright and R.H. Rediker, J. Appl. Phys. 36, 1574 (1965).
11. D.L. Mitchell, E.D. Palik and J.N. Zemel, Proceedings of the International Conference on the Physics of Semiconductors, Paris, 1964 (Dunod, Paris, 1964), pp. 325-333.
12. D.L. Mitchell, E.D. Palik, J.D. Jensen, R.B. Schoolar and J.N. Zemel, Bull. Am. Phys. Soc. 9, 292 (1964).
13. E.D. Palik, D.L. Mitchell and J.N. Zemel, Phys. Rev. 135, A763 (1964).
14. See, for example, J.O. Dimmock and G.B. Wright, Phys. Rev. 135, A821 (1965).
15. R.J. Elliott, J.P. McLean and G.G. Macfarlane, Proc. Phys. Soc. (London) 72, 553 (1958).
16. E. Burstein, G.S. Picus, R.F. Wallis and F. Blatt, Phys. Rev. 113, 15 (1959).
17. L.M. Roth, B. Lax and S. Zwerdling, Phys. Rev. 114, 90 (1959).
18. J.F. Butler, A.R. Calawa, R.J. Phelan, Jr., T.C. Harman, A.J. Strauss and R.H. Rediker, IEEE Solid-State Device Res. Conf., Boulder, Colorado, 1-3 July 1964; Appl. Phys. Letters 5, 75 (1964).
19. J.F. Butler, A.R. Calawa, R.J. Phelan, Jr., A.J. Strauss and R.H. Rediker, Solid State Commun. 2, 303 (1964), DDC 453105.
20. J.F. Butler and A.R. Calawa, Meeting of the Electrochemical Society, San Francisco, 9-13 May 1965.
21. A.G. Foyt, Jr., "Gunn Effect in Compound Semiconductors," Technical Report 385, Lincoln Laboratory, M.I.T. (7 July 1965), in publication.

II. LASER RESEARCH

A. PERTURBATION OF REFRACTIVE INDEX OF ABSORBING MEDIA BY A LASER BEAM

Previously, we reported work in which liquid absorbing media was used.¹ The present work has been carried out with ammonia gas instead of monoethylamine as the absorber in order to study laser propagation through a simple gas. By using the same experimental apparatus slightly modified, we have made measurements of the optical disturbance created by a neodymium glass laser in a one-meter cell of ammonia gas at about 110-psi gauge pressure, in which 10 percent of the neodymium energy is absorbed. This pressure is chosen for maximum absorption but must be slightly less than the vapor pressure over the liquid at room temperature in order to keep condensation from forming on the cell windows.

By varying the gas pressure, any absorption from 0 to 10 percent may be selected, the perturbation of the index of refraction scaling accordingly.

As before, pictures of the interferometer fringes created by a pulsed argon laser are photographed by imaging the neodymium beam exit end of the absorption cell on the film. With each interferometer picture, a measurement is made of the corresponding total integrated energy in the neodymium beam up to the time the interferometer is illuminated. Since the distribution of energy, as well as the total energy in the neodymium beam, determines the details of the disturbance in the absorber, we have utilized a vidicon camera system with a single-line A-scope readout to give a profile of the neodymium beam.

It is found that up to at least 3 joules/cm²* the neodymium beam produces an index profile in the absorber which is almost identical to the energy distribution profile of the neodymium beam as it enters the absorber. The neodymium energy distribution at the absorption cell exit, however, has been altered by both the original laser beam divergence and by the divergent effect of the index profile through which it passes. Figure II-1 shows energy profiles across the center



Fig. II-1. Energy profile along a diameter of cross section of neodymium laser beam at cell entrance (solid line) and cell exit (dashed line). Argon laser phase front along a diameter of cross section of disturbance at cell exit (dotted line).

* Values of energy/unit area greater than this give too large a number of fringes to be accurately measured and plotted.

Section II

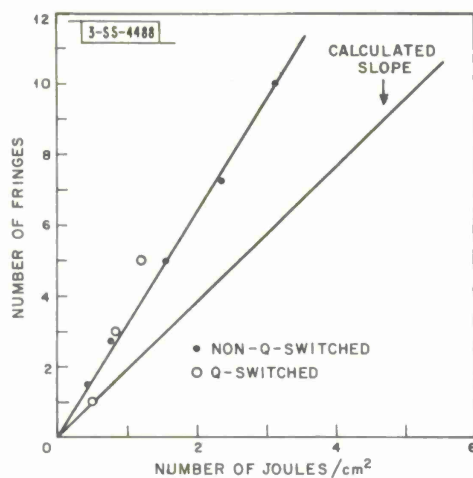


Fig. II-2. Number of interferometer fringes at center of disturbance created in one meter of ammonia gas at 110 psi plotted against number of joules/cm² in the neodymium laser beam at that point.

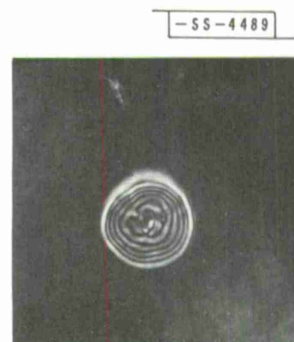


Fig. II-3. Typical interferogram of disturbance created in one meter of ammonia gas by a non-Q-switched 1/4-inch-diameter neodymium laser beam.

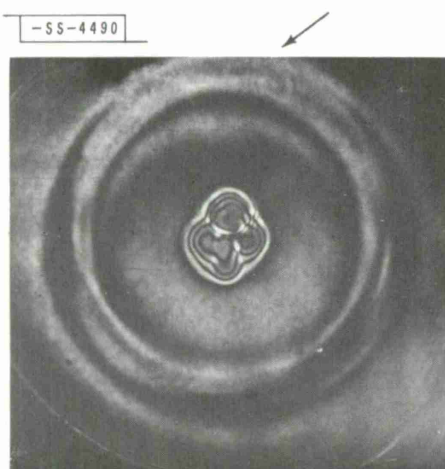


Fig. II-4. Typical interferogram of disturbance created in one meter of ammonia gas by a Q-switched 1/4-inch-diameter neodymium laser beam. Arrow indicates the cylindrical sound wave.

of the neodymium beam at the absorption cell exit and entrance, along with the corresponding profile of the argon phase front at the cell exit. The tails on the argon phase front, as compared to the entering neodymium beam, are due to the original neodymium laser beam divergence of, in this case, about 0.5 mrad acting over the one-meter-cell length. The longer tails of the neodymium exit profile are caused by the divergent effect of the disturbed index of refraction of the absorbing medium.

In order to compare the interferometer fringe shift with the neodymium energy/unit area which causes the shift, we have numerically integrated the neodymium entrance beam profile by using the measured total energy to give the energy/unit area at any point on the disturbance. The number of fringes at the center of the disturbance is plotted against the corresponding energy/unit area for one meter of ammonia gas at 110 psi (Fig. II-2). A typical interferometer picture is shown in Fig. II-3, the disturbance being approximately $\frac{1}{4}$ inch in diameter.

The slope of the straight line passing through the data in Fig. II-2 should correspond to

$$\text{slope} = \frac{(n-1) \beta a}{\rho C_p \lambda} = 1.92 \quad (1)$$

where

n = index of refraction of the absorber at 4880 Å

ρ = density of the absorber

C_p = specific heat at constant pressure

λ = wavelength of the interferometer illumination

β = volume expansivity

a = total cell absorption

The measured slope is larger than the predicted value by a factor of about 1.7 for this case. There is approximately the same discrepancy for the liquid and monoethylamine gas absorbers. In all cases, the number of fringes observed has been substantially greater than predicted. Because of an unexpectedly large divergence of the unperturbed laser beam used with the original long cell measurements in monoethylamine gas, the energy/unit area had been overestimated, thereby accounting for the too few fringes that had been seen previously for that absorber. The value of dn/dT , the thermal coefficient of the index, has been measured directly for a number of absorbers and is found to be identical to $(n-1) \beta$ as assumed in Eq. (3). Saturation of the absorption would give a nonlinear response, and too few fringes, contrary to observation. Also, there is no evidence of slow relaxation of the specific heat when the high frequency vibrational modes which are excited by the laser transfer their energy to translational motion. The discrepancy with Eq. (3) is still unexplained.

Results of firing a Q-switched laser beam through ammonia gas give two distinct disturbances, as reported previously,¹ for liquid absorbers: (1) the normal rarefaction at the center which remains stationary, and (2) a pressure wave which radiates outward at the sonic velocity. A typical interferometer picture, taken about 25 μ sec after the Q-switched pulse, is shown in Fig. II-4. The cylindrical sound wave is the large diameter disturbance indicated by the arrow.

Section II

The energy/unit area vs the peak number of fringes in the stationary disturbance has also been plotted in Fig. II-2 for the Q-switched neodymium laser beam. Because the neodymium energy distribution is neither as symmetric nor as smooth as it is with the non-Q-switched laser, the numerical integration is less accurate and the data points show greater scatter. The fact that they still lie about the line drawn through the non-Q-switched data points indicates that the processes involved depend upon the laser energy rather than the laser power. This is consistent with the observation in the non-Q-switched case that the number of fringes is determined solely by the total energy deposited up to the time the fringes are observed.

P. R. Longaker
M. M. Litvak

B. STARK LINEWIDTH MEASUREMENT OF ION DENSITY IN AN ARGON ION LASER

The moderately high ion and electron densities of about $10^{14}/\text{cm}^3$ in a small bore argon ion laser tube have been determined from the Stark-broadened linewidths of particular neutral argon lines, for which the Doppler linewidth is much less even at operating gas temperatures as high as 4000°K . This is an improvement over the usual technique of using hydrogen as an impurity in the tube to measure the hydrogen Stark linewidths because the hydrogen Doppler linewidths are comparable to the Stark linewidths at moderate electron densities, and extraction of the density data from the linewidth is difficult and can be unreliable.

Figure II-5 shows the electron density n_e vs discharge current as measured from the linewidth (also indicated) of the $5495\text{-}\text{\AA}$ neutral argon line (not a laser transition) emitted from an argon ion laser tube. The Doppler linewidth has not been subtracted and as indicated, even at 4000°K , it is below the linewidth measured at as little as 0.5 amp.

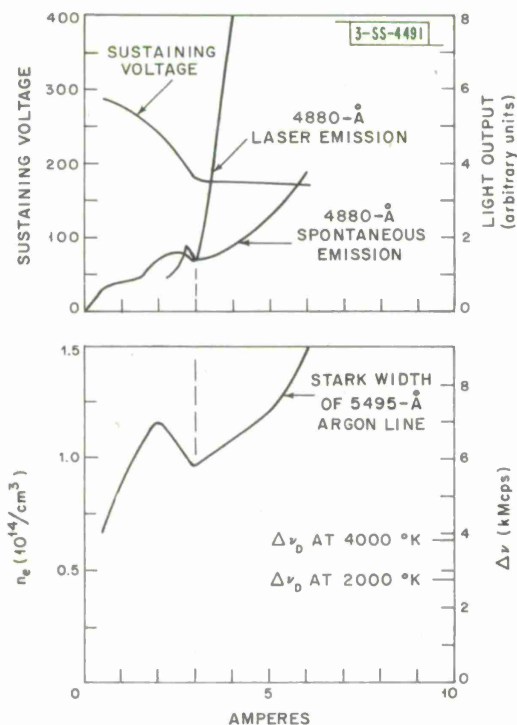


Fig. II-5. Laser tube voltage, 4880-Å laser and spontaneous emission, electron density, and 5495-Å neutral argon linewidth as functions of discharge current. Argon ion laser: bore 1.5 mm, length 20 cm.

Data indicate that the gas temperature on the axis at 6 amp would be roughly 2000°K. Current densities as high as 340 amp/cm² and electron densities of 10¹³/cm³ to 10¹⁴/cm³ were measured from the linewidths over the indicated current range. The Stark broadening is a slow function of the electron temperature.² An electron temperature of approximately 20,000°K was assumed, as suggested by data on ratios of line intensities. The complicated behavior of the linewidth at low currents reproduces itself especially near the dip at 3 amp in the 4880-Å laser and spontaneous emission, and in the voltage across the tube, as shown in Fig. II-5. The value of the current at the dip is expected to depend upon tube radius and pressure. This drop in electron density occurs because of an increase in mobility, possibly due to the decrease of the electron-neutral-atom collision cross section (Ramsauer minimum) at about 1-ev electron energy.³

This linewidth technique will be applied for laser conditions of higher currents in a strong magnetic field. The ion densities then obtained will give important information about the limitations on laser action due to resonance radiation trapping by ground state ions and about the improvement of power efficiency with arc constriction by the magnetic field.

R. J. Carbone
M. M. Litvak

C. HIGH PRESSURE MERCURY LASER

Laser oscillation was not obtained with the mercury discharge described previously.⁴ An internal mirror laser tube containing the lowest-loss mirrors attainable was constructed to operate at high temperature (about 280°C) in order to obtain a high optical quality cavity for this low gain transition. The tube had an 18-mm bore and a 35-cm active length. The electrodes were coaxial to the tube axis.

Photographic measurements of the arc size were made as a function of current at several pressures. This indicated a lower value of band radiation per cm³ of discharge than estimated previously. The solid straight line in Fig. II-6 shows data⁵ previously reported at 96 torrs, assuming an earlier estimate of constant arc diameter equal to 2.5 mm. The lower curve is obtained from the same watts of emission but corrected for the measured arc area. The gain, as calculated from the spontaneous emission produced at 96 torrs or higher pressures, is less than 0.14 percent/meter which is too small compared to the mirror losses. Furthermore, the mirror reflectivity probably decreases and the loss increases over room temperature figures at the elevated operating temperatures. Nearly optimum green band output and discharge stability occurred at 96 torrs.

The ratio of peak power density emitted in the green band to the input electrical power density is plotted as a dashed line in Fig. II-6. This indicates a low power efficiency of 2×10^{-5} . However, the population in the radiating state is about 4 percent of the maximum number possible at this pressure.

The green band at the highest currents is still, most likely, emission from the mercury molecule and not from the plasma. Rough estimates of the electron density (10¹⁵/cc) and temperature (6000°K) in this discharge indicate that electron continuum radiation, free-free radiation (emitted by an electron going between continuum states), and free-bound radiation (emitted by an electron going between a continuum and a bound state) contribute less than 10⁻² watt/cc to the radiation observed in the green band. The absorption coefficient for the inverse processes

Section II

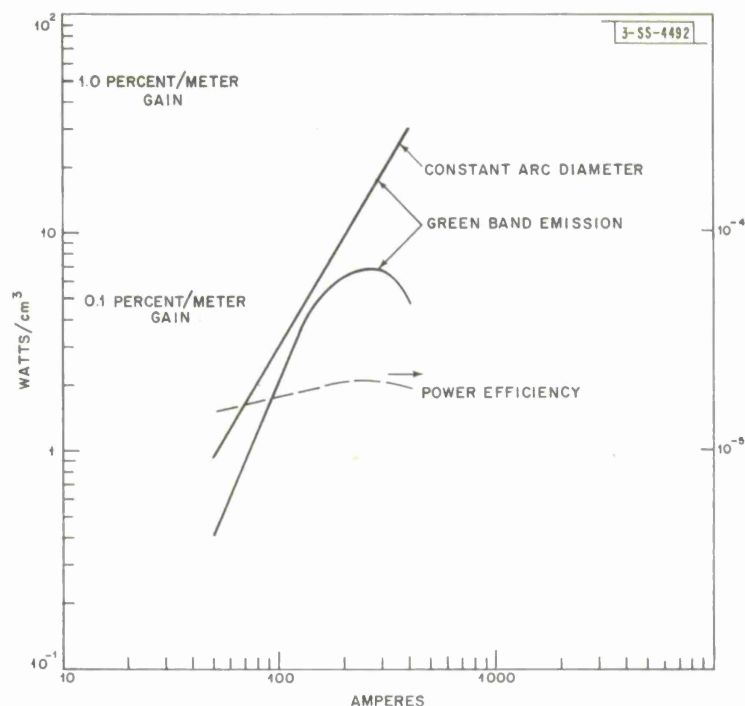


Fig. II-6. Power output and power efficiency in the mercury vapor green band as a function of pulsed arc current at 96 torrs (260°C). Laser gains for 50 and 5 watts/cc are also indicated. Argon partial pressure was 25 torrs.

is smaller than 0.1 percent, especially for wavelengths greater than 4950 \AA , but might exceed the laser gain at much higher currents. Until density measurements from Stark linewidths are successfully made for this discharge, these estimates may yet prove to be too conservative.

Designs for a laser tube in which the discharge region and the laser region are well-separated are being considered. The metastable laser-molecule can easily diffuse several millimeters in its radiative lifetime. This would prevent dissociation or excitation of the laser molecule by impact and also avoid photon absorption by the plasma.

R. J. Carbone
M. M. Litvak

D. PHOTOCURRENT SPECTRUM AND PHOTOELECTRIC COUNTS PRODUCED BY A GASEOUS LASER

A paper of this title has been submitted to The Physical Review. The abstract reads as follows:

"The anode-current spectrum of a photomultiplier illuminated by light of time varying intensity is obtained theoretically. The moments of the photoelectron counts under the same conditions are derived. The expressions are evaluated for the case of light emitted from a laser oscillator by using a semiclassical theory of the van der Pol oscillator.

"The theoretical predictions are compared with experiments in which the spectrum of the photomultiplier was observed in the range 0-17 Mc and counts were recorded for counting intervals ranging between 10^{-6} and 10^{-1} sec. The three lowest order factorial moments were evaluated as functions of T and compared with theory. The spectral data are used to predict the counting data and a comparison is made. The signal-to-noise ratio of the two types of experiments is evaluated and found to be comparable."

C. Freed
H. Haus*

E. MULTIPLE STIMULATED BRILLOUIN SCATTERING IN SOLIDS

The optical scattering part of this experiment in quartz has been completed. The experimental setup is shown in Fig. II-7. As many as six successive Brillouin shifts have been observed as a result of iterative scattering and reamplification in the ruby rod over at least 3 cm^{-1} of the ruby linewidth. Figure II-8 shows an example. Only Stokes waves are generated in this experiment, which can be understood from considerations of the Brillouin conversion efficiency and ruby gain.

It is essential that the laser line be unequivocally identified in the etalograms in order to establish the possible presence of frequency up-shifts (anti-Stokes lines). In the radiation returned from the sample, the laser line can easily be weaker than the first Brillouin shift because the laser radiation is only scattered in the backward direction, whereas Brillouin waves are actually generated backward with moderately large conversion efficiencies. If the Brillouin waves undergo amplification in the ruby rod, then successive shifts can appear more intense than the laser.

The method which provided identification of the laser line in the interferograms was temperature control of the ruby rod. The laser emission of ruby shifts roughly 0.2 cm^{-1} per degree so that firings at temperatures controlled to within 0.01° produced essentially the same laser line in successive etalograms. In all cases examined by this method, the laser turned out to be the highest frequency line although it was also the weakest or near the weakest. In fact, in many etalograms, laser radiation did not appear at all. Thus, for example, Fig. II-9 shows six Stokes shifts with the laser line brought out only by optical enhancement (a reflector opposite the etalon and beam splitter) in a separate firing held to within 0.01°C .

The velocity of sound calculated from all the data is $5.75 \times 10^5 \text{ cm/sec} \pm 1$ percent at 25.5 kMcps, using the relation $\Delta\omega/\omega = 2v(c/n) \sin(\phi/2)$, where $\Delta\omega$ is the frequency shift, ω is the laser frequency, c/n is the velocity of light in the medium, v is the acoustic velocity, and ϕ is the scattering angle.

Figure II-10 shows the intensity profiles estimated from some typical etalon rings. The intensity of a particular Brillouin line is proportional to the product of quartz conversion efficiency times ruby amplification factor, diminished by the beam divergence, so that the profile can be interpreted qualitatively by assuming the following possible parameters. The laser oscillates near line center, and the gain for the Stokes waves might be 10 near the center, falling to 1 near one line edge. A Brillouin conversion efficiency of 10 to 25 percent, especially if it is

* Department of Electrical Engineering, M.I.T.

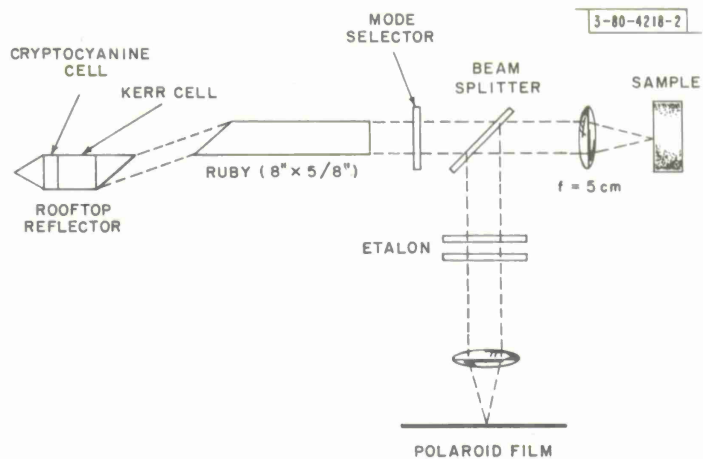


Fig. II-7. Experimental setup for detection of stimulated Brillouin scattering in solids. Laser was operated between 25 and 500 Mw over roughly 1 cm² and 2 cm² areas, respectively.

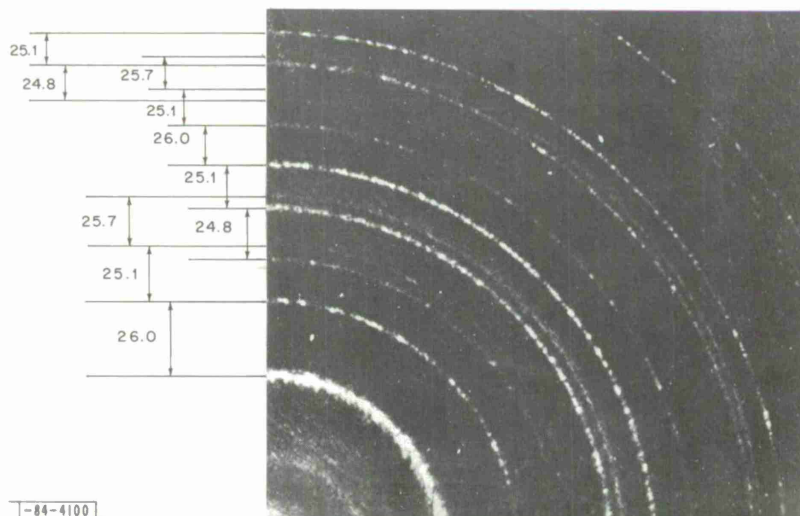


Fig. II-8. Etalogram of backscattered radiation from x-cut quartz crystal. In original photograph, five shifts can be measured. Interorder spacing is 94.5 kMcps. Shifts interlace because total of all shifts exceeds interorder spacing.

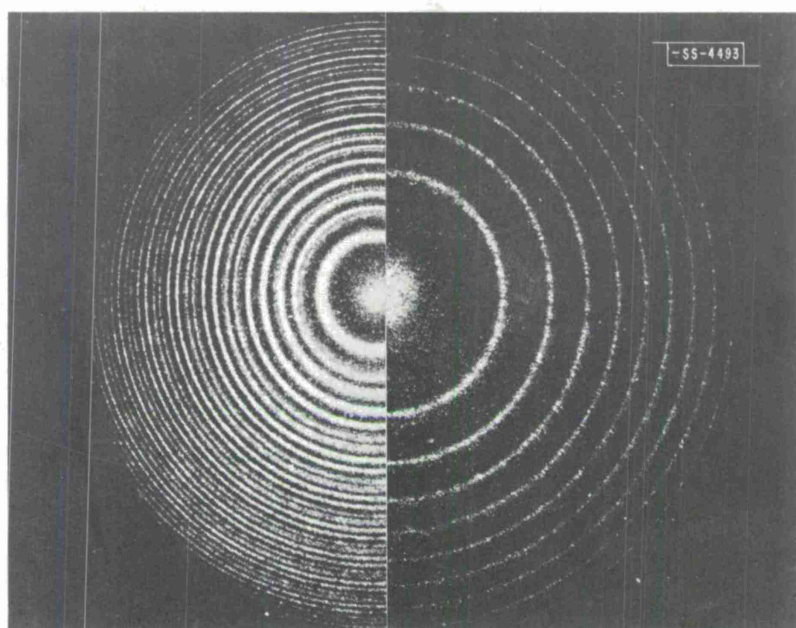


Fig. II-9. Quartz. Six lines on left half of picture are all Stokes shifts measured in the backward direction; laser is on right half. Average shift is 25.5 ± 0.2 kMcps

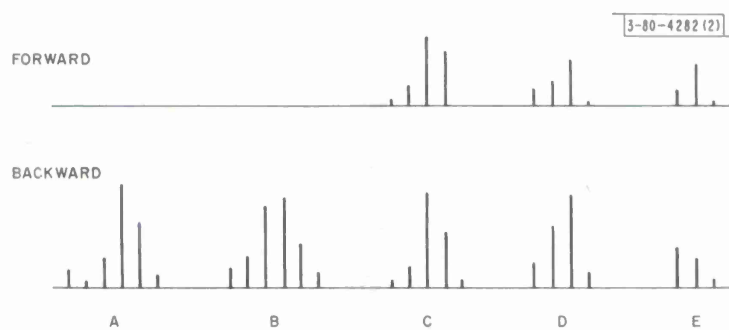


Fig. II-10. Intensity profiles of several typical etalon rings. Highest frequency is at left; spacings average to 25.5 ± 0.3 kMcps.

Section II

nonlinear with incident power, can thus result in the types of patterns observed. Furthermore, this scheme can explain why the backward phonons required for anti-Stokes scattering are not generated: prior to reamplification, the backward Stokes waves are never more intense than the primary laser source.

High power stimulated Brillouin scattering experiments are being continued in order to detect the associated coherent microwave phonon pulses.

P. E. Tannenwald
F. H. Perry
E. Walters

REFERENCES

1. Solid State Research Report, Lincoln Laboratory, M.I.T. (1965:1).
2. H.R. Griem, Plasma Spectroscopy (McGraw-Hill, New York, 1964).
3. R.B. Brode, Rev. Mod. Phys. 5, 257 (1933).
4. Solid State Research Report, Lincoln Laboratory, M.I.T. (1964:2), DDC 606126, H-606.
5. Solid State Research Report, Lincoln Laboratory, M.I.T. (1964:4), DDC 613961, H-639.

III. MATERIALS RESEARCH

A. SINGLE-CRYSTAL GROWTH OF COBALT-DOPED ZnAl_2O_4

Single crystals of zinc aluminate lightly doped with divalent cobalt have been grown from a flux of lead oxyfluoride in order to obtain samples for measuring the nuclear hyperfine field of tetrahedrally coordinated Co^{+2} . Weighed amounts of flux and $\text{Zn}_{0.999}\text{Co}_{0.001}\text{Al}_2\text{O}_4$ in the ratio 6:1 were ground together by hand, sealed in a 250-cc platinum crucible, and fired to 1300°C . After soaking for 48 hours, the melt was slowly cooled to 850°C at a rate of 5°C per hour. Numerous crystals possessing an octahedral habit and ranging in size from 1 to 6 mm across a cube face were formed on top of the melt. The crystals were separated from the flux by hand and then leached in acetic acid-sodium acetate. It is expected that the extent of Co^{+2} doping varies in the crystallites, all of which were blue and transparent, as expected for a Co^{+2} concentration of about 0.1 percent.

D. B. Rogers
R. Germann
A. Ferretti

B. SINGLE-CRYSTAL GROWTH AND PROPERTIES OF LaVO_3 AND YVO_3

Metallic conductivity in oxides whose structures are related to that of ReO_3 (including perovskites and the tungsten bronzes) has been interpreted with a model^{1, 2} involving overlap of B-site cation d-wave functions with anion-near-neighbor p_σ - or p_π -orbitals, resulting in the formation of partially occupied σ^* - or π^* -antibonding bands. For a given series of transition metal cations having the same formal charge, these bands are expected to decrease in width with increasing electronic spin on the cation. On the other hand, an increase of formal charge on the cation results in increased polarization of the anion wave functions and larger bandwidth. These trends are clearly illustrated by the properties of perovskite-type oxides ABO_3 in which the B-cation is in the first transition series.³ LaTiO_3 and CaVO_3 , where Ti^{+3} and V^{+4} ions have an electronic configuration $t_{2g}^1 e_g^0$, are Pauli paramagnetic and metallic,⁴⁻⁶ indicating that the t_{2g} states have been broadened into a partially filled π^* -band. However, LaCrO_3 ($t_{2g}^3 e_g^0$) is an insulator and antiferromagnetic below $T_N = 320^\circ\text{K}$, indicating localized t_{2g} states on the chromium ion. Goodenough³ has pointed out, however, that overlap between cation and anion wave functions for this material is probably still appreciable since the magnetic exchange parameter is similar to that for LaFeO_3 , in which superexchange via σ -orbitals might be expected to provide a much stronger interaction.

These considerations have led us to investigate the properties of V^{+3} in perovskite-type materials. This ion is intermediate in the series and it is not possible a priori to state whether its electrons will be localized or collective. Metallic SrFeO_3 ⁷ ($t_{2g}^4 e_g^0$) is an analog since $S = 1$; however, the formation of π^* -bands in this material is probably a consequence of the higher formal charge. According to Reuter and Wollnik,⁵ the rare-earth vanadites AVO_3 appear to be semiconductors with an activation energy for conduction of about 0.20 eV for each member of the series. However, subsequent magnetic susceptibility measurements at low temperatures indicated Pauli paramagnetism.⁶ Since resistivity measurements had been made only on polycrystalline materials, it seemed desirable to repeat these measurements on single crystals and

Section III

to extend the magnetic susceptibility measurements over a larger temperature range. For this study, LaVO_3 and YVO_3 were selected as representative members of the series.

Single crystals of LaVO_3 and YVO_3 were obtained from their melts in iridium crucibles by cooling through the melting point at $5^\circ\text{C}/\text{hour}$ under an atmosphere of 85 percent argon-15 percent hydrogen. Melting points as measured by an optical pyrometer appeared to be about 2080° and 1860°C for LaVO_3 and YVO_3 , respectively. Chemical analysis for total vanadium and for vanadium oxidation states showed that only trivalent vanadium was present in both samples within analytical error; however, the YVO_3 sample contained about 1.5 percent excess Y_2O_3 . X-ray powder patterns indicated that both samples were single-phase materials; it was not possible to determine whether the Y_2O_3 was present as a solid solution or as a separate phase below the limits of detection.

Four-probe conductivity measurements were performed over the temperature interval 120° to 670°K by using the van der Pauw⁸ technique. The results are shown in Fig. III-1. Although the activation energy for LaVO_3 at temperatures above 0°C is similar to that obtained from powders,⁵ the results are in general quite different from the powder data. For both samples, the temperature dependence of resistivity is indicative of semiconducting behavior. The activation energies for YVO_3 over the entire temperature range and for LaVO_3 in the interval 130° to 270°K are remarkably low for semiconducting oxides.

Magnetic susceptibility measurements are being made on powders obtained from the crystal ingots. Preliminary results indicate the existence of an antiferromagnetic transition in LaVO_3 at $T_N \approx 135^\circ\text{K}$. This result is consistent with the increase in resistivity observed near this

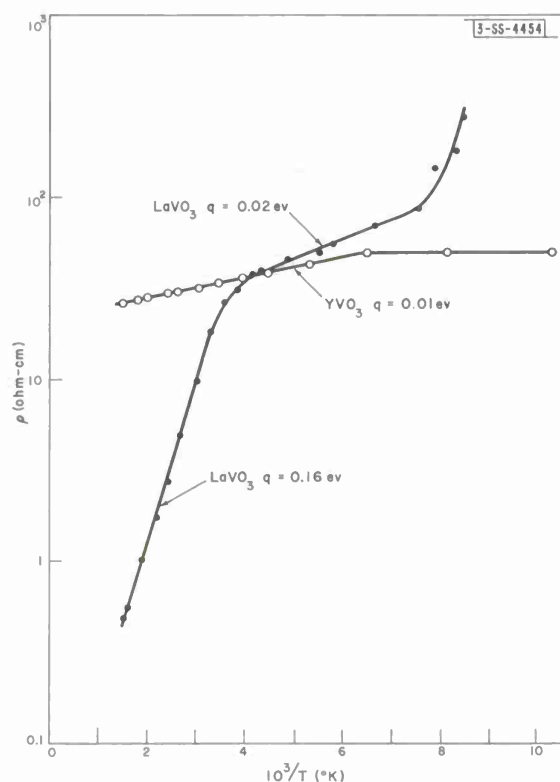


Fig. III-1. Temperature dependence of resistivity ρ for single crystals of LaVO_3 and YVO_3 . Values of activation energy q are derived from the slopes via the relation $\rho = \rho_0 \exp(q/kT)$.

temperature and with a crystallographic transition (probably cubic \rightarrow tetragonal, $c/a < 1$) which is observed for this material at about 126°K. The sign of the crystallographic transition and its occurrence below the magnetic ordering temperature suggest that the transition is probably due to spin-orbit coupling within the d^2 vanadium ion.

The magnetic results which are supported by the conductivity studies appear to indicate that the t_{2g} state of V^{+3} in rare-earth perovskites exists as discrete levels and that no bands are formed. However, the low activation energies may indicate that there is considerable mixing of cationic and anionic orbitals, with a mixing parameter λ near the critical value λ_c at which the localized-to-collective electron transition occurs.

D. B. Rogers	A. Ferretti
D. H. Ridgley	R. J. Arnott
R. W. Germann	E. J. Delaney

C. PEROVSKITE PHASE STABILITY IN La-Mn-O SYSTEM

Perovskite-type oxides of general formula $(La, M^{+2})(Mn^{+3}, Mn^{+4})O_3$ have been the subject of considerable investigation since Jonker and Van Santen⁹ first reported the occurrence of ferromagnetism in those compositions containing 10 to 50 percent of the total manganese as Mn^{+4} . These authors further showed that the amount of manganese in the tetravalent state depended sensitively on the conditions of sample preparation. Even when no substitution of divalent ions on the A-sites was attempted, $LaMnO_3$ exhibited a pronounced tendency to take up excess oxygen. Yakel¹⁰ reported that a sample containing 35.3 percent of the manganese as Mn^{+4} was of rhombohedral symmetry. Those containing less than 25 percent Mn^{+4} were orthorhombic or monoclinic. Subsequently, Wold and Arnott¹¹ described a preparation under pure nitrogen at 1300°C which resulted in only 0.02 percent Mn^{+4} . These authors found that the transformation from orthorhombic to rhombohedral symmetry at room temperature takes place at 21 percent Mn^{+4} . Goodenough, Wold, Arnott and Menyuk¹² have pointed out that perovskite systems containing manganese frequently exhibit two types of orthorhombic symmetry: an O'-orthorhombic symmetry ($c/\sqrt{2} < a \leq b$) in which the Mn^{+3} -occupied interstices have large distortions from cubic symmetry reflecting a Jahn-Teller ordering about the Mn^{+3} cation, and O-orthorhombic symmetry ($a < c/\sqrt{2} < b$) in which there is no static Jahn-Teller effect. They emphasize the importance of these symmetries for the application of superexchange theory to the observed magnetic properties and report a symmetry change in the system $LaMnO_{3+\lambda}$ from O' to O at $\lambda \approx 0.10$, or about 20 percent Mn^{+4} .

The presence of Mn^{+4} in perovskite phases having lanthanum to manganese ratios of 1:1 implies a formulation $La_{1-\delta}Mn_{1-7\delta}^{+3}Mn_{6\delta}^{+4}O_3$. For 35 percent Mn^{+4} , this corresponds to about 5.5 percent vacancies on both cation sites. Although numerous perovskite systems have been reported that have vacancies on the A-cation sublattice or the oxygen sublattice, B-site vacancies are quite unusual. Furthermore, large amounts of Mn^{+4} are surprising in view of the general instability of this valence state at elevated temperatures. Jonker and Van Santen⁹ suggested that the unusual stability of Mn^{+4} in this material might be indicative of a region of mixed crystals extending from $LaMn^{+3}O_3$ toward $La_{2/3}Mn^{+4}O_3$. In order to determine the limits of mixed crystal formation and the symmetries of the resulting structures, an investigation of perovskite phase stability in the system La-Mn-O has been initiated.

Section III

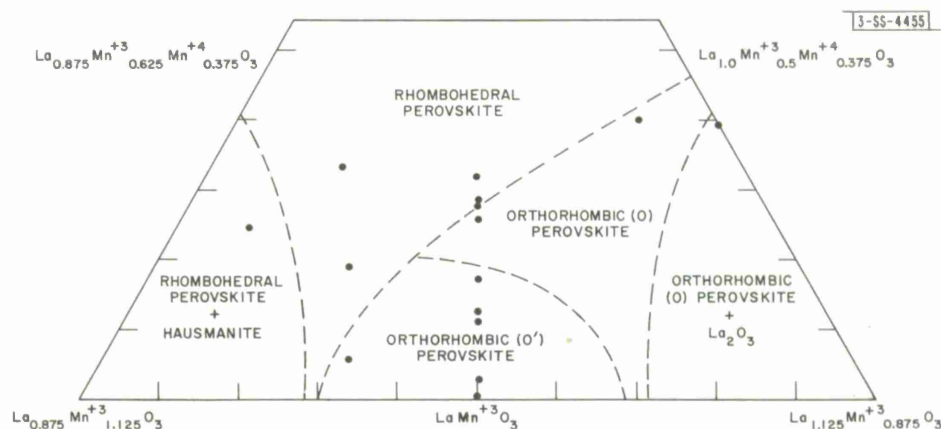


Fig. III-2. Tentative stability diagram of perovskite phases in the system La-Mn-O.

Samples were prepared by dissolving the desired amounts of La_2O_3 and Mn_2O_3 in nitric acid, evaporating the solutions to dryness under an infrared lamp, pre-firing at about 200°C to drive off volatile residues, thorough grinding of the residue in an agate mortar and pestle, then igniting under various atmospheres at temperatures ranging from 1000° to 1350°C . Samples heated in oxygen atmospheres and at lower temperatures yielded the largest $\text{Mn}^{+4}/\text{Mn}^{+3}$ ratios; samples heated in scrubbed nitrogen at about 1350°C yielded low $\text{Mn}^{+4}/\text{Mn}^{+3}$ ratios. The observed phases as determined by x-ray measurements are indicated on the stability diagram shown in Fig. III-2. Although the dashed boundary limits are only tentative and the diagram is incomplete, the large compositional ranges for the various perovskite phases are clearly established. From such a diagram it is obvious that the amount of tetravalent manganese in a given preparation will depend sensitively not only on atmosphere and temperature of ignition, but also on such variables as the degree of initial mixing of the component oxides, the length of ignition time, and especially on the lanthanum to manganese ratio. Thus, conflicting reports in the literature of sample composition and crystallographic symmetry for apparently similar preparations are not surprising.

D. B. Rogers
R. J. Arnott
E. J. Delaney

D. SEMICONDUCTOR \rightleftharpoons METAL TRANSITION IN LaCoO_3

Lanthanum cobaltate undergoes a semiconductor \rightleftharpoons metal transition^{13, 14} at 1210°K . Previous x-ray intensity analysis¹⁵ provided qualitative indications concerning this transformation. In order to obtain more precise information concerning the structural changes, the simplex method (see Sec. III-E) has been applied to new experimental data to refine the atomic parameters in the 500° to 1500°K range. The results follow.

1. Symmetry

Neutron diffraction measurements have shown that at room temperature this rhombohedral perovskite belongs to the space group $R\bar{3}c$.¹⁶ Refinement of high temperature x-ray data shows that the space group is $R\bar{3}$ and $R\bar{3}m$ in the semiconductor and metallic ranges, respectively.

Fig. III-3. Temperature dependence of lanthanum and oxygen atomic parameters in LaCoO_3 . Note difference in ordinate scales.

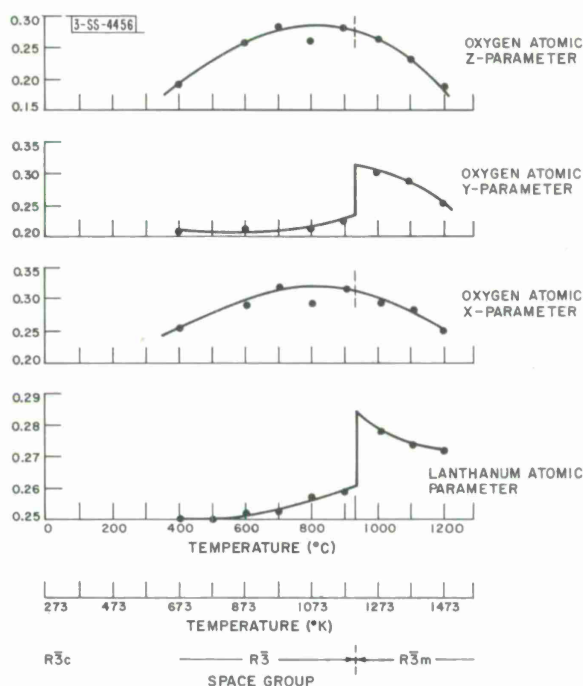


Figure III-3 shows the change in the lanthanum and oxygen atomic parameters in units of the pseudo-cubic cell edge. The values were computed on the basis of the $R\bar{3}$ and $R\bar{3}m$ space groups below and above 1210°K , respectively. Only in this manner was it possible to obtain consistent results across the transition point.

2. Structural Mechanism

Figure III-4 shows the variation with temperature of the oxygen-oxygen and lanthanum-cobalt distances specified in the $\{444\}$ planes and along the c -axis, respectively. From these results it follows that:

- With rising temperature, in the semiconducting phase, two lanthanum ions move in pairs along the c -axis toward a central cobalt ion (Fig. III-5). In the metallic phase, this motion is reversed with rising temperature, and the ions gradually return to their ideal position.
- The movement of the oxygen in both phases is such as to shield the cobalt from the lanthanum ions.

3. Interpretation

These data clarify the origin of the semiconducting \rightleftharpoons metallic transition at 1210°K and the change in the electrical activation energy with temperature in the interval $600^\circ\text{K} < T < 1210^\circ\text{K}$. They also demonstrate the surprising occurrence of increasing order with increasing temperature in this same interval. Analysis of magnetic susceptibility has shown that the high-spin Co^{3+} state is $\sim 5 \text{ cm}^{-1}$ above the low-spin Co^{III} state at 0°K . Although this energy separation increases by about $2 \text{ cm}^{-1}/^\circ\text{K}$, nevertheless, with increasing temperature, there is an increasing Co^{3+} population which approaches 50 percent at high temperatures. Since Co^{3+} has a larger

Section III

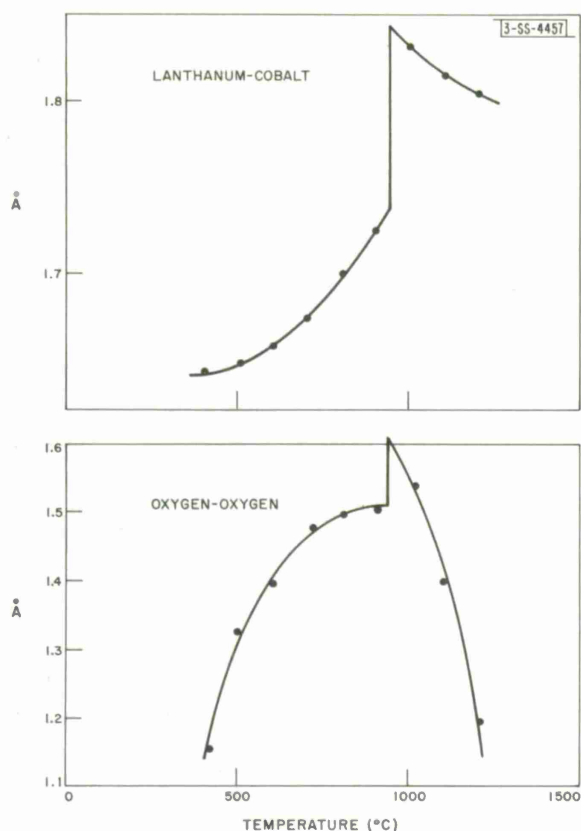


Fig. III-4. Temperature dependence of oxygen-oxygen and lanthanum-cobalt distances in LaCoO_3 . Note difference in ordinate scales.

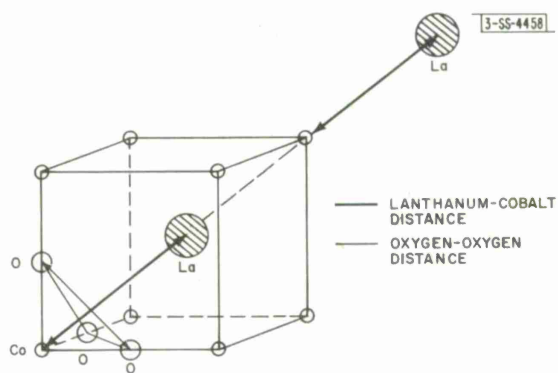


Fig. III-5. Motion of lanthanum ions in LaCoO_3 .

ionic size than Co^{III} in an octahedral site, ordering of Co^{3+} and Co^{III} ions takes place above $\sim 600^\circ\text{K}$, which is reflected in the oxygen x-parameter of Fig. III-3. Metallic conductivity occurs when the covalent mixing parameter for σ -bond orbitals is $\lambda > \lambda_c$, where λ_c is a critical value. Semiconducting and localized cationic e_g orbitals are present when $\lambda < \lambda_c$. In low-temperature LaCoO_3 , we have $\lambda < \lambda_c$. In high-temperature LaCoO_3 , the effective parameter to be used is

$$\bar{\lambda} = (\lambda_1 \lambda_2)^{1/2} = \lambda \{ 1 + 1/2(\gamma_1 - \gamma_2)/\lambda - \dots \}$$

where $\gamma_1 > \gamma_2$ because the wave functions fall off exponentially with distance from the atomic nuclei, and $\lambda_1 \equiv \lambda + \gamma_1$, $\lambda_2 \equiv \lambda - \gamma_2$, where λ_1 and λ_2 refer to the two cobalt sublattices that exist above 600°K . As $\bar{\lambda}$ increases with increasing temperature because of the increased distortion with increased ordering, $\bar{\lambda} \rightarrow \lambda_c$ at 1210°K .

P. M. Raccah
J. B. Goodenough

E. APPLICATION OF SIMPLEX METHOD TO CRYSTALLOGRAPHIC CALCULATIONS

The accuracy of precision cell edge calculations based on x-ray diffraction data can be markedly improved by nonlinear fitting on the observable function

$$2\theta = 2 \arcsin \left[\frac{\lambda}{2} f(h, k, l) \right]$$

in order to avoid any bias. When the nonlinear method is used, the systematic error in diffractometer readings is calculated and does not lead to inaccuracy in the cell edge results. The function to be minimized is still

$$F = \left[\frac{\sum_{i=1}^n \left| (2\theta)_{\text{calc}} - (2\theta)_{\text{obs}} \right|_i^2}{n} \right]^{1/2}$$

where $(2\theta)_{\text{calc}}$ and $(2\theta)_{\text{obs}}$ are the calculated and observed values of 2θ , respectively, and n is the number of peaks observed. A Fortran program employing the simplex method¹⁷ has been written for solving the minimization problem with the SDS 930 computer.

A second computer program, using essentially the same simplex routine for minimization, has been written for making atom position calculations based on diffractometer intensity data. In this case the function to be minimized is

$$F = \left[\frac{\sum_{i=1}^n \left| I_{\text{calc}} - I_{\text{obs}} \right|_i^2}{n} \right]^{1/2}$$

where I_{calc} and I_{obs} are the calculated and observed intensities, respectively, and n is the number of peaks. This method of calculation has made it possible to use ordinary powder diffractometer data successfully in order to study the high temperature transformation of LaCoO_3 (see Sec. III-D) and to determine the atom positions in a number of chromium spinels (see Sec. III-F).

P. M. Raccah
P. H. Trent

TABLE III-1
CRYSTALLOGRAPHIC PARAMETERS FOR CHROMIUM SPINELS

Compound	U-Parameter	Debye-Waller Factor	Cell Edge (Å)	Site Mixing	R-Factor
MnCr_2S_4	0.3863	0.18	10.11 ₀	0	0.057
FeCr_2S_4	0.3850	0.59	9.99 ₅	0	0.091
CoCr_2S_4	0.3821	0.35	9.92 ₃	0	0.020
CuCr_2S_4	0.3841	0.55	9.81 ₄	0	0.065
ZnCr_2S_4	0.3842	0.82	9.98 ₆	0	0.036
ZnCr_2O_4	0.3899	0.36	8.321	0.07*	0.036
ZnCr_2Se_4	0.3849	1.46	10.440	0	0.159
MnCr_2O_4	0.3890	~0	8.437	0	0.016
CdCr_2O_4	0.3896	0.33	8.596	0	0.018
CdCr_2Se_4	0.3894	1.25	10.740	0	0.075

*This apparent inversion is probably due to vacancies on the zinc site.

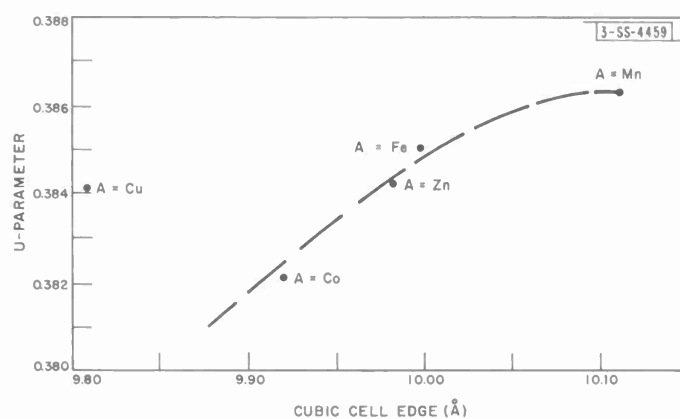


Fig. III-6. U-parameter vs cubic cell edge for chromium spinels of the type ACr_2S_4 .

F. CRYSTALLOGRAPHIC STUDY OF CHROMIUM SPINELS

Crystallographic parameters for 10 spinels of the type ACr_2X_4 (where A = Mn, Fe, Co, Cu, Zn, or Cd; and X = O, S, or Se) have been calculated from x-ray diffraction data on powdered samples. The U-parameter, Debye-Waller temperature coefficient, cubic cell edge, degree of site mixing, and R-factor for each compound are listed in Table III-1. For the five compounds containing sulfur, the U-parameter is plotted against cell edge in Fig. III-6. It is seen that $CuCr_2S_4$ does not belong to the same family as the other four compounds. This is not surprising since $CuCr_2S_4$ is metallic, whereas the other compounds are semiconductors.

The crystallographic parameters were calculated by the simplex method described in Sec. III-E from intensity data obtained with a Norelco diffractometer by using step-counting procedures. The precision of the fit between calculated and observed intensities is quite high, as indicated by the average R-factor of 0.059. A typical fit for $ZnCr_2O_4$ is given in Table III-2.

TABLE III-2
OBSERVED AND CALCULATED X-RAY INTENSITIES FOR $ZnCr_2O_4$

h	k	l	2 θ (deg)	Intensity	
				Observed	Calculated
2	2	0	30.65	11.6557	11.9943
3	1	1	36.00	31.3257	31.2489
2	2	2	37.60	1.8288	2.1829
4	0	0	43.70	4.5436	4.4438
4	2	2	54.16	4.4867	3.9597
5	1	1	57.70	12.5823	11.9291
3	3	3			
4	4	0	63.32	12.7123	13.0114
6	2	0	71.86	1.5687	1.3701
5	3	3	71.88	3.0155	3.1038
6	2	2	75.92	1.1298	1.4940
4	4	4	79.88	0.5283	0.5086
7	1	1	82.84	0.1788	0.1877
5	5	1			
6	4	2	87.78	1.8288	1.9330
7	3	1	90.72	4.6980	4.8444
5	5	3			
8	0	0	95.62	1.7801	1.6967
8	2	2	103.52	1.0567	1.0696
6	6	0			
7	5	1	106.58	3.4626	3.3866
4	4	4			
6	6	2	107.62	0.7966	0.8860

TABLE III-3
U-PARAMETERS OF CHROMIUM SPINELS

Compound	U-Parameter	
	By X-ray Diffraction	By Neutron Diffraction
MnCr_2S_4	0.3863	0.3876 [*]
FeCr_2S_4	0.3848	0.3840 [†]
CoCr_2S_4	0.3829	0.3830 [‡]
ZnCr_2Se_4	0.3849	0.3843 [§]
MnCr_2O_4	0.3890	0.3892 [‡]
[*] N. Menyuk and K. Dwight, J. Appl. Phys. <u>36</u> , 1088 (1965). [†] G. Shirane, D.E. Cox and S.Y. Pickart, J. Appl. Phys. <u>35</u> , 954 (1964). [‡] K. Dwight and N. Menyuk (unpublished). [§] R. Plumier, Compt. rend. <u>260</u> , 3348 (1965).		

In order to check the accuracy of the present method, the U-parameters obtained have been compared, when possible, with those found by neutron diffraction measurements. As shown in Table III-3, the differences in U-parameter are essentially in the fourth decimal place. This degree of agreement indicates that, with adequate calculational methods, standard x-ray powder measurements can yield structural data comparable in accuracy to those obtained from neutron diffraction experiments.

P. M. Raccach
R. J. Bouchard^{*}
A. Wold^{*}

G. PARTIAL PRESSURES FROM OPTICAL DENSITY MEASUREMENTS OF VAPOR PHASE

In order to obtain calibration data required for using density measurements to determine the selenium partial pressures over HgSe(c) and other binary selenides, the optical properties of selenium vapor in equilibrium with pure liquid selenium have been investigated. The optical density D_λ has been measured between 1900\AA and $2.0\text{ }\mu$ at optical cell temperatures of 330° , 400° , 500° , 700° , and 860°C for total selenium pressures between 7×10^{-5} and 1.0 atm . Previously identified¹⁸ vibronic bands of $\text{Se}_2(\text{g})$ that have a maximum D_λ near 3400\AA were observed as well as structureless (with $2\text{-}\text{\AA}$ resolution) absorption between 2000 and 2700\AA associated with the presence of one or more species of the type $\text{Se}_n(\text{g})$ with $n > 2$.

^{*} Brown University.

A self-consistent analysis of the data shows that the partial pressure p_2 of $\text{Se}_2(\text{g})$ is related to the measured optical densities by the expression $p_2 = r(D_{3405} - 0.18 D_{2400})/L$. The parameter r is a Beer's law constant for $\text{Se}_2(\text{g})$ which depends on the optical cell temperature, and L is the optical pathlength. The second term in the parenthesis is the contribution to D_{3405} of absorption by $\text{Se}_n(\text{g})$. Values of r were obtained by measuring D_{3405} for reservoir temperatures low enough for the vapor to consist entirely of $\text{Se}_2(\text{g})$. In such cases, $r = Lp_{\text{total}}/D_{3405}$, where p_{total} is the published^{19, 20} total pressure at the reservoir temperature. The measured values of r decrease from 0.236 atm-mm at 860°C to 0.141 atm-mm at 500°C. The temperature dependence of r is consistent with the known¹⁸ vibrational energy levels in the electronic ground state of $\text{Se}_2(\text{g})$ and with the assignment of the 3405-Å peak to a transition from the $v = 0$ vibrational state.

The p_2 values obtained from the experimental data agree closely with those calculated from the dissociation constants for Se_4 , Se_6 , and Se_8 given by Illarionov and Lapina.²⁰ However, particularly for nearly saturated vapor, they differ significantly from the p_2 values calculated from the Se_6 - Se_2 dissociation constant given by Stull and Sinke.²¹

R. F. Brebrick

H. RESISTIVITY AND HALL COEFFICIENT OF Ti_2O_3

The resistivity ρ and Hall coefficient R of Ti_2O_3 samples have been measured at the National Magnet Laboratory as a function of magnetic field H in the range $8 < H < 170$ kG. Specimens were cut in different orientations from single-crystal boules of Ti_2O_3 grown by the Czochralski method.²² The total content of altermvalent cationic impurities did not exceed 100 ppm relative to Ti^{+3} . The principal anionic impurity was N which was present in amounts exceeding 1.0 atom-percent relative to Ti; this corresponds to approximately 10^{20} excess holes per cm^3 if all N atoms were singly ionized.

Tables III-4 and III-5 summarize the experimental results. Repeated measurements of the same sample on different days with different equipment, or of samples cut in the same orientation from different locations in the same boule, gave results which differed by no more than 10 percent.

The following features of the data are noteworthy: (1) Neither reannealing at 800°C for three days nor etching had any significant effect on the results. (2) All samples are nearly isotropic; neither ρ nor R changes appreciably with sample orientation. (3) Both ρ and R diminish perceptibly, although not markedly, with rising temperature T in the range $4 < T < 390^\circ\text{K}$. (4) R is positive and is independent of magnetic field in the range $8 < H < 170$ kG. (5) For $T \geq 77^\circ\text{K}$, the magnetoresistance $\Delta\rho/\rho_0 \equiv [\rho(H) - \rho_0]/\rho_0$ is of the order of 10^{-4} . At 4.2°K, $\Delta\rho/\rho_0$ increases as H^2 for low H and as H for the intermediate and high magnetic field range. At this temperature, values of $\Delta\rho/\rho_0$ up to 0.12 – without any indication of saturation – were encountered.

The magnetoresistance observed at 4.2°K is too large to be reconciled with the charge carrier concentrations in the range 3 to $5 \times 10^{20} \text{ cm}^{-3}$ computed from the data on the basis of the one-band formula $R = 1/ne$. The lack of anisotropy is inconsistent with a band model²³ which ascribes band formation near the Fermi level exclusively to direct cation-cation interactions, since this model predicts that $\rho(\parallel c) \ll \rho(\parallel a)$.

J. M. Honig
R. T. Germain
D. M. Esterling

Section III

TABLE III-4
RESISTIVITY OF Ti_2O_3

Sample	O/Ti Ratio	Direction of Current Flow	Resistivity (ohm-cm) at				Remarks
			4.2°K	77°K	273°K	338°–390°K	
329	1.497	a	8.3×10^{-3}		2.4×10^{-3}		
			1.2×10^{-2}	6.9×10^{-3}	7.0×10^{-3}		*
41	1.504	a	5.0×10^{-3}	3.5×10^{-3}			
45		a	3.7×10^{-3}				
		a	1.2×10^{-3}			2.9×10^{-3}	*
		22° from c to a	5.5×10^{-3}	3.9×10^{-3}	2.2×10^{-3}	1.6×10^{-3}	
		45° from c to a	6.6×10^{-3}	4.6×10^{-3}	2.5×10^{-3}	1.7×10^{-3}	
47		c	1.7×10^{-2}	1.1×10^{-2}			†
		a	1.1×10^{-2}				
		a	1.6×10^{-2}	1.1×10^{-2}			†
		22° from c to a	8.2×10^{-3}				
		45° from c to a	7.4×10^{-3}	4.7×10^{-3}			
413	1.498	c	3.7×10^{-2}				
		a	1.3×10^{-2}	7.4×10^{-3}	3.7×10^{-3}	2.9×10^{-3}	
		22° from c to a	1.7×10^{-2}	9.0×10^{-3}	5.2×10^{-3}		
		45° from c to a	4.1×10^{-2}	2.2×10^{-2}	1.1×10^{-2}	9.0×10^{-3}	
*Sample etched.							
†Sample reannealed three days at 800°C.							

TABLE III-5
HALL COEFFICIENT OF Ti_2O_3

Sample	Direction of Current Flow	Hall Coefficient ($cm^3/coul$) at				Remarks
		4.2°K	77°K	273°K	338° – 390°K	
329	a	0.021	0.017	0.015		
	a	0.025	0.023	0.020		*
41	c	0.010				
	a	0.011	0.0090			
45	c	0.016				
	a	0.015		0.011		
	a	0.015	0.013	0.011	0.0096	*
	22° away from c to a	0.019	0.018	0.015	0.012	
47	45° away from c to a	0.019	0.016	0.013	0.012	
	c	0.017				
	c	0.010	0.010	0.0053		†
	c	0.017				
413	a	0.015	0.016	0.010		†
	22° away from c to a	0.023	0.018			
	45° away from c to a	0.020	0.018			
	c	0.016				
413	a	0.020	0.018	0.015	0.011	
	22° away from c to a	0.019	0.012	0.0075		
	45° away from c to a	0.021	0.019	0.014	0.011	
* Sample etched.						
† Samples reannealed three days at 800°C.						

I. SUPERCONDUCTIVITY AND RESISTIVITY IN HIGH PRESSURE InSb-In SYSTEM

The high pressure phase of indium antimonide, InSb(II), closely resembles β -Sn in structure,²⁴⁻²⁶ electrical properties,²⁵ and superconductivity.²⁷ The similarity between InSb(II) and β -Sn is also demonstrated by the fact that they form a complete series of solid solutions.²⁸⁻³⁰ This similarity is being explored still further by studying the InSb(II)-In system in order to compare its properties with those of the well-characterized Sn-In system.³¹

Samples of nominal composition $\text{InSb(II)}_{1-x}(\text{2In})_x$, with x between 0.1 and 0.5, have been prepared at 37 kbar. These samples were melted for two to three hours at 400°C (above the melting points of both InSb and indium at this pressure), quenched to room temperature, and annealed at 125°C for 20 hours. This annealing temperature was selected because there is a tin-rich hexagonal γ -phase in the Sn-In system whose composition stability range is widest at about 125°C. The samples were then cooled to about 150°K with liquid nitrogen before releasing the pressure in order to retain the high pressure phase(s) at atmospheric pressure. Discs with metallic lustre, about 5 mm in diameter and 3.5 mm thick, were obtained by this procedure and stored in liquid nitrogen to prevent transformation to the stable form.

All samples investigated are superconductors with transition temperatures T_c within the range $4.8^\circ \pm 0.2^\circ\text{K}$, in comparison with T_c values of 2.1° and 3.4°K for InSb(II) and indium, respectively. Increases in T_c with alloying are also observed in the InSb(II)-Sn (Ref. 28) and Sn-In (Ref. 31) systems. Distinct transitions at 4.71° and 4.96°K occurred for the sample with $x = 0.3$, presumably because of the presence of two superconducting phases. Since the mutual solubilities of tin and indium are quite limited, the existence of a two-phase region in the InSb(II)-In system would not be surprising. The existence of such a region is also suggested by the fact that T_c is essentially constant over a wide range of composition, since T_c might be expected to change with composition within a single-phase region. (It should not be concluded that the samples which exhibited only one superconducting transition are single phase, since the experimental conditions during the runs on these samples might have been unsuitable for resolving two narrowly spaced transitions. Furthermore, in a two-phase sample the spatial distribution of the phases may be such that one transition masks the other.)

Evidence that InSb(II) and indium do not form a complete series of solid solutions is also provided by the observation of thermal effects during temperature drift runs performed on samples with x up to 0.5. In these experiments, resistivity ρ and sample temperature are monitored as the sample is slowly heated above 77°K. At some effective transformation temperature T_{eff} , the rate of transformation to the stable atmospheric pressure form increases rapidly to high values, and ρ also increases rapidly. For all samples so far investigated, T_{eff} is $201^\circ \pm 2^\circ\text{K}$, the same value as for pure InSb(II). In the InSb(II)-Sn system, on the other hand, T_{eff} increases monotonically with increasing tin content.

In the drift runs on pure InSb(II) and on a sample with $x = 0.10$, no change in the rate of temperature increase was detected at T_{eff} . For a sample with $x = 0.15$, there was a slight increase in the rate at T_{eff} . For all samples with x between 0.2 and 0.5, however, the sample temperature at T_{eff} increased very rapidly (in some cases to a value as high as 20°K above ambient temperature) and then rapidly decreased to ambient temperature. These observations show that the amount of heat liberated by transformation to the atmospheric pressure state is

much larger for x greater than 0.2 than for x of 0.15 or below. This discontinuity indicates that in the high pressure system, there is a phase boundary at x of about 0.1 which separates solid solutions of indium in InSb(II) from a phase significantly different in structure from InSb(II). The latter might be analogous to the γ -phase in the Sn-In system.

Attempts are being made to identify the phases in the InSb(II)-In system by x-ray diffractometer measurements on solid samples kept at about 150°K. The samples examined thus far are so highly strained that the patterns obtained are unsuitable for structural determinations.

M. D. Banus
Lynne B. Farrell
A. J. Strauss

J. QUENCHING OF Dy^{+2} FLUORESCENCE BY Y^{+2} IN $\text{CaF}_2:\text{Dy}^{+2}$ LASERS

Yttrium, a common impurity in CaF_2 , is reduced from the trivalent to the divalent state when $\text{CaF}_2:\text{Dy}^{+2}$ lasers are produced by exposing Dy^{+3} doped single crystals to ionizing radiation. The $\text{Y}^{+2}(4d^1)$ quenches the fluorescence of $\text{Dy}^{+2}(4f^{10})$ and therefore raises the threshold for laser action.

The energy levels^{32, 33} of Dy^{+2} and Y^{+2} in CaF_2 are shown in Fig. III-7. Optical pumping into the broad absorption bands of Dy^{+2} efficiently populates the $^5\text{I}_7$ level, producing an inversion between this level and a Stark split level of the $^5\text{I}_8$ ground state. $\text{Y}^{+2}(4d^1)$ is a dynamical Jahn-Teller ion. No fluorescence is observed from the e_g level at $17,000\text{ cm}^{-1}$ since the transition takes place by means of nonradiative interactions with the lattice.

In order to study the interaction of Y^{+2} and Dy^{+2} , single crystals of CaF_2 containing 0.2 mole % of Dy^{+3} but different concentrations of Y^{+3} were grown by the Bridgman method. Several crystals, grown from "pure" CaF_2 prepared by reducing high purity CaCO_3 in HF, contained only 5×10^{-4} mole % Y. Crystals grown from commercial fluorite contained 5×10^{-3} mole % Y.

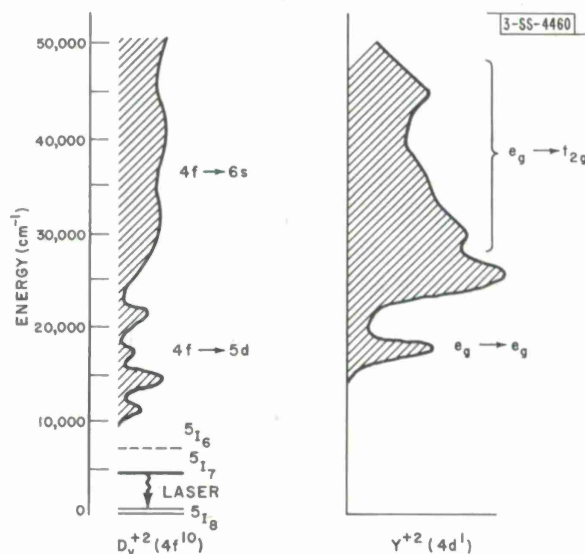


Fig. III-7. Energy levels of $\text{Dy}^{+2}(4f^{10})$ and $\text{Y}^{+2}(4d^1)$.

Section III

Other crystals were doped with various higher concentrations of YF_3 , up to a maximum of 12 mole %. These crystals were then polished into laser rods and irradiated with 10^6 rad of 2.5 mev electrons at room temperature. Subsequent optical absorption measurements showed that both dysprosium and yttrium were partially reduced to the divalent state. The exact divalent concentrations are not known. Previous experiments lead us to assume that the divalent ions represent about 10 percent of the initial trivalent ion concentrations.

The thresholds of the lasers, which were pumped with one FX-38A flash lamp, were measured at 87°K. Crystals grown from "pure" CaF_2 had an average threshold of 18.8 joules. (These lasers also operated as three-level systems at room temperature.) Material grown from commercial fluorite had an average threshold of 27.6 joules. The threshold of material intentionally doped with increasing amounts of YF_3 rose rapidly; doping with 1 mole % of YF_3 prevented laser action even for excitation energies exceeding 300 joules. From these data we conclude that Y^{+2} inhibits laser action in $\text{CaF}_2:\text{Dy}^{+2}$.

To investigate the mechanism inhibiting laser action, the fluorescent lifetime of the $^5\text{I}_7$ level of Dy^{+2} was measured as a function of yttrium concentration. If Y^{+2} and Dy^{+2} interact resonantly, the observed lifetime τ will be decreased from its intrinsic value τ_i by a quenching lifetime τ_q according to the reciprocal relation $1/\tau = 1/\tau_i + 1/\tau_q$. Lifetime measurements were made at 77°K. The fluorescent lifetime curves of the $^5\text{I}_7$ level are not exponential. The initial τ values, which depend on the Y concentration, varied from 12.2 msec for the purest sample (5×10^{-4} mole % Y) to 6.2 msec for crystals containing 12 mole % YF_3 . In all cases, τ increased to the same final value of 14 msec.

Figure III-8 is a plot of τ_q vs C^{-2} , where C is the total concentration of yttrium. Values of τ_q were computed using initial τ measurements and assuming $\tau_i \sim 14$ msec. The figure shows that τ_q is proportional to C^{-2} and therefore to r^6 , where r is the interionic distance. This

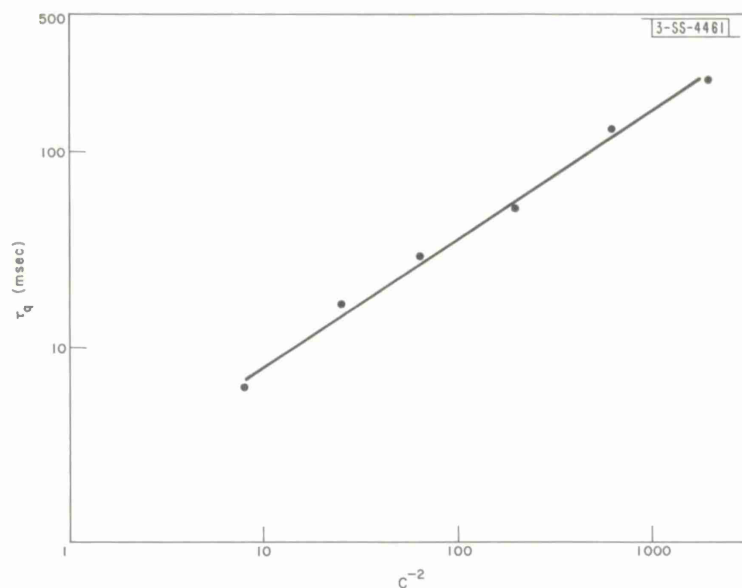


Fig. III-8. Quenching lifetime τ_q for Dy^{+2} in CaF_2 vs C^{-2} , where C is the total concentration of Y^{+3} in mole percent.

indicates that dysprosium and yttrium interact by means of dipolar fields and that the energy exchange is resonant.

The energy level diagrams, as well as the nonexponential lifetime curves, imply that the energy exchange takes place between the 5I_7 level of Dy^{+2} and excited t_{2g} levels of Y^{+2} . Energy in these levels is short-circuited to the Y^{+2} ground state. In order to substantiate this view, lifetime measurements were made by using filtered radiation. The filter absorbed photons of energy greater than $20,000\text{ cm}^{-1}$ and prevented population of the t_{2g} levels of Y^{+2} . Under these conditions, lifetime curves are exponential and no quenching effects were observed.

The resonant energy transfer between Dy^{+2} and Y^{+2} involves the transfer of a "virtual" photon. Under constant illumination, we should also expect the fluorescent output of Dy^{+2} to be reduced by the absorption of "real" photons by the t_{2g} levels of Y^{+2} .

J. R. O'Connor

REFERENCES

1. J.B. Goodenough, Bull. Soc. Chim. France 4, 1200 (1965).
2. A. Ferretti, D.B. Rogers and J.B. Goodenough, J. Phys. Chem. Solids (to be published).
3. J.B. Goodenough, AIME Meeting, Philadelphia, Pennsylvania, 19 October 1964.
4. W.D. Johnston and D. Sestrich, J. Inorg. Nucl. Chem. 20, 32 (1961).
5. B. Reuter and M. Wollnik, Naturwissenschaften 17, 569 (1963).
6. S. Kern and D.B. Rogers (unpublished).
7. J.B. MacChesney, R.C. Sherwood and J.F. Potter, J. Appl. Phys. (to be published).
8. L.J. van der Pauw, Philips Res. Report 13, 1 (1958).
9. G.H. Jonker and J.H. Van Santen, Physica 16, 337 and 559 (1950).
10. H.L. Yakel, Acta Cryst. 8, 394 (1955).
11. A. Wold and R.J. Arnott, J. Phys. Chem. Solids 9, 176 (1959).
12. J.B. Goodenough, A. Wold, R.J. Arnott and N. Menyuk, Phys. Rev. 124, 373 (1961).
13. J.B. Goodenough and P.M. Raccach, J. Appl. Phys. 36, 1031 (1965).
14. Solid State Research Report, Lincoln Laboratory, M.I.T. (1965:1), Sec. III-D-3-b.
15. *Ibid.*, Sec. III-D-3-a.
16. *Ibid.*, Sec. IV-A-6.
17. J.A. Nelder and R. Mead, Computer J. 7, 308 (1965).
18. B. Rosen, Physica 6, 205 (1939).
19. L.S. Brooks, J. Am. Chem. Soc. 74, 227 (1952).
20. V.V. Illarionov and L.M. Lapina, Doklady Akad. Nauk S.S.S.R. 114, 1021 (1957).

Section III

21. D.R. Stull and G.C. Sinke, Thermodynamic Properties of the Elements (American Chemical Society, Washington, D.C., 1956), p. 179.
22. Solid State Research Report, Lincoln Laboratory, M.I.T. (1965:1), Sec. III-B-3.
23. Solid State Research Report, Lincoln Laboratory, M.I.T. (1964:2), p. 63, DDC 606126, H-606.
24. M.D. Banus, R.E. Hanneman, A.N. Mariano, E.P. Warekois, H.C. Gatos and J.A. Kafalas, Appl. Phys. Letters 2, 35 (1963).
25. R.E. Hanneman, M.D. Banus and H.C. Gatos, J. Phys. Chem. Solids 25, 293 (1964).
26. P.L. Smith and J.E. Martin, Nature 196, 762 (1962).
27. H.E. Bömmel, A.J. Darnell, W.F. Libby and B.R. Tittman, Science 139, 1301 (1963).
28. M.D. Banus, S.D. Vernon and H.C. Gatos, J. Appl. Phys. 36, 864 (1965).
29. M.D. Banus, A.J. Strauss and L.B. Farrell, J. Appl. Phys. 36, 2186 (1965).
30. A.J. Darnell and W.F. Libby, Phys. Rev. 135, A1453 (1964).
31. M.F. Merriam and M. von Herzen, Phys. Rev. 131, 637 (1961).
32. J.R. O'Connor and J.H. Chen, Phys. Rev. 130, 1790 (1963).
33. Z.J. Kiss and R.C. Duncan, Proc. IRE 50, 1531 (1962).

IV. PHYSICS OF SOLIDS

A. MAGNETO-OPTICS

1. Reflectivity of ReO_3

Preliminary measurements of the reflectivity of small ReO_3 crystals by G.B. Wright showed that a plasma reflection edge in the green accounts for the bright red appearance of these crystals. The crystals were grown in our laboratory, and resistivity measurements have shown the material to be metallic with high conductivity.* The optical measurements have now been carried out with a spectrometer designed to measure absolute reflectivity of samples with surface areas as small as 1 mm^2 . The results of the measurements taken to date at room temperature are shown in Fig. IV-1.

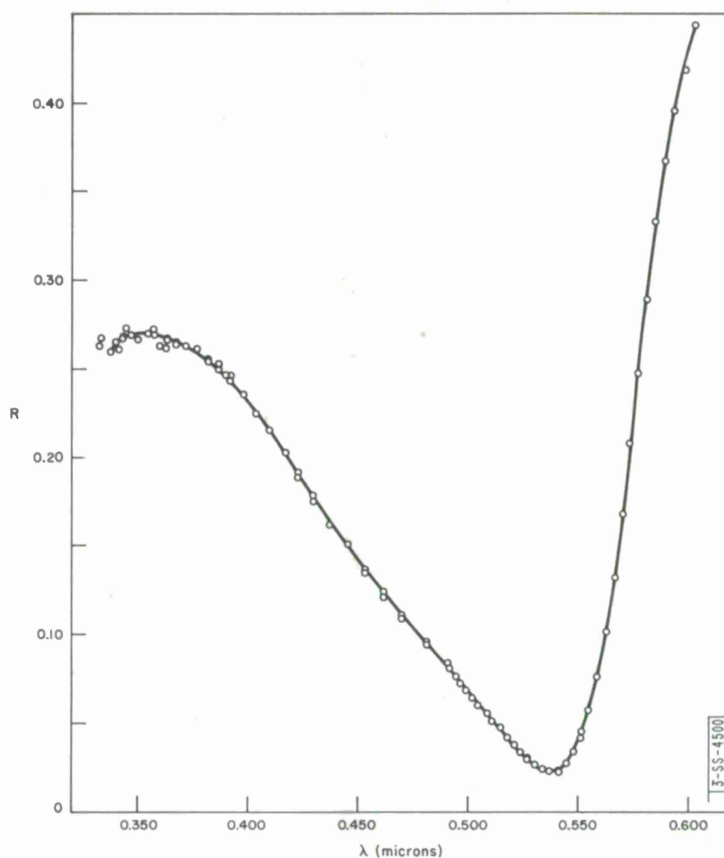


Fig. IV-1. Reflectivity near plasma edge of ReO_3 at 300°K.

* See p. 59 of Ref. 1.

Section IV

In the long wavelength region, at 2.5μ , a reflectivity of about 91 percent was measured at several points on the small, 2 to 3 mm², grown surface of the best crystal. Care was taken to ensure that light was reflected at near normal incidence from a single crystal face without overlapping small angle grain boundaries. Photomultiplier and PbS detectors were used to record the spectra with the CaF₂ prism monochromator.

The plasma edge occurs as a sharp drop in reflectivity to a minimum of 1.9 percent at a photon energy of 2.30 eV. The reflectivity recovers smoothly to a value of 28 percent at the highest energy at which measurements were made (3.8 eV). The steepness of the plasma edge (~ 0.2 eV) and the depth of the minimum appear to be similar to that observed in silver near 3.85 eV. Thus it is not clear whether the edge is caused only by free carrier plasma effects, or whether there is also an interband process. Our extension of these measurements to a greater energy range and an analysis of the optical constants should elucidate the mechanism for the plasma edge and its connection to the band structure of this material.

J. Feinleib
A. L. McWhorter
B. Feldman

2. Oscillatory Faraday Rotation and Magnetoabsorption of the Indirect Transition in Germanium*

The observations last reported in preliminary form[†] on the oscillatory Faraday rotation of the indirect transition in germanium have been extended to magnetic fields of 103 kG and down to temperatures of 1.5°K. In addition to the (110) orientation for which heat sunk measurements were previously reported, measurements were carried out on the (100) orientation. Far less structure was observed for the case of the radiation perpendicular to the (100) face than for the case of the radiation perpendicular to the (110) face, since the former configuration exhibits only a single electronic effective mass, whereas the latter exhibits two. This is consistent with the previous determination by Halpern and Lax,² from magnetoabsorption data, that the main transitions in the indirect spectrum are those from the top of the valence bands to the electronic ladders in the conduction band.

A representative summary of a typical set of rotation data [for \vec{H} parallel to a (110) face] together with the corresponding magnetoabsorption is shown in Fig. IV-2. The absorption data, consisting of the upper left and lower right traces, have been placed on the figure to indicate the locations of the transitions; since these curves just give the relative transmission, they have been placed as shown for convenience. The lower right trace represents the exciton absorption, while the upper left trace gives the transmission at energies in the region of the Landau levels. It can be seen that the rotation data contain a great deal more structure than the absorption data.

It should be noted that the simple Landau level theory for the magnetoabsorption of the indirect transition is not obeyed in germanium at magnetic fields of $\gtrsim 60$ kG. The simple theory predicts a staircase-like behavior and this is in fact observed at lower fields; however, the high

* This experiment was carried out using the high field facilities of the National Magnet Laboratory, M.I.T.

† See p. 40 of Ref. 1.

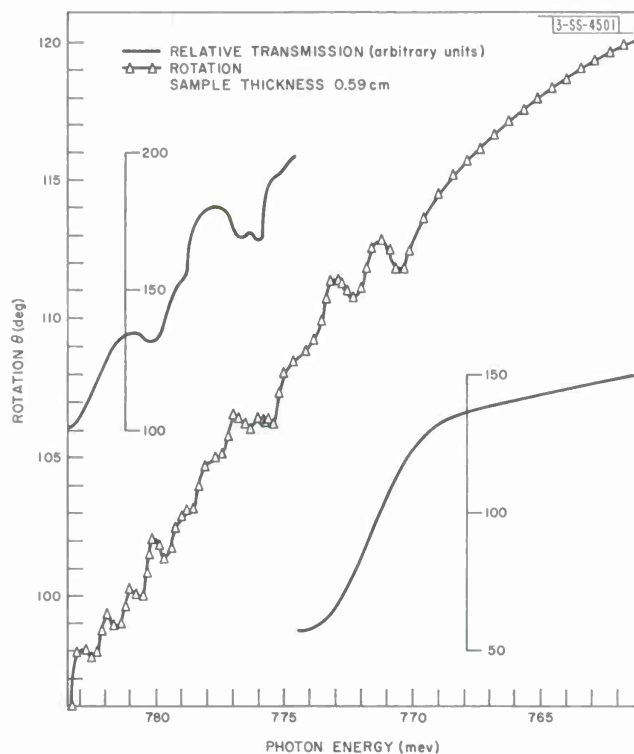


Fig. IV-2. Oscillatory Faraday rotation and transmission of indirect transition in germanium at 1.5°K for (110) orientation with $H = 103$ kG.

field (103 kG) data shown in the figure clearly contain oscillatory components. A possible explanation for the deviation from the simple theory at high fields is the increased contribution of exciton transitions.

In order to carry out a line-shape analysis of the oscillatory rotation due to the indirect transition, it is necessary to subtract out the background rotation which represents the dispersive tail of the direct energy gap transition. This has been carried out for the (100) orientation in indirect exciton for several magnetic field values; the results are shown in Fig. IV-3. By using phenomenological relaxation times $\sim 5 \times 10^{-11}$ seconds, we have been able to fit the line shapes shown, with dispersion curves centered at the energies corresponding quite closely to the two points at which the experimental curve for a given field crosses the axis. The energy difference between the two points represents the separation between the strongest lines of each of the two components of the exciton. This energy, as a function of the magnetic fields in question, is approximately constant and is equal to 1.5 mev. Up to 85 kG, the shift in energy with magnetic field of each of these two lines taken separately is linear and is equal to 0.04 mev/kG. Above 85 kG, it appears that the energy shift with magnetic field contains a quadratic term. These results can be compared with the magnetoabsorption Zeeman spectrum for the (100) orientation of the indirect exciton as shown in Fig. IV-4. These data were taken at an earlier date³ and extend out to only 73 kG; however, they do overlap with the lowest field values shown in Fig. IV-3. The strong lines labeled 1 and 2 in Fig. IV-4 correlate with the rotation data. The high field slopes of these lines are approximately equal and separated by 1.5 mev so that the energy spacing

Section IV

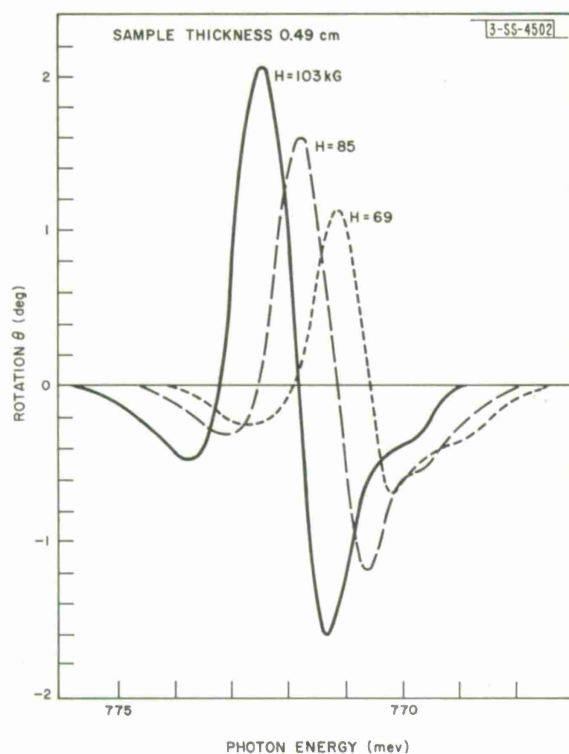
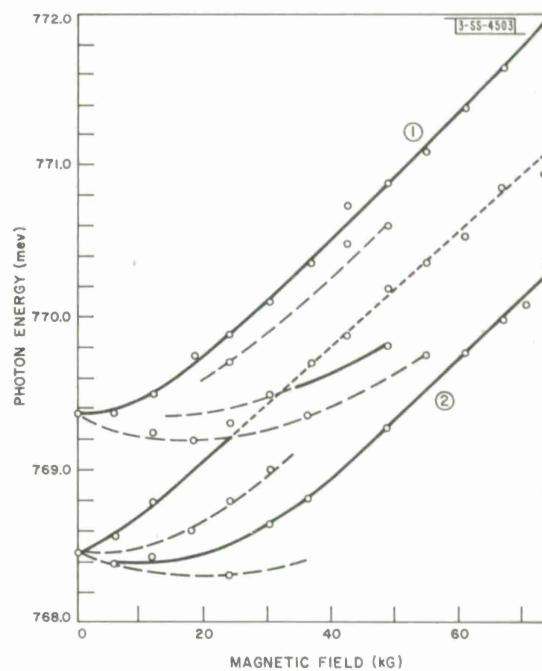


Fig. IV-3. Oscillatory part of Faraday rotation in vicinity of indirect exciton at $T = 1.5^\circ\text{K}$ for (100) orientation.

Fig. IV-4. Zeeman spectrum of indirect exciton in germanium at 1.7°K for (100) orientation.



is constant and of the magnitude observed in the rotation data. The energy shift with magnetic field for either component in the linear region is 0.04 meV/kG, also in agreement with the rotation data. We are presently engaged in extending the absorption measurements to fields of greater than 100 kG to ascertain whether the quadratic term observed in the rotation data is seen.

A comparison of the data obtained for the (110) orientation for both the heat sunk and the helium immersed cases indicates that the strain splitting (which exists only in the heat sunk case, where the sample is wedged into a holder for good thermal contact) is of opposite sign to the magnetic field induced splitting. This behavior is being investigated further.

J. Halpern

3. Oscillatory Faraday Rotation of the Direct Transition in GaSb*

We have observed the Faraday rotation of the direct transition in thin single-crystal GaSb samples having $\sim 10^{17}$ impurities/cm³. The experiments were carried out both in the low magnetic field regime and at fields of up to 103 kG for a range of energies from below the gap to approximately 100 meV into the edge. The low field ($\lesssim 40$ kG) rotation experimental results are shown in Fig. IV-5. The data were taken for an 8- μ -thick sample mounted on a glass substrate which was immersed in a helium bath and held at 1.5°K. The rotation was measured on transmission with the direction of propagation (and the magnetic field) perpendicular to a (110) face.

The rotation in the vicinity of 810 meV is due to direct transitions to the lowest lying exciton level. The spectra at higher energies are due to direct transitions between complementary Landau levels. We do not believe that these relatively low magnetic field transitions are excitonic in nature because (as shown in Sec. IV-A-4 which discusses magnetoabsorption data) the positions of these transitions extrapolate in the limit of zero field to an edge energy which lies 5 meV above the position of the zero field exciton. Furthermore, the relative amplitudes of corresponding peaks exhibit an approximately H^2 behavior. This is in good agreement with the relative amplitudes expected on the basis of a Landau level model, assuming that the relaxation time τ is relatively independent of H for small magnetic fields. Such a model gives an H^2 dependence of amplitude for small fields which goes over into a linear dependence at higher fields. The variation of line shape with magnetic field for the transition in the energy range 825 to 830 meV is particularly clear and seems to be amenable to analysis in terms of the theoretical curves developed by Halpern, Lax and Nishina;⁴ the relevant calculations are presently being carried out.

The high field rotation data are shown in Fig. IV-6. The absorption becomes so large in the vicinity of the exciton and first Landau transition (for the samples we had) that it becomes difficult to determine the rotation. In the other energy regions it is seen that the rotation saturates strongly. Here, the simple Landau level theory breaks down because the best one could hope for in using this theory would be a linear dependence of the amplitude on H at high magnetic fields. There are two alternative models that could possibly describe this type of saturation. One would

* This experiment was carried out using the high field facilities of the National Magnet Laboratory, M.I.T.

Section IV

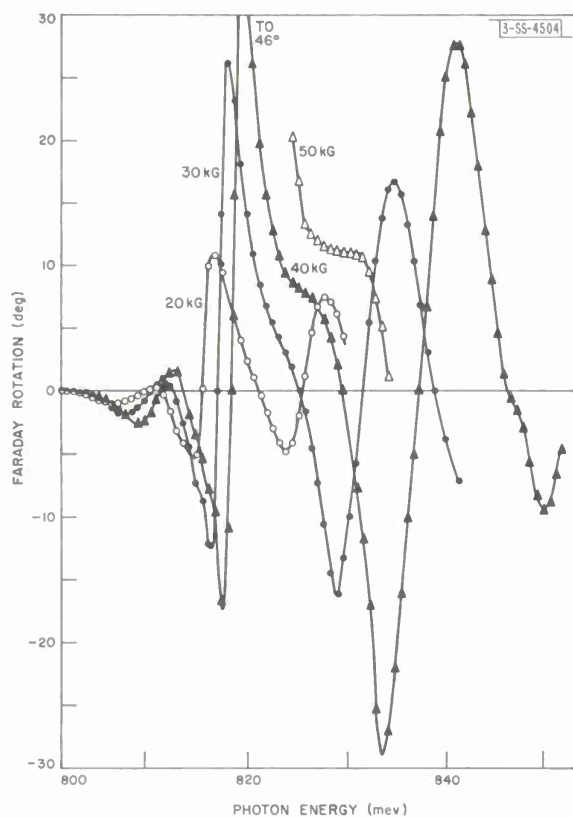


Fig. IV-5. Low field oscillatory rotation of direct transition in GaSb at 1.5°K.

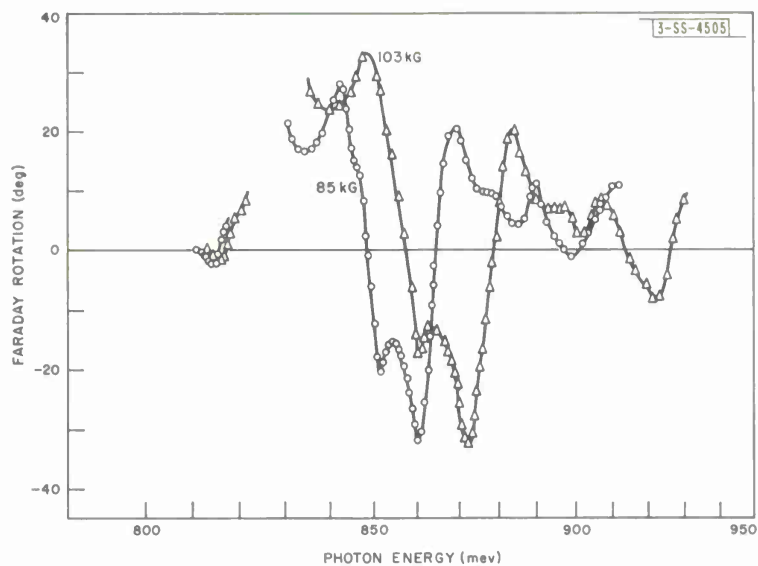


Fig. IV-6. High field Faraday rotation of direct transition in GaSb at 1.5°K.

require a magnetic field dependence of the relaxation time τ for high fields which goes approximately as $\tau \propto H^{-3/2}$; in the quantum limit at 4.5°K where $\hbar\omega_c \gg kT$, this is not an unreasonable dependence. The other possible explanation is that at high magnetic fields the transitions to the exciton levels lying beneath each of the Landau levels are much more likely than transitions to the Landau levels themselves. Elliott and Loudon⁵ have shown that the rotation connected with such exciton transitions will exhibit saturation. Because of the curvature of the conduction band, it is unfortunately not possible to determine from the magnetoabsorption data whether the high field transitions are indeed to exciton levels.

In Fig. IV-7 we have plotted the positions of the peaks of the Faraday rotation as a function of magnetic field for both the low and high field data; such a plot enables us to identify families of transitions. The lower three lines represent the exciton rotation peaks; these do not converge to a common zero field value. This is attributed to the zero field strain splitting of the exciton. The upper six lines in the figure converge to a zero field edge value which is in agreement with that determined from magnetoabsorption data. One should note that the energies which the positions of the peaks represent do not coincide with the Landau transition energies; however, both sets of energies converge to the same zero field limit. It seems fortuitous that the positions of the high field peaks appear to lie on straight lines in spite of the nonparabolic behavior of the conduction band at high fields; again, this is probably connected with the fact that the energies at which the peaks fall do not represent the transition energies.

J. Halpern

4. Magnetoabsorption of Circularly Polarized Light in GaSb*

As an aid in the interpretation of the Faraday rotation data for the direct transition in GaSb (discussed in Sec. IV-A-3), we have carried out magnetoabsorption experiments in the Faraday geometry for both right and left circularly polarized (RCP and LCP) light. In Fig. IV-8 we show a plot of the positions of the direct transitions for $E \perp H$ as a function of magnetic field. The solid and open points are for LCP and RCP light, respectively; the squares represent strong transitions and the triangles weak ones. The crosses represent the data taken by Zwerdling, *et al.*,⁶ at 39 kG in the Voigt geometry with $E \perp H$; such a configuration will simultaneously exhibit both RCP and LCP transitions. The discrepancy at the lowest levels could possibly be explained in two ways. It is either due to the different conditions of strain in the two experiments or to the anisotropy of the valence bands (our data were for $H \parallel [110]$, while those of Zwerdling, *et al.*, were for $H \parallel [111]$).

We are presently engaged in the identification of the individual transitions; this is somewhat complicated for the low quantum numbers because of the above-mentioned strained sample situation (the samples are mounted on glass substrates and are helium immersed, giving rise to a differential contraction).

However, from the high quantum number, low magnetic field spacings for the LCP and RCP series, we have been able to determine the electron light-hole reduced mass as 0.022 m. If we

* This experiment was carried out using the high field facilities of the National Magnetic Laboratory, M.I.T.

Section IV

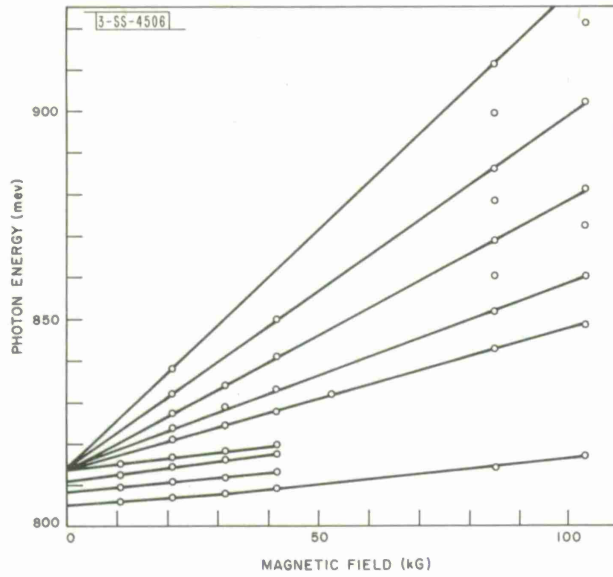
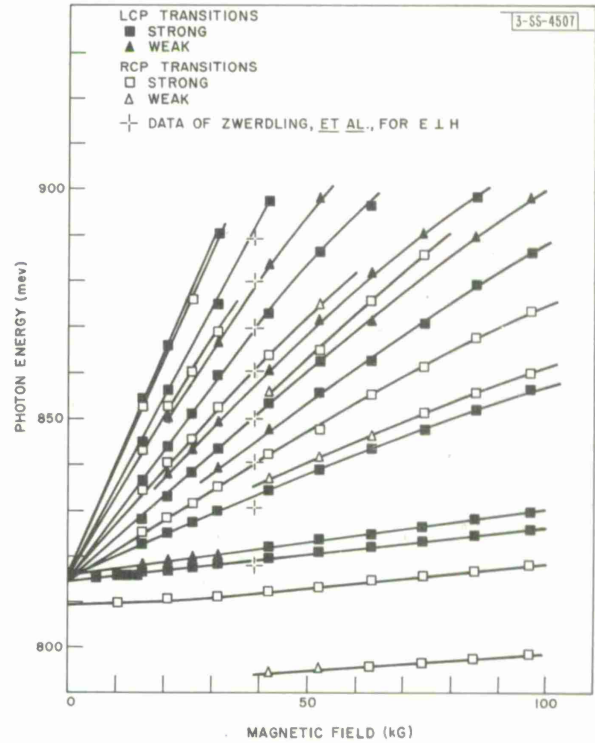


Fig. IV-7. Positions of peaks of Faraday rotation curves in GaSb plotted as a function of field at $T = 1.5^\circ\text{K}$ for (110) orientation.

Fig. IV-8. Positions of direct transitions in GaSb at 1.5°K for $E \perp H$ as a function of magnetic field.



use the previously determined experimental data for the electron heavy-hole reduced mass, the result that the split-off band energy at $\vec{k} = 0$ can be bracketed between the values 0.8 and 1.0 meV, and demand consistency within the framework of the Kane theory,⁷ we obtain values of 0.047 m for the light-hole mass and 0.041 m for the electron mass.

Several other results can be obtained from the data presented in Fig. IV-8. The nonparabolic high field behavior of the conduction band can be seen; this effect appears at magnetic fields greater than ~ 40 kG. Also, the two lines at the bottom of the figure correlate very well with those observed by Johnson, *et al.*,⁸ who denoted these the α - and γ -lines and interpreted them as an exciton and an exciton-impurity complex, respectively. The low field quadratic behavior for the α -line characteristic of an exciton is clear from the figure; the low field behavior of the γ -line could not be determined because the transition became too weak. Finally, a zero field energy gap of 814.5 ± 0.5 meV at 1.5°K is obtained together with an exciton binding energy of 5 meV; however, this latter number is not too significant because of the sample strain.

J. Halpern

5. Magnetoabsorption of the Direct Transition in GaSe*

We have initiated a program to investigate the band structure of GaSe by using the magneto-optical effects. This material is particularly suited to theoretical analysis in that it has a layer structure and can, for many types of experiments, be considered as a two dimensional structure.

As of this writing we have carried out some very preliminary observations on samples which we believe to be relatively unstrained and which range in thickness from 10 through 70μ — the thickness being chosen to match the absorption coefficient at the wavelength of interest. These experiments have been performed both at room temperature and with the samples immersed in liquid helium and held at 1.5°K . The magnetic field data has so far been taken in the Faraday geometry with the field perpendicular to the layers and at fields ranging from zero up to 96 kG.

No indication of magneto-oscillation was observed in the room temperature measurements. However, we did observe the broad absorption which occurs above the edge both at zero field and at 96 kG; this absorption had previously been seen only at lower temperatures.^{9,10} Also, the ratio of maximum to minimum in the absorption coefficient in the vicinity of the $n = 1$ exciton level (in the zero field data) is considerably greater than that reported by other experimenters.^{9,10} This would indicate that the material is of good quality; Hall effect measurements are presently being carried out to substantiate this. We have also observed a shift in the position of the room temperature $n = 1$ exciton peak of approximately 5 to 6 meV to lower energies, in a magnetic field of 96 kG. Such behavior could possibly be explained on the basis of a large g -factor together with a large effective mass. Furthermore, the peak exhibits a splitting of the same magnitude (5 meV) which would correspond to a g -factor of eight or so.

The data obtained at 1.5°K show large oscillatory magnetoabsorption effects. A typical set of experimental transmission traces for several values of magnetic field is shown in Fig. IV-9 (these have not been normalized to correct for variation of photomultiplier response with wavelength). The data shown are for unpolarized light. The line shapes are clearly characteristic

*This experiment was carried out using the high field facilities of the National Magnet Laboratory, M.I.T.

Section IV

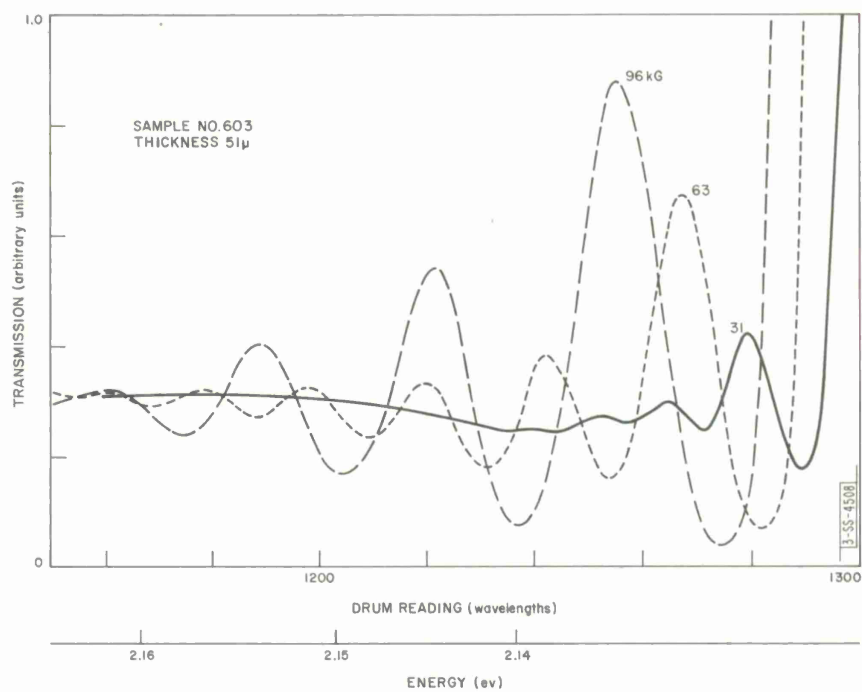


Fig. IV-9. Experimental traces of oscillatory magnetoabsorption of direct transition in GaSe at $T = 1.5^\circ\text{K}$ with $H \parallel C$.

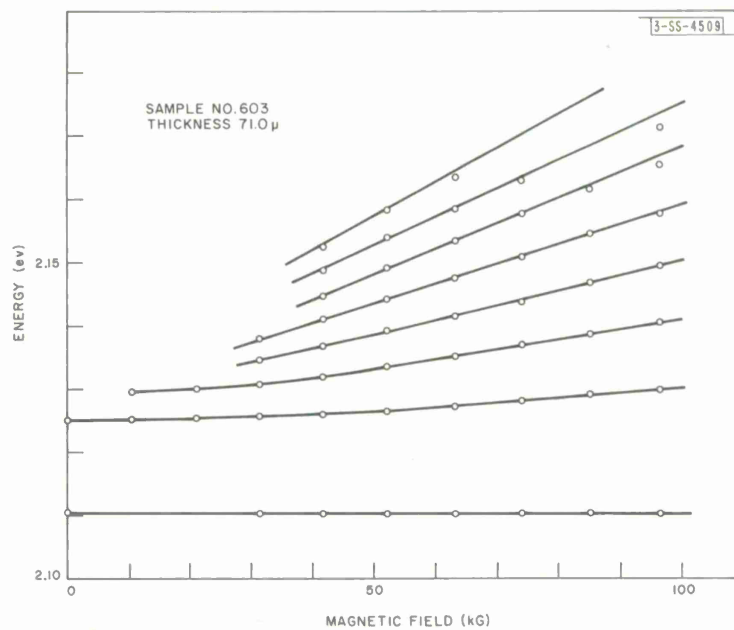


Fig. IV-10. Positions of direct transitions in GaSe as a function of magnetic field at $T = 1.5^\circ\text{K}$ with $H \parallel C$.

of direct transitions. Other data, taken with LCP and RCP light, respectively, give two series of lines with a small energy difference (~ 0.75 mev) between corresponding pairs of transitions. Such a spectrum would be obtained if one assumes, with Bassani, *et al.*,¹⁰ a simple nondegenerate band at both valence and conduction band edges (either at Γ or Z) composed of linear combinations of s and p_z orbitals, and a difference in g -factor between the respective bands, $g_2 - g_1 \approx 1.5$.

In Fig. IV-10 we have plotted the energies of the direct transitions as a function of magnetic field. Although the data are not complete it is clear that the transitions, at least for the lower quantum numbers, are to the exciton states lying beneath the Landau sub-bands rather than to the Landau levels themselves. From the figure, we estimate an edge energy of 2.13 ev and an exciton binding energy at 1.5°K of ~ 20 mev. One can observe an apparent deviation from parabolicity at the higher fields and quantum numbers and also an increase in the effective reduced mass with increasing magnetic quantum number.

J. Halpern

6. Optical Studies of Sulfur-Doped Silicon

A fourth impurity center due to sulfur in silicon, in addition to those previously reported,¹¹ presumably pairs of neutral sulfur atoms, has been found with an ionization energy of 0.1089 ev. Studies of the transitions from the ground state to the excited states under stress indicate that the value derived for the pure shear deformation potential E_2 by using this center is identical with that obtained for silicon by using other sulfur impurity centers. Measurements of the stress along $\langle 100 \rangle$ axes previously reported¹² have been complemented with measurements of the behavior of the transitions for stresses in other high symmetry crystal orientations. The data show unexpected extra splitting of the transitions with stresses along the $\langle 111 \rangle$ and $\langle 110 \rangle$ axes. Some of these additional splittings are apparently due to impurity centers with lower than tetrahedral symmetry.

W.E. Krag S. Fischler
W.H. Kleiner H.J. Zeiger

7. Determination of Spin-Orbit Band Splitting in Graphite*

Previous values of the spin-orbit band splitting in graphite have been derived by McClure and Yafet¹³ who used tight binding arguments and an analysis of the temperature dependence of the small g -shift observed in the electron spin resonance experiments of Wagoner.¹⁴ In this analysis it was found that the crystalline environment of graphite apparently reduced the atomic spin-orbit splitting of carbon¹⁵ by more than one order of magnitude. In fact, the tight binding estimates¹³ indicate a spin-orbit splitting of only $\sim 10^{-5}$ ev, whereas the g -shift analysis yields a value of $\sim 10^{-4}$ ev. By using the magnetoreflexion technique, a more direct measurement was made of the spin-orbit band splitting ϵ_{so} in graphite. The preliminary result of $\epsilon_{so} = 0.005 \pm 0.002$ ev which was obtained differs sharply from the previous indirect determination,¹³ but is comparable to the valence band splitting of diamond, $\epsilon_{so} = 0.006$ ev (Ref. 16). Experiments with

* This experiment was carried out using the high field facilities of the National Magnet Laboratory, M.I.T.

Section IV

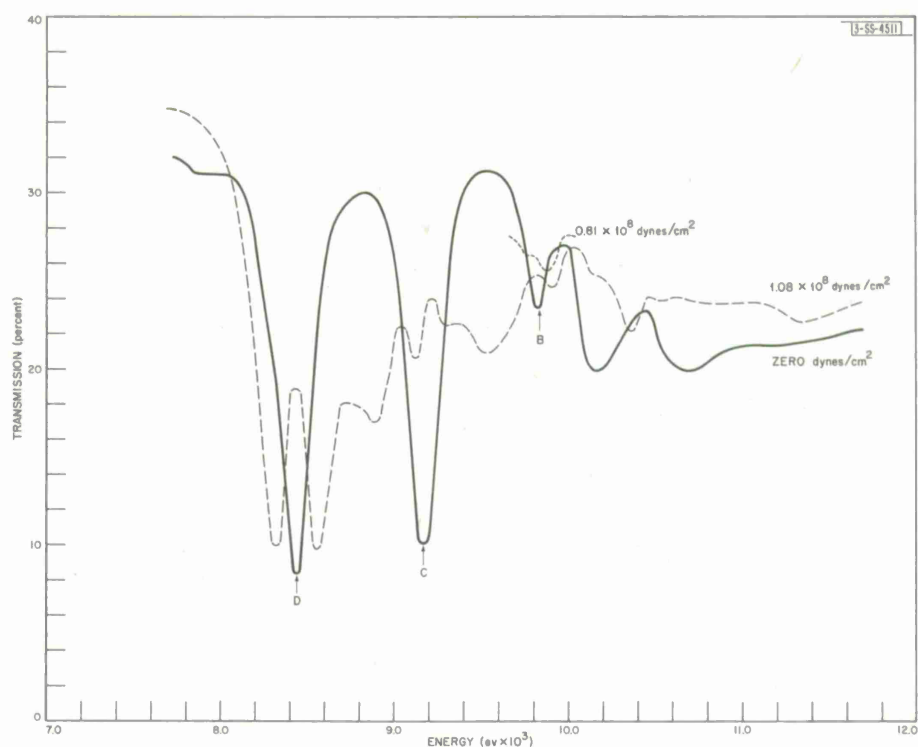


Fig. IV-11. Effect of uniaxial strain on excitation spectra of group III impurity (gallium) in germanium at $T \approx 8^\circ\text{K}$. The strain is parallel to a (100) face.

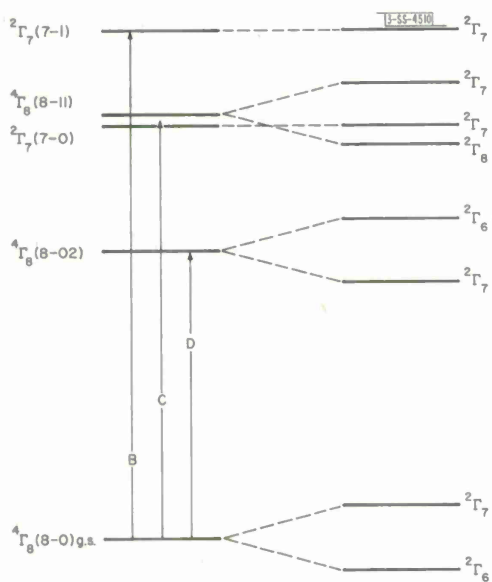


Fig. IV-12. Energy states for group III impurity in germanium.

lasers which give higher resolution are in progress; these experiments may resolve the apparent discrepancy with the spin resonance experiment.

Mildred S. Dresselhaus
J.G. Mavroides

8. Excitation Spectra of Group III Impurities in Germanium Under Uniaxial Stress

A study of the behavior of the excitation spectra of group III impurities in germanium under uniaxial stress was carried out to determine the deformation potential parameters for the valence band of germanium and also to obtain further information about these impurity states.

Figure IV-11 shows a typical spectra for a group III impurity in germanium; here the transmission vs wavelength is displayed for zero stress and also for uniaxial stress parallel to the (100) direction. The experimental lines are identified by the letters indicated in the theoretical diagram of Mendelson and James¹⁷ given in Fig. IV-12.

The experimental lines have been identified by using estimates of the polarized line intensities obtained from the wave functions of Schechter¹⁸ and Mendelson and James.¹⁷ From this identification, the acceptor state splittings of the ground state and three excited states for the gallium and indium impurities in germanium under (100) and (111) strains have been determined.

TABLE IV-1 DEFORMATION POTENTIAL PARAMETERS FOR THE VALENCE BAND OF GERMANIUM			
	Impurity		Average
	Gallium	Indium	
D_u (ev)	1.3	1.4	1.35
$D_{u'}$ (ev)	1.7	2.0	1.85

The experimental B-line corresponds to the transition from the ground state to the excited state Γ_7 which does not split under either (100) or (111) strain. The splitting of the B-line thus gives the splitting of the ground state. By using the results of Bir, Butikov and Pikus¹⁹ for the ratio between the acceptor ground state splitting and the splitting of the valence band edge in germanium, deformation potential parameters²⁰ have been determined and are given in Table IV-1.

D.H. Dickey
J.O. Dimmock

B. SOLID STATE MAGNETOPLASMAS

1. Magnetoplasma Cyclotron Resonance in p-Type PbSe

Measurements are being made of the microwave surface impedance of p-type PbSe as a function of magnetic field. In the experiment the sample is made part of the end wall of a TE_{113} cylindrical cavity resonant at 70 kMcps, with the static magnetic field applied in the plane of the

Section IV

sample. Such a geometry is particularly fruitful for investigating this material when a high concentration of holes ($\sim 1 \times 10^{18}/\text{cm}^3$) exists even at liquid helium temperature, so that the free carrier plasma frequency greatly exceeds the radiation frequency. As a result, large longitudinal depolarizing fields exist which shift the natural frequencies of the plasma away from the cyclotron frequencies of the individual carriers, producing onsets of absorption at hybrid frequencies which involve the masses of all the carriers. These hybrid resonances are followed by sudden decreases in absorption – the so-called dielectric anomalies.

Structure has been observed in the surface absorption vs magnetic field curve in the region below 3000 gauss. This may be partly due to the above-mentioned effects and partly to subharmonic resonances of the Azbel-Kaner type. Tentative identification of the main absorption peak when the field is along the [100] direction with the dielectric anomaly gives a value for the transverse effective mass of $m_t = 0.048 \pm 0.005 m$, which may be compared to the value obtained previously* from measurements on this same sample of the temperature dependence of the amplitude of Shubnikov-de Haas oscillations, $m_t = 0.050 \pm 0.006 m$.

A rectangular cavity is being constructed in order to provide more positive control of the relative orientation of the RF electric field in the cavity and the static magnetic field, so that the behavior of the ordinary and extraordinary modes of propagation in the crystal may be investigated separately. This is essential in order to simplify the theoretical analysis and to determine the anisotropy of the effective mass ellipsoids.

Additional structure at higher magnetic fields has also been observed and is being investigated.

S. Berman
W.C. Kernan

2. Magnetoplasma Wave Propagation in PbTe

The transmission of 9-kMcps microwave signals through oriented slices of PbTe at 4.2°K in DC magnetic fields up to 10 kG is being studied.

The mode of propagation within the sample is the helicon wave which, for the present experimental arrangement, is well described by a plane wave with a complex propagation vector \vec{q} . In the long wavelength limit the dispersion relation is obtained from simultaneous solution of Maxwell's equations and an equation derived from the equation of motion of the free carriers.²² To zero order in ω/ω_c and $1/\omega_c \tau$, where ω_c is the cyclotron angular frequency and τ the particle collision time, this equation can be written as

$$\vec{E} + \frac{1}{ne} \vec{J} \times \vec{B}_0 = 0 \quad . \quad (1)$$

Here \vec{E} and \vec{J} are macroscopic field quantities, \vec{B}_0 is the applied DC magnetic field, and n is the carrier concentration. The solution is an undamped wave whose propagation constant depends only on carrier density and the angle Θ between the DC magnetic field and the propagation direction given by

$$q = \sqrt{\frac{ne\omega\mu_0}{B_0 \cos \Theta}} \quad . \quad (2)$$

* See Sec. IV-A-2 of Ref. 21.

In order to allow for the effects of finite τ and nonzero ω in the equation of motion of the particles, the zero order solution may be taken as the unperturbed solution in a perturbation calculation to first order in ω/ω_c and $1/\omega_c \tau$. The result is an imaginary component of q (damping) and a correction term to the real part of q . These terms are a function of the mass and collision time anisotropies of the particles and of the crystal orientation when the perturbation treatment is generalized to allow for a tensor mass and collision time.

Experimentally, we observe the variation of q with θ which shows a significant dependence on the anisotropies. A highly sensitive microwave receiver is used which allows measurement of both the phase and amplitude of the transmitted signals to power levels of the order of 10^{-20} watts.²³ Helicon transmission has been observed for propagation along the $\langle 100 \rangle$ direction in p-type PbTe, and preliminary data indicate that the effects of anisotropy should be measurable in both the attenuation and phase in high mobility samples.

J. Walpole
A.L. McWhorter

C. HYPERSONIC WAVES IN SOLIDS

1. Microwave Phonon Generation at 70 kMcps

Further attenuation measurements have been carried out on x-cut quartz in order to determine more accurately the temperature dependence of 70-kMcps longitudinal acoustic waves. The previously reported T^4 dependence²⁴ resulted from measurement of the relative echo height of the first four echoes in an x-cut quartz sample, whereas the most recent results are based on eight to ten echoes. The T^4 variation is confirmed with improved accuracy.

In addition, a large reduction in the decrement between echoes at a given temperature has been observed which is dependent on the position of the sample in the microwave cavity. Under the most favorable circumstances, this leads to observation of up to fifteen echoes although attenuation measurements are made only on a nearly exponential display of about ten.

J. B. Thaxter
C. D. Parker

2. Attenuation of 9-kMcps Hypersonic Waves in Semiconductors

At low temperatures the attenuation of hypersonic waves in semiconductors is primarily the result of electron-phonon scattering since the phonon-phonon scattering attenuation becomes quite small. This electronic contribution to the attenuation is being measured to determine the electron-phonon coupling parameters in GaAs and InSb. Both the deformation potentials and the piezoelectric constants can be determined from these measurements independent of the electron mean free scattering time as long as $q\ell > 1$. Here q is the wave vector of the generated hypersonic wave and ℓ is the electron mean free path. In this region the absorption is a resonant interaction corresponding to a Landau type damping of the hypersonic wave by electrons moving synchronously with it.

The experiments consist of the measurement of the magnetic field dependence of the attenuation and velocity of the hypersonic wave at a temperature of 25°K. These measurements are being made with a very sensitive microwave detection system similar to one that has been used for CW transmission experiments,²³ but adapted for pulsed operation in a reflection configuration. Unity signal-to-noise is obtained with an average input power to the receiver of about 10^{-20} watts.

Section IV

This corresponds to approximately 170-db loss in coupling to the hypersonic wave and path attenuation in the semiconductor for unity signal-to-noise in our system. A unique feature of this detection system is the capability of measuring extremely small velocity changes, of the order of 5 parts in 10^8 for samples 1 cm long.

Preliminary measurements on samples of GaAs oriented in the $\langle 111 \rangle$ and $\langle 110 \rangle$ directions and on x-cut quartz have verified the performance of the microwave detection system.

K.W. Nill
A.L. McWhorter

D. MAGNETISM

1. Long-Range Exchange Interaction from Spin Wave Resonance

In a previous report,^{*} results concerning the long-range exchange interaction from spin wave resonance experiments on a number of permalloy films were presented. The squared interaction distance ρ^2 , given by $\sum_r J_r r^4 / \sum_r J_r r^2$, where J_r is the exchange integral between spins a distance r apart, was 120 times the square of the nearest-neighbor distance. This result, obtained from the coefficient of the quartic term in the spin wave dispersion relation measured at 300°K, compared favorably with ρ^2 obtained from an earlier spin wave interaction experiment whose interpretation was valid up to 80°K. In order to ascertain that there is no radical change with temperature in the coefficient of the quartic term, it was decided to repeat the dispersion experiment at low temperatures.

Preliminary studies of the spin wave dispersion relation for permalloy have been completed on the same sample (63 percent nickel-37 percent iron) at 4.2°, 77°, and 298°K. The results indicate that the long-range interaction distance remains approximately an order of magnitude greater than the nearest-neighbor distance at each temperature and that the coefficient of the quartic term of the dispersion relation increases by roughly 20 percent from room temperature to 4.2°K.

R. Weber
P.E. Tannenwald
J.W. Burke

2. Magnetic Properties of Chromium Spinels with Nonmagnetic A-Sites

Magnetic measurements are being made of a number of spinels of the form ACr_2X_4 , where A is nonmagnetic zinc or cadmium, and X = oxygen, sulfur or selenium. Our measurements on the normal²⁵ cubic spinel $CdCr_2Se_4$ show it to be ferromagnetic with a moment of $5.8\mu_B$ at 10 koe and 4.2°K compared with a theoretical spin-only value of $6\mu_B$ for Cr^{3+} ions. The Curie temperature determination made in low field ($H = 100$ oe) indicates $T_c = 130^\circ K \pm 1^\circ$. Susceptibility measurements were carried out to 400°C, and the resultant $1/\chi_M$ vs temperature curve is shown in Fig. IV-13 along with the magnetization curve. The susceptibility curve yields a Curie constant $C = 3.66$, which is consistent with the predicted value $C = 3.75$ for spin-only Cr^{3+} ions. In this respect it differs radically from the ferromagnetic $CuCr_2X_4$ (X = S, Se, and Te) spinels which contain a mixture of Cr^{3+} and Cr^{4+} ions, which leads to metal-like electrical

^{*} See Sec. IV-A-1 of Ref. 21.

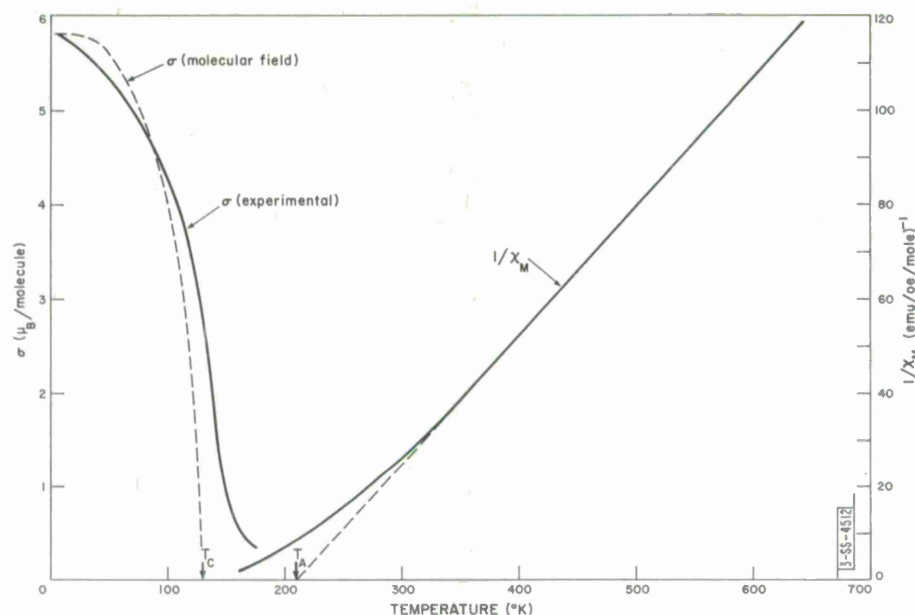


Fig. IV-13. Magnetization and susceptibility vs temperature in CdCr_2Se_4 for $H = 10$ koe.

conductivity behavior.²⁶ CdCr_2Se_4 , on the other hand, behaves like a semiconductor with a relatively high resistivity.²⁷ To our knowledge, CdCr_2Se_4 is the first example of a nonconducting ferromagnetic chalcogenide involving a 3d ion; as such, it is an interesting material for comparison with the Heisenberg model of ferromagnetism.

For a ferromagnetic normal spinel with nonmagnetic A-sites, the octahedral B-sites are all equivalent, and the molecular field acting at these sites is just

$$\vec{h}_B = \sum_i J_i \vec{S}_B = K \vec{S}_B \quad (3)$$

where i corresponds to the i^{th} nearest neighbor, and J_i corresponds to the product of the i^{th} nearest-neighbor exchange interaction and the corresponding number of neighbors. Thus, for a ferromagnetic material, molecular field theory predicts a magnetization curve of the form $M = M_0 B_J(KM/kT)$ independent of the nature of the interactions, where $B_J(z)$ is the Brillouin function. The normalized magnetization curve predicted by the Brillouin function for $J = 3/2$ (the value for spin-only Cr^{3+}) is also shown in Fig. IV-13 and is seen to disagree markedly with the experimental results.

The ratio of T_C/T_A to be expected for this structure was obtained from a high-temperature expansion of the susceptibility of the form

$$\chi = \frac{C}{T} \left\{ 1 + \sum_n a_n \left(\frac{J_1}{kT} \right)^n \right\} \quad (4)$$

which was carried out to fourth order assuming nearest-neighbor interactions only. The predicted value of $T_C/T_A \lim_{n \rightarrow \infty} = a_n/a_{n-1}$. Our results for a_n/a_{n-1} are 1.0, 0.80, 0.695, and 0.647 for

Section IV

$n = 1$ through 4, respectively, and appear to be converging to a number near the experimental value $T_A/T_C = 0.619$.

The behavior of CdCr_2Se_4 is in marked contrast with that obtained by Lotgering in ZnCr_2Se_4 (Ref. 26) and ZnCr_2S_4 (Ref. 28). The high temperature inverse susceptibility curves in these two materials have a positive T_A , indicating ferromagnetic coupling, but at about room temperature the curves depart from linearity and they both become antiferromagnetic at low temperature. Lotgering explained these results on the basis of a ferromagnetic nearest-neighbor interaction and an antiferromagnetic next-nearest-neighbor interaction. In view of our results, it seemed worthwhile investigating the possibility that the behavior of the susceptibility of ZnCr_2Se_4 and ZnCr_2S_4 was a size effect involving only near-neighbor interactions. It is known that the $\text{Cr}^{3+} - \text{Cr}^{3+}$ interaction is strongly ferromagnetic in MnCr_2S_4 (Ref. 29), whereas it is strongly antiferromagnetic in spinels with smaller unit cells such as ZnCr_2O_4 (Ref. 30) and CoCr_2O_4 (Ref. 31). This is due to the fact that the nearest-neighbor interaction is a combination of an antiferromagnetic direct interaction,³² which is strongly sensitive to cell dimensions, and a ferromagnetic superexchange interaction, which is less sensitive to cell size. The unit cell dimensions of ZnCr_2Se_4 and ZnCr_2S_4 were therefore measured at room temperature and at 84°K, and the results are shown in Table IV-2.

TABLE IV-2		
Sample	Cell Length (a_0) (Å)	
	T = 300°K	T = 84°K
ZnCr_2Se_4	10.497 ± 0.002	10.485 ± 0.002
ZnCr_2S_4	9.986 ± 0.002	9.965 ± 0.002

As can be seen in Table IV-2, the change in cell dimension with temperature is extremely small and cannot play a decisive role. Hence it must be concluded that Lotgering's explanation in terms of next-nearest neighbors is qualitatively correct. We have therefore begun to investigate the effect of zinc and cadmium on next-nearest-neighbor interactions.

Since Anderson³³ has shown that nearest-neighbor interactions alone cannot lead to long-range antiferromagnetic order in a cubic spinel with nonmagnetic A-sites, the Néel temperature T_N serves as a measure of the next-nearest-neighbor interaction in these materials. The T_N for the zinc-containing spinels ZnCr_2O_4 , ZnCr_2S_4 , and ZnCr_2Se_4 are 16° (Ref. 34), 18°, and 20°K, respectively. The value for ZnCr_2Se_4 is in accord with that obtained by Lotgering,²⁶ but our curve of χ_M vs T taken at 10 koe, as given in Fig. IV-14, suggests the possibility that this paramagnetic-antiferromagnetic transition is accompanied by a first-order phase change.

Preliminary measurements show that CdCr_2O_4 becomes antiferromagnetic at $T_N = 9^\circ\text{K}$. This is significantly lower than the value obtained in any of the zinc-containing spinels and

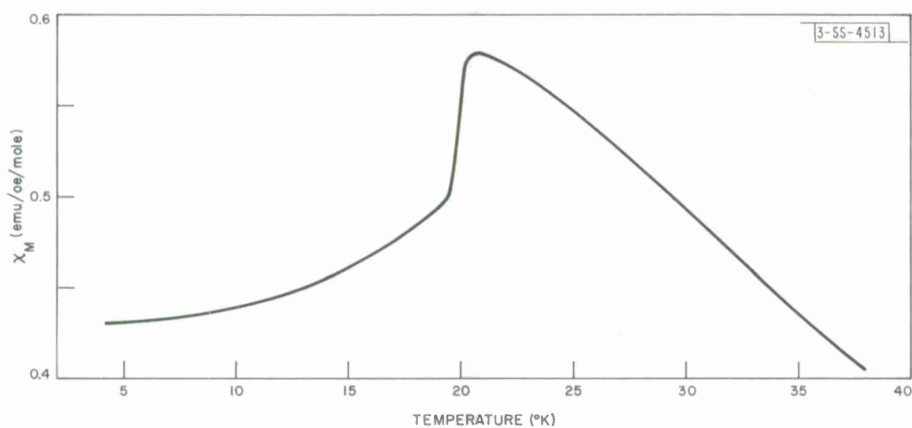


Fig. IV-14. Variation of magnetic susceptibility with temperature of ZnCr_2Se_4 in vicinity of paramagnetic-ferromagnetic transition for $H = 10$ koe.

suggests that the A-site cation may play a direct role in the next-nearest-neighbor superexchange interaction.

N. Menyuk R.J. Arnott
K. Dwight A. Wold*

E. BAND STRUCTURE OF MERCURY CHALCOGENIDES

1. Thermoelectric Power vs Pressure for HgSe , HgTe , and $\text{HgSe}_x\text{Te}_{1-x}$ Alloys

The thermoelectric power α of extrinsic n-type HgSe , HgTe , and $\text{HgSe}_x\text{Te}_{1-x}$ alloys has been measured[†] as a function of hydrostatic pressure. The purpose of these measurements is to determine the ordering of the energies of the Γ_8 and Γ_6 states and thus to classify the band structures as " α -Sn-like" or "InSb-like." As will be explained in a more detailed presentation, the application of hydrostatic pressure is expected to cause an increase in $|\alpha|$ for $E(\Gamma_6) > E(\Gamma_8)$ (InSb-like) and a decrease in $|\alpha|$ for $E(\Gamma_6) < E(\Gamma_8)$ (α -Sn-like).

This type of measurement has been used recently to supply additional evidence that HgTe has the α -Sn ordering of states at $k = 0$ (Ref. 35). Our measurements agree with that work and show a 1-percent decrease in $|\alpha|$ per 1000 bars, measured to 7000 bars, for a sample with 1×10^{18} electrons/cc at room temperature. Our measurements on HgSe of the same concentration show a 1-percent increase in $|\alpha|$ per 1000 bars, measured to 6000 bars. $\text{HgSe}_{0.50}\text{Te}_{0.50}$ with 1.6×10^{18} electrons/cc shows a decrease in $|\alpha|$ by 1 percent per 1000 bars, measured to 8000 bars. $\text{HgSe}_{0.75}\text{Te}_{0.25}$ with 7×10^{17} electrons/cc shows no change in α to 6000 bars.

These measurements then suggest that $E(\Gamma_6) < E(\Gamma_8)$ for HgTe , but $E(\Gamma_6) > E(\Gamma_8)$ for HgSe and $E(\Gamma_6) \approx E(\Gamma_8)$ for $\text{HgSe}_{0.75}\text{Te}_{0.25}$; or HgTe has the α -Sn ordering of states at $k = 0$, and HgSe has the InSb ordering and the crossover in behavior occurs at 75 percent HgSe , 25 percent HgTe . With this conclusion the problem remains of how HgSe has a zero or slightly negative thermal energy gap³⁶ yet systematically fits in with the other zinc blende and diamond semiconductors. Work directed toward this problem is continuing.

S. H. Groves

* Brown University.

† The measurements reported here were begun during postdoctoral work under Professor W. Paul of Harvard University, who generously provided the facilities for continuation of this work at Harvard after the author joined the staff of Lincoln Laboratory.

F. THEORY

1. Cyclotron Resonance of Piezoelectric Polarons

The following is an abstract from a paper which has been submitted to The Physical Review.

"The magnetic field dependence of the energy and linewidth of the transition from the $n = 1$ to $n = 0$ Landau level of a piezoelectric polaron has been calculated numerically for polarons at zero temperature. A weak isotropic piezoelectric coupling between the electron and the acoustic phonon modes is assumed and is treated as a perturbation on free electron magnetic eigenstates. It is found that the shift in the cyclotron resonance frequency due to piezoelectric electron-phonon interaction begins to differ drastically from that expected from the polaron effective mass theory when $\hbar\omega_c/mc^2 > 1$, where $\hbar\omega_c$ is the separation in energy of the unperturbed magnetic levels, m is the band mass of the electron, and c is the velocity of sound in the crystal.

"The semiclassical theory of Mahon and Hopfield is reviewed and shown not to be suitable for interpreting recently reported cyclotron resonance experiments in CdS, where the Landau level spacings were substantially greater than the mean thermal energy per electron.

"Difficulties encountered in extending the present perturbation calculation to finite temperature are pointed out.

"Finally, the weak coupling energy shift of the $n = 1$ to $n = 0$ transition for optical polarons (electrons coupled to longitudinal optical phonons) is evaluated as a function of magnetic field and compared to previous results derived for weak fields. It is suggested that the markedly non-linear magnetic field dependence of the energy shift found might offer an attractive experimental way of observing optical polaron effects on the electron self-energy."

D.M. Larsen

2. Optical Properties of Rare-Earth Metals

The electronic band structure of the rare-earth metals gadolinium, thulium, and lanthanum has been determined by means of nonrelativistic augmented plane wave (APW) calculations.³⁷ The bands near the Fermi energy are of mixed s-d character, are relatively flat, and yield a high density of states. The calculation also gives a very narrow 4f band which in gadolinium metal has a width of about 0.05 eV and lies about 11 eV below the bottom of the 5d-6s bands. (This separation, however, was found to depend strongly on the potential used and is consequently not very reliable.) The very narrow width of the 4f band indicates that the 4f electrons are highly localized as expected.

From the calculated electronic energy bands, predictions can be made concerning the expected optical properties of the rare-earth metals. Anomalies in the optical absorption and reflectivity are expected at frequencies for which the energy bands yield a high joint density of states. Also, the high density of states at the Fermi energy and the position of the 4f levels should be observable in photoemission experiments. Spicer³⁸ has recently measured the photoemission from gadolinium and has found a high density of states at the Fermi energy and a bandwidth in good agreement with our theoretical predictions. He has also observed emission from the 4f levels at about 5.8 eV below the Fermi energy. Corresponding to this, an anomaly is expected in the ultraviolet at about 6.6 eV due to transitions between the 4f levels and the conduction bands above the Fermi energy.

The infrared reflectivity of a thin film of antiferromagnetic holmium has been measured by Schüler.³⁹ This shows a temperature dependent anomaly at about 0.35 ev which has been interpreted in terms of interband transitions across the energy gaps created by the antiferromagnetic superlattice. Cooper and Redington⁴⁰ have observed the infrared absorption spectra of a thin film of dysprosium both with and without an external magnetic field. They observed an anomaly at 0.44 ev quite similar to that seen by Schüler in holmium. The spectra observed from antiferromagnetic and ferromagnetic dysprosium were identical.

The frequency of the anomaly is strongly temperature dependent both in dysprosium and holmium indicating⁴¹ that it is of magnetic origin, probably because of the exchange splitting of the s-d conduction bands. This splitting is given by

$$\Delta E = 2jS \quad (5)$$

where j is the effective exchange energy and S is the spin of the rare-earth ion.

TABLE IV-3		
	S	ΔE (ev)
Gadolinium	7/2	0.61
Terbium	3	0.52
Dysprosium	5/2	0.44
Holmium	2	0.35
Erbium	3/2	0.26
Thulium	1	0.17

An estimate of ΔE can be obtained for gadolinium from the observed saturation magnetization⁴² of $7.55 \mu_B$ /atom and our calculated density of states at the Fermi surface, assuming a conduction band g -factor of two, if the additional $0.55 \mu_B$ /atom is ascribed to an exchange polarization of the conduction electrons. Values of ΔE and S are tabulated for the heavy rare-earth metals in Table IV-3 from our calculated value of ΔE for gadolinium and assuming j is the same for all metals in the series. The agreement with the measured values of 0.44 ev for dysprosium and 0.35 ev for holmium is quite encouraging.

J.O. Dimmock
A.J. Freeman*
R.E. Watson†

3. Electronic Band Structure, Fermi Surface, and Magnetic Properties of Palladium Metal

The electronic energy bands of palladium metal have been determined by using the non-relativistic APW method. The energy bands obtained are qualitatively similar to those calculated

* National Magnet Laboratory, M.I.T.

† Bell Telephone Laboratories, Murray Hill, New Jersey.

Section IV

for copper,⁴³ silver,⁴⁴ and nickel.⁴⁵ The Fermi surface, which consists of two hole surfaces and a compensating electron surface, agrees very well with the de Haas-van Alphen data of Vuillemin and Priestley.⁴⁶ The electron surface is centered at Γ and contains approximately 0.39 electrons per palladium atom. One hole surface consists of a small pocket of about 1.6×10^{-3} holes per palladium atom centered at X. The other hole surface is open along the [100] direction and is in good qualitative agreement with the galvanomagnetic measurements of Alekseevskii, Karstens and Mozhaev.⁴⁷ The Fermi energy was found to lie slightly above a maximum in the calculated electronic density of states $N(E)$ as expected from studies of dilute alloys with iron and cobalt.⁴⁸ By using the computed $N(E_F)$, an electronic contribution to the specific heat is obtained which is only about half the observed value,⁴⁹ indicating the importance of the electron-phonon enhancement,⁵⁰ as is typical for d-band metals. The computed paramagnetic susceptibility $\chi(T)$ is much smaller than the experimental value,⁵¹ emphasizing the importance of exchange in markedly enhancing $\chi(T)$ (Ref. 52), particularly at low temperatures.

J.O. Dimmock
A.J. Freeman*
A.M. Furdyna*

4. On the Symmetry of Hartree-Fock Ground States

In recent years there has been considerable interest in the nature of the symmetry properties of the Hartree-Fock ground state wave functions (single Slater determinants) of quantum mechanical systems.⁵³⁻⁵⁵ It is well known that exact energy eigenstates transform irreducibly ("irreducibly" always refers here to the symmetry group of the Hamiltonian of the system). No analogous theory has been developed for the transformation properties of solutions of the Hartree-Fock equations. In fact, counterexamples have been found which show that there are systems which have Hartree-Fock ground states that do not transform irreducibly. The H_2 molecule at sufficient internuclear distance provided the first counterexample.⁵⁶ This was for a system with nondegenerate exact ground state (closed shell system). A number of counterexamples have also been found recently for systems with degenerate exact ground states (open shell systems). Hartree-Fock solutions which do not transform irreducibly nevertheless may well give a better description of some physical quantities than Hartree-Fock solutions which are restricted to transform irreducibly. The Hartree-Fock description of exchange polarization in relation to hyperfine interactions provides an example of this.⁵⁵

More recently there has been speculation^{53,54} that there might be closed shell atoms or atomic ions for which the Hartree-Fock ground state does not transform irreducibly. We have proved that these speculations are correct: we have found that the Hartree-Fock ground state of the closed shell ion H^- does not have 1S symmetry, the symmetry of the exact ground state. The same is true of Li^- and O^{--} . The proof involves the assumption that the energy values in the literature^{57,58} accurately represent the exact 1S Hartree-Fock values, although this is not a critical assumption since relaxation of the symmetry restriction leads to an appreciable lowering of the energy.

T.A. Kaplan
W.H. Kleiner

* National Magnet Laboratory, M.I.T.

REFERENCES

1. Solid State Research Report, Lincoln Laboratory, M.I.T. (1964:4), DDC 613961, H-639.
2. J. Halpern and B. Lax, J. Phys. Chem. Solids 26, 911 (1965).
3. J. Halpern and B. Lax, J. Phys. Chem. Solids (to be published).
4. J. Halpern, B. Lax and Y. Nishina, Phys. Rev. 134, A140 (1964).
5. R.J. Elliott and R. Loudon, J. Phys. Chem. Solids 15, 196 (1960).
6. S. Zwerdling, B. Lax, K.J. Button and L.M. Roth, J. Phys. Chem. Solids 9, 320 (1959).
7. E.O. Kane, J. Phys. Chem. Solids 1, 249 (1957).
8. E.J. Johnson, I. Filinski and H. Y. Fan, Proceedings of the International Conference on the Physics of Semiconductors, Exeter, 1962, p. 375.
9. J. L. Brebner and G. Fischer, Proceedings of the International Conference on the Physics of Semiconductors, Exeter, 1962, p. 760.
10. F. Bassani, D. L. Greenaway and G. Fischer, Proceedings of the Seventh International Conference on the Physics of Semiconductors, Paris, 1964, p. 51.
11. Solid State Research Report, Lincoln Laboratory, M.I.T. (1964:4), p. 44, DDC 613961, H-639.
12. W. E. Krag, W. H. Kleiner, S. Fischler and H. J. Zeiger, Bull. Am. Phys. Soc. 9, 705 (1964).
13. J. W. McClure and Y. Yafet, Proceedings of the Fifth Conference on Carbon (Pergamon Press, Oxford and New York, 1960), p. 22.
14. G. Wagoner, Phys. Rev. 118, 647 (1960).
15. C. E. Moore, Atomic Energy Levels, Circular 467 (National Bureau of Standards, Washington, D.C.), Vol. I, pp. 24, 147 (1949); Vol. II, p. 138 (1952).
16. C. J. Rauch, Proceedings of the International Conference on the Physics of Semiconductors, Exeter, 1962, p. 276.
17. K. S. Mendelson and H. M. James, J. Phys. Chem. Solids 25, 729 (1964).
18. D. Schechter, J. Phys. Chem. Solids 23, 237 (1962).
19. G. L. Bir, E. I. Butikov and G. E. Pikus, J. Phys. Chem. Solids 24, 1467 (1963).
20. W. H. Kleiner and L. M. Roth, Phys. Rev. Letters 2, 334 (1959).
21. Solid State Research Report, Lincoln Laboratory, M.I.T. (1965:1).
22. C. R. Legendy, Phys. Rev. 125, A1714 (1964).
23. A. L. McWhorter and W. G. May, IBM J. Research Develop. 8, 285 (1964).
24. J. B. Thaxter and P. E. Tannenwald, Appl. Phys. Letters 5, 67 (1964).
25. P. Raccah (private communication).
26. F. K. Lotgering, Proceedings of the International Conference on Magnetism, Nottingham, England, 1964, to be published.
27. A. Wold and R. Bouchard (private communication).
28. F. K. Lotgering, Philips Res. Report 11, 190 (1956).
29. N. Menyuk, K. Dwight and A. Wold, J. Appl. Phys. 36, 1088 (1965).
30. T. R. McGuire, L. N. Howard and J. S. Smart, Ceramic Age 60, 22 (1952).
31. N. Menyuk, K. Dwight and A. Wold, J. de Physique 25, 528 (1964).
32. D. G. Wickham and J. B. Goodenough, Phys. Rev. 115, 1156 (1959); J. B. Goodenough, Phys. Rev. 117, 1442 (1960).
33. P. W. Anderson, Phys. Rev. 102, 1008 (1956).
34. J. M. Hastings and L. M. Corliss (private communication).

Section IV

35. R. Piotrkowski, S. Porowski, Z. Dziuba, J. Ginter, W. Girat and L. Sosnowski, *Phys. Stat. Sol.* 8, K135 (1965).
36. T.C. Harman and A.J. Strauss, *J. Appl. Phys. Suppl.* 32, 2265 (1961).
37. J.O. Dimmock and A.J. Freeman, *Phys. Rev. Letters* 13, 750 (1964), DDC 613895.
38. A.J. Blodgett, W.E. Spicer and A. Yu (to be published).
39. C. Chr. Schüller, *Phys. Letters* 12, 84 (1964).
40. B.R. Cooper and R.W. Redington, *Phys. Rev. Letters* 14, 1066 (1965).
41. H. Miwa, *Progr. Theoret. Phys. (Kyoto)* 29, 477 (1963).
42. H. Nigh, S. Legvold and F.H. Spedding, *Phys. Rev.* 132, 1092 (1963).
43. B. Segall, *Phys. Rev.* 125, 109 (1962); G.A. Burdick, *Phys. Rev.* 129, 138 (1963).
44. B. Segall, "Theoretical Energy Band Structures for the Noble Metals," Report No. 61-RL-(2785G), General Electric Research Laboratory, Schenectady, New York, July 1961.
45. J.G. Hanus, Quarterly Progress Report No. 44, Solid State and Molecular Theory Group, M.I.T. (15 April 1962), p. 29; J. Yamashita, M. Fukuchi and S. Wakoh, *J. Phys. Soc. Japan* 18, 999 (1963); S. Wakoh and J. Yamashita, *J. Phys. Soc. Japan* 19, 1342 (1964).
46. J.J. Vuillemin and M.G. Priestley, *Phys. Rev. Letters* 14, 307 (1965).
47. N.E. Alekseevskii, G.E. Karstens and V.V. Mozhaev, *J. Exptl. Theoret. Phys. (U.S.S.R.)* 46, 1979 (1964) [English translation: *Soviet Phys. - JETP* 19, 1333 (1964)].
48. A.M. Clogston, *et al.*, *Phys. Rev.* 125, 541 (1962); T. Takahashi and M. Shimizu, *J. Phys. Soc. Japan* 20, 26 (1965).
49. B.W. Veal and J.A. Rayne, *Phys. Rev.* 135, A442 (1964).
50. K. Krebs, *Phys. Letters* 6, 31 (1963); R.E. Prange and L.P. Kadanoff, *Phys. Rev.* 134, A566 (1964).
51. F.E. Hoare and J.C. Matthews, *Proc. Roy. Soc. (London)* A212, 137 (1952); H. Kojima, R.S. Tebble and D.E.G. Williams, *Proc. Roy. Soc. (London)* A260, 237 (1961); M. Wucher, *Ann. Physique* 7, 317 (1952); *Compt. rend.* 242, 1143 (1956).
52. P.A. Wolff, *Phys. Rev.* 120, 814 (1960); J.A. Seitchik, A.C. Gossard and V. Jaccarino, *Phys. Rev.* 136, A1119 (1964).
53. P.O. Löwdin, *Revs. Modern Phys.* 35, 496 (1963).
54. R.K. Nesbet, *Revs. Modern Phys.* 35, 498 (1963).
55. A.J. Freeman and R.E. Watson, *Magnetism*, G.T. Rado and H. Suhl, eds. (Academic Press, New York, 1965), Vol. IIA, p. 168.
56. J.C. Slater, *Phys. Rev.* 35, 509 (1930).
57. L.C. Green, M.M. Mulder, M.N. Lewis and J.W. Woll, *Phys. Rev.* 93, 757 (1954).
58. E. Clementi and A.D. McLean, *Phys. Rev.* 133, A419 (1964).

DOCUMENT CONTROL DATA - R&D

(Security classification of title, body of abstract and indexing annotation must be entered when the overall report is classified)

1. ORIGINATING ACTIVITY (Corporate author)		2a. REPORT SECURITY CLASSIFICATION	
Lincoln Laboratory, M.I.T.		Unclassified	
		2b. GROUP	
		None	
3. REPORT TITLE			
Solid State Research			
4. DESCRIPTIVE NOTES (Type of report and inclusive dates)			
Quarterly Technical Summary - 1 May 1965 through 31 July 1965			
5. AUTHOR(S) (Last name, first name, initial)			
Gatos, Harry C.			
6. REPORT DATE		7a. TOTAL NO. OF PAGES	7b. NO. OF REFS
15 August 1965		86	122
8a. CONTRACT OR GRANT NO.		9a. ORIGINATOR'S REPORT NUMBER(S)	
AF 19(628)-5167		Solid State Research (1965:2)	
b. PROJECT NO.		9b. OTHER REPORT NO(S) (Any other numbers that may be assigned this report)	
649L		ESD-TDR-65-318	
c.			
d.			
10. AVAILABILITY/LIMITATION NOTICES			
None			
11. SUPPLEMENTARY NOTES		12. SPONSORING MILITARY ACTIVITY	
None		Air Force Systems Command, USAF	
13. ABSTRACT			
<p>This report covers in detail the solid state research work at Lincoln Laboratory for the period 1 May 1965 through 31 July 1965. The topics covered are Solid State Device Research, Laser Research, Materials Research, and Physics of Solids.</p>			
14. KEY WORDS			
solid state devices	magnetoemission	photomultiplier	high pressure
solid state physics	Gunn effect	stimulated Brillouin scattering	simplex method
laser research	refractive index	crystal growth	magnetoplasmas
materials research	crystallographic parameters	phase studies	hypersonic waves
magneto-optics	ion density	band structure	magnetism
photoluminescence			

